DLR-IB-MO-HF-2024-70

Analysis of Environmental Factors and Operating Conditions on Degradation Patterns of Aircraft Systems for Hydrogen-Based Power Generation

Masterarbeit

Davide Rescigno

Deutsches Zentrum
DLR für Luft- und Raumfahrt

ALMA MATER STUDIORUM
UNIVERSITÀ DI BOLOGNA

DEPARTMENT OF INDUSTRIAL ENGINEERING

MASTER'S DEGREE COURSE IN MECHANICAL ENGINEERING

ANALYSIS OF ENVIRONMENTAL FACTORS AND OPERATING CONDITIONS ON DEGRADATION PATTERNS OF AIRCRAFT SYSTEMS FOR HYDROGEN-BASED POWER GENERATION

Master's degree thesis in SERVIZI GENERALI DI IMPIANTO

Supervisor

Chiar.mo Prof. Emilio Ferrari

Candidate

Davide Rescigno

Co-supervisors

Chiar.mo Prof. Alberto Regattieri

Robert Meissner DLR

Academic Year 2023/2024

Abstract

Currently, one of the most significant challenges in the aviation industry is transitioning towards sustainable aircraft operations. The use of liquefied hydrogen for propulsion and energy supply in aircraft is a recently discussed technology. Due to its novelty in civil aviation, a notable gap exists because the implications of liquid hydrogen storage and hydrogen-based energy supply have not been adequately addressed in assessments of maintenance needs. Theoretical models, such as those based on DIN/ISO standards, often disregard variations in operating conditions and environmental factors, leading to inaccurate estimates of maintenance requirements. This study aims to bridge these gaps by systematically evaluating the impact of various operating conditions and environmental factors on the structural integrity and performance of critical components of hydrogen-powered aircraft. By introducing metrics, parameters, and degradation indices, transfer functions have been developed to link diverse operating conditions and environmental factors with the degradation patterns of various components and to describe different system design approaches. Furthermore, there is a lack of data on how the evaporation of liquid hydrogen and the rate of pressure increase in the tank may impact the degradation of relief valves over time. Therefore, this study proposes a thermodynamic model, developed using MATLAB, to simulate the dynamics of liquid hydrogen evaporation through a computational analysis. This aims to calculate the number of opening and closing cycles of relief valves. This analysis has made it possible to assess how various design variables, types of insulation, insulation degradation, venting pressures, and tank filling levels affect the frequency of relief valve triggers, thus influencing their failure rates. This methodology has facilitated the evaluation of diverse operational scenarios, offering a comprehensive framework for application in various case studies.

Contents

List of Figures

List of Tables

Nomenclature

Symbols and Indices

λ	Failure Rate	$\left[\frac{1}{hour}\right]$
ϕ	Energy Derivative	$\left[\frac{Pa \cdot m^3}{J}\right]$
I	Degradation Index	–
S	Indicator	–
m	Metric	–
P_{vent}	Venting Pressure	$[bar]$
P_i	Operating Pressure	$[bar]$
Q	Heat Transfer	$\left[\frac{J}{s}\right]$
p	Proportionality Factor	[%]
$f(x)$	Percentage Reduction in Service Life	[%]
ε	Emissivity	–
σ	Stefan-Boltzmann Constant	$\left[\frac{W}{m^2 K^4}\right]$
T_∞	Temperature of the Surrounding	$[K]$
T_s	Temperature of the Outer Tank Wall	$[K]$
T_{LH2}	Temperature of the Liquid Hydrogen	$[K]$
h	Thermal Convection Coefficient	$\left[\frac{W}{m^2 \cdot K}\right]$
h_e	Latent Heat of Vaporization of Liquid Hydrogen	$\left[\frac{kJ}{kg}\right]$
R	Thermal Resistance	$\left[\frac{K}{W}\right]$
A	Heat Exchange Surface Area	$\left[m^2\right]$
M	Mass of Hydrogen Evaporated	$\left[\frac{kg}{s}\right]$
EV	Evaporation Rate	[%]
m_{H2}	Liquid Hydrogen Mass	$[g]$
m_{ev}	Liquid Hydrogen Mass Evaporated	$[g]$
$\frac{dP}{dt}$	Pressure Rise Rate	$[bar]$
β	Tank Fill Level	[%]
ρ	Average Tank Fluid Density	$\left[\frac{kg}{m^3}\right]$
V	Tank Volume (Liquid and Vapor)	$[m^3]$
x	Fluid Quality	–
N_{SL}	Number of Valve Design Opening Cycles per Day	$[cycles]$
N_{CD}	Number of Valve Opening Cycles per Day	$[cycles]$
N_{UD}	Nusselt Number	–
R_{AD}	Rayleigh Number	–
P_r	Prandtl Number	–

Acronyms

ACL	Anode Catalyst Layer
AGDL	Anode Gas Diffusion Layer
ATDI	Average Total Degradation Index
BPP	Bipolar Plate
CCL	Cathode Catalyst Layer
CFRP	Carbon Fiber Reinforced Polymer
CGDL	Cathode Gas Diffusion Layer
CL	Catalyst Layer
COPV	Composite Overwrapped Pressure Vessel
CTE	Coefficient of Thermal Expansion
ECSA	Electrochemical Surface Area
ENY	Expected Number of Years
FCS	Fuel Cell System
FEM	Finite Element Method
FIC	Flight Cycle
FP	Filling Pressure
GDL	Gas Diffusion Layer
GFRP	Glass Fiber Reinforced Polymer
GRMS	Gravity Root Mean Square Acceleration
ISO	International Organization for Standardization
LBB	Leak Before Break
LCFA	Low Cycle Fatigue Analysis
MEA	Membrane Electrode Assembly
MLI	Multi-Layer insulation
MNCTF	Mean Number of Cycles To Failure
MPD	Maintenance Planning Document
MTBF	Mean Time Between Failures
MTBR	Mean Time Between Removals
MTBUR	Mean Time Between Unscheduled Removals
MTTF	Mean Time To Failures
NWP	Normal Working Pressure
OHD	Operating Hours per Day
PEM	Proton Exchange Membrane
PEMFC	Polymer Electrolyte Membrane Fuel Cells
PRV	Pressure Relief Valve
PSV	Pressure Safety Valve
RH	Relative Humidity
SOC	State of Charge
SOFI	Spray-on Foam Insulation
TT	Twin Tail
TTB	Twin Tail-Boom
TVS	Thermodynamic Vent System

1 Introduction

Hydrogen-powered aircraft represent a significant step towards sustainable aviation, offering a substantial reduction in environmental impact and moving away from traditional fuel dependencies. The European Commission has underscored this transition through its Green Deal initiative, aiming for a climate-neutral air mobility system by 2050 [85]. Hydrogen stands out as an ideal energy storage medium due to its carbon-free nature and its prevalence in the universe, which makes it readily available. The interest in hydrogen surged during the last fuel crisis, and with the current rise in fuel prices combined with environmental concerns, hydrogen is being revisited as a solution for long-term energy needs. Consequently, a growing consensus holds that hydrogen is the only genuinely viable option for addressing long-term environmental and energy dependency challenges [62]. As a flexible energy carrier producible from a diverse array of primary energy sources, hydrogen has the potential to enhance the reliability of fuel supply for aviation, possibly easing geopolitical tensions linked to the localization of fossil fuel resources [129].

However, the successful integration and functioning of such aircraft necessitate an in-depth comprehension of the intricate relationships between operational parameters, environmental variables, and the degradation processes affecting key components.

Within the realm of hydrogen-powered aircraft, this study will demonstrate that the inclusion of environmental factors is crucial to determine the degradation patterns of the new key components of such systems. In addition, the operating conditions of these systems have not been thoroughly examined and addressed. Investigating these conditions and factors is vital for ensuring the safety, efficiency, and longevity of aircraft components and systems. This is especially pertinent in terms of durability, where extensive research already explores the impacts of hydrogen-powered aircraft on areas like aircraft design, airline operations, and maintenance needs [46, 85]. Typically, maintenance requirements are projected using comparative models like DIN/ISO standards, which, however, do not consider specific some operating conditions or environmental factors. A change in operating parameters or environmental factors, such as exposure to extreme temperature gradients, hydrogen environment or vibration loads, currently does not alter the estimated maintenance needs. Given the innovative nature of such concepts in civil aviation and the constrained availability of information, developing surrogate patterns is imperative for understanding the impact of various environmental factors and operating conditions on the system's degradation behavior.

1.1 Research objective

By systematically evaluating the impact of various operating and environmental conditions on critical components, this research aims to refine the understanding of maintenance requirements. This enhanced understanding will surpass theoretical models by accommodating real-world scenarios, thus providing a more accurate foundation for future evaluations of maintenance needs. Incorporating operating and environmental conditions into the assessment of maintenance requirements is anticipated to influence system design assumptions significantly.

By bridging the current gap in considering specific operating conditions and environmental factors, this study aims to provide a methodology that is directly applicable to real-world conditions. The findings of the research extend beyond theoretical frameworks and are intended for practical application in the management and implementation of hydrogen-powered aircraft.

The research objectives can be summarized as follows:

1. Investigate the impact of operating conditions and environmental factors on the structural integrity and performance of key components in hydrogen-powered aircraft, including compressed and liquid hydrogen tanks, relief valves, and fuel cells;
    1.1 Develop and define degradation indices that correlate different operating conditions and environmental factors with hydrogen-powered aircraft components;
    1.2 Relate degradation indices to component failure rates.
2. Design a thermodynamic model to conduct a computational analysis to examine the dynamics of hydrogen evaporation and assess its effect on the activation frequency of relief valves, thus influencing their failure rate.

The aim of the research is summarized in Fig. 1.1.

1.2 Research framework

The research framework depicted in Fig. 1.2 outlines the steps to be taken to achieve the research objective. Initially, a thorough literature analysis is necessary to identify the current understanding of the degradation of critical components in hydrogen-powered aircraft. Subsequently, developing a structured methodological approach is required to derive metrics, indicators, and degradation indices that characterize the various operational and environmental conditions, as well as to outline various system design approaches.

Furthermore, a thermodynamic model will be introduced to evaluate various operational strategies, choice of insulating materials, and the impact of insulation degradation on the lifespan of the relief valves. Finally, the results from both the computational analysis and

the component degradation analysis will be examined through the calculation of degradation indices, suggesting an appropriate allocation of components for different operational scenarios.

1.3 Research question

From the research objectives and research framework, research questions are formulated, which represent the basis upon which the literature review will be conducted. This study aims to answer the following questions:

1. How do operating conditions and environmental factors influence the degradation of critical components in hydrogen-powered aircraft?
2. How can the impact of operating conditions and environmental factors be quantified and measured?
3. What additional maintenance efforts are expected as a result of unavoidable system degradation? Thus, how does the failure rate changes? What is that driven by?
4. How does the dynamics of hydrogen evaporation affect the lifespan of relief valves (and consequently other components of the thermodynamic venting system)?
5. How reliable are current technologies in enabling the widespread use of hydrogen propulsion systems?

The first question, will be discussed in Chapter 2, while a methodology to address the second question will be presented in Chapter 3. Finally, the findings of this study (pertaining to the third and fourth questions) will be extensively analyzed in Chapter 4, while future efforts required and remaining challenges will be introduced in Chapter 5.

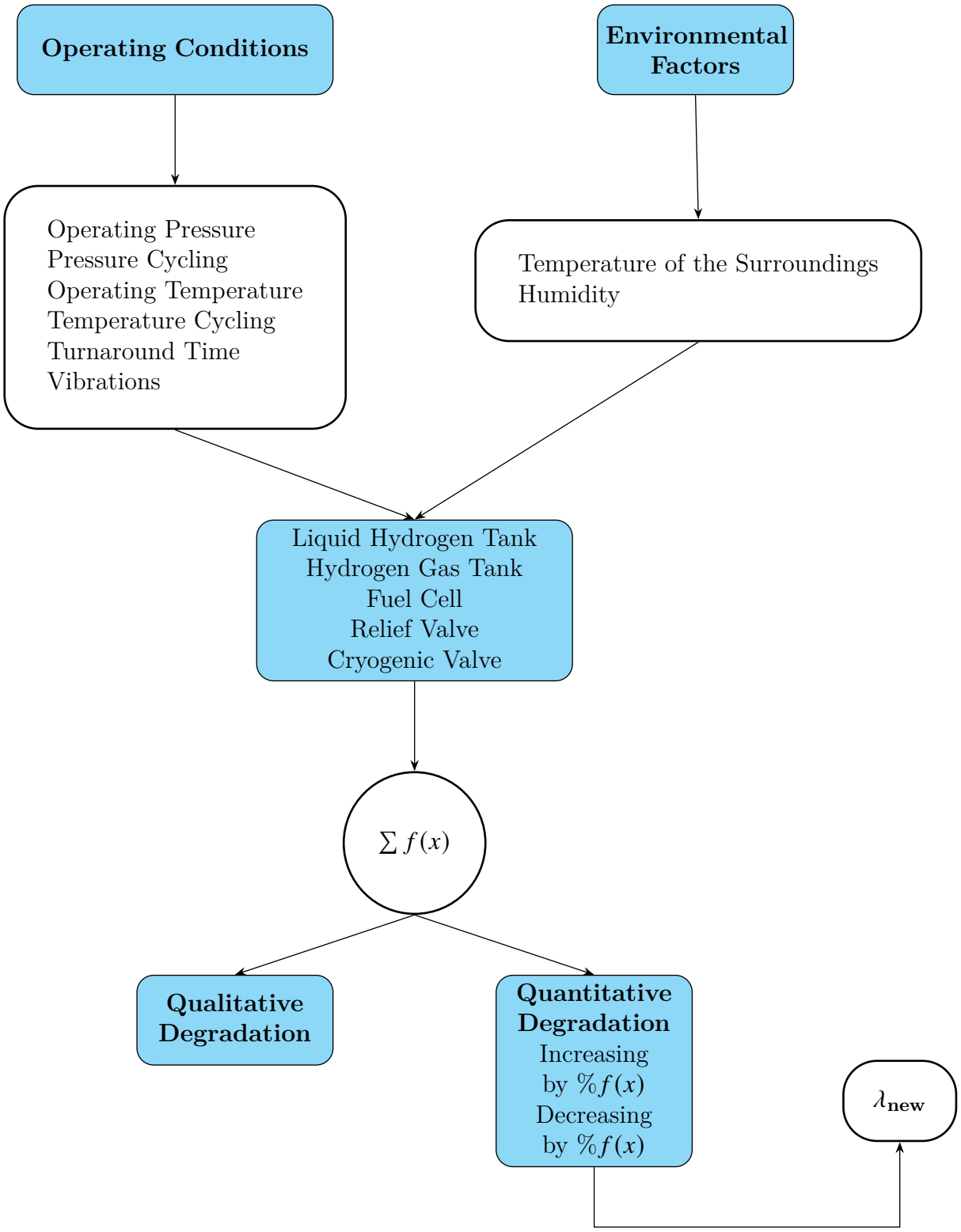

Figure 1.1 Research objective.

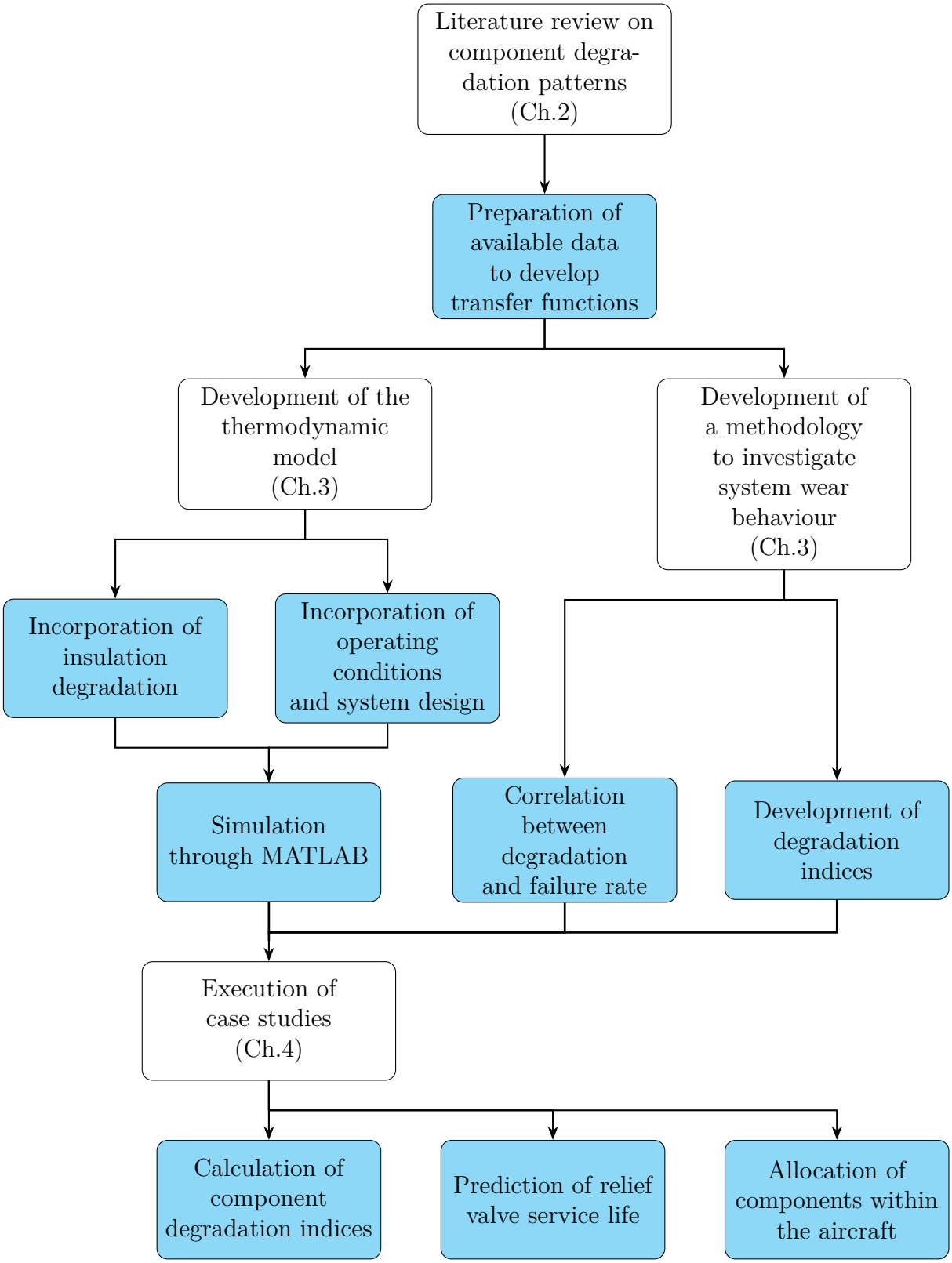

Figure 1.2 Research framework.

1.4 Definition of operating conditions and environmental factors

Within this study, the following environmental factors and operating conditions will be examined:

Environmental Factors

Environmental factors refer to the external conditions that an aircraft and its components are exposed to during flight or while on the ground (turnaround time). These include:

- **External Air Temperature**: This varies significantly with altitude and geography, directly influencing the thermal performance of the aircraft's materials and systems.
- **External Air Pressure**: The decrease in pressure with increasing altitude may have direct effects on structural resistance of the hydrogen systems.
- **Humidity**: Variations in humidity could deteriorate material properties, as will be explained in subsections 2.2.7 and 2.3.6.
- **Vibrations induced by environmental phenomena**: Turbulence or weather impacts can test the limits of the aircraft's structural integrity and affect passenger comfort.

Operating Conditions

Operating conditions, on the other hand, refer to the specific situations and parameters that aircraft components are intentionally subjected to due to their intrinsic nature and function. Examples of operational conditions include:

- **Operating Temperature**: For instance, liquid hydrogen used as fuel must be maintained at a temperature of around 20K at 1.2 bar to remain liquid [130].
- **Operating Pressure**: This pressure depends on the nature of the fuel and design requirements, and as will be illustrated in upcoming chapters, there are often increases in pressure beyond the Normal Working Pressure (NWP).
- **Vibrations induced by other aircraft components**: These differ from environmental vibrations as they are generated internally, for example, by engine operations or the aircraft's mechanical systems.
- **Turnaround Time**: This parameter does not refer to a physical condition but rather to operations related to preparing the aircraft between flights. It refers to the period needed to prepare an aircraft between arrival and subsequent departure, including activities such as deboarding passengers and baggage, cleaning, refueling, maintenance checks, boarding of passengers, baggage, and cargo, and the rest and wait time of the aircraft at the airport [109].

2 Fundamentals

As previously discussed, adopting hydrogen systems in civil aircraft will necessitate the implementation of new technologies and components. In this study, the most critical components will be examined, namely Type III and Type IV for Hydrogen Gas Tank Applications, Liquid Hydrogen Tanks, Relief Valves, and Fuel Cells. These selections stem from their pivotal roles in ensuring both the safety and operational functionality of the aircraft. Recognizing their significance in the overall system, these components stand out as key contributors to the success and reliability of hydrogen-powered aviation. This chapter aims to establish a solid foundation for the aforementioned components in order to develop reliable degradation models. To formulate such patterns, it is crucial to examine how various operating conditions and environmental factors affect each component. Operating parameters, such as turnaround time, pressure cycles, temperature cycles, fluid operating temperature and vibrations, are identified as critical in influencing the overall health of aircraft components. Concurrently, environmental factors like external air temperature, air pressure and relative humidity represent additional challenges to the durability and efficiency of these components.

Section 2.1 introduces a general discussion on the various tank configurations and fuel cell arrangements reviewed in the literature, providing an exploration of potential advantages and disadvantages. This will enable the assessment of how different design approaches—namely, the placement of components in various parts of the aircraft—can impact longevity and efficiency of the system. This evaluation will assist in identifying the most promising and degradation-resistant configurations.

Subsequently, a detailed analysis of components will be conducted from Sections 2.2 to 2.5, delving into each critical element of the hydrogen fuel system. This examination will include research on materials, insulation design and technologies, fuel cell performance and longevity, as well as the operational challenges of pumps and cryogenic valves.

Finally, Section 2.6 will introduce an overview of maintenance strategies and parameters that will be adopted in this study. Different approaches to corrective, preventive, and predictive maintenance will be discussed, highlighting how proper management and maintenance can mitigate sudden malfunctions of these hydrogen systems.

2.1 Integration of hydrogen storage systems and fuel cell technology in aircraft design

In this section, the various configurations proposed for this study will be scrutinized, with detailed analyses provided in Subsections 2.1.1 and 2.1.2. Finally, Subsection 2.1.3 will succinctly introduce the distinctions in terms of vibrational and environmental perspectives that arise from integrating the components within the fuselage as opposed to the underwing nacelle.

2.1.1 Overview of tank integration

The most frequently suggested configurations for integrating hydrogen fuel tanks involve embedding them within the fuselage of a conventional tube-and-wing aircraft design [5]. Alternatively, other designs allocate the entire cross-section of a fuselage segment to accommodate one or more tanks.

Sefain [111] introduced two distinct solutions; the first is a Twin-boom configuration, in which external slender booms function as hydrogen fuel tanks while also serving as structural components linking the wings and tail surfaces. The second proposal is a Tail-Tank configuration, wherein a tank is situated above the fuselage and physically detached from it, connected through an above-fuselage pylon and the tailplane. These configurations are collectively illustrated in Fig. 2.1: Subfig. 2.1a shows the configuration where the tank is integrated into the fuselage of a conventional tube-and-wing configuration; Subfig. 2.1b presents a configuration where the tanks are allocated in the front and rear of the aircraft; Subfig. 2.1c displays the ring tank configuration, in which the tank is arranged in a ring shape around almost the entire perimeter of the aircraft; Subfig. 2.1d illustrates the upper tank configuration, where the tanks would be placed above the passenger cabin; Subfig. 2.1e and Subfig. 2.1f show the Twin Tail-Boom (TTB) and Tail-Tank (TT) concepts, respectively.

For short-to-medium-range aircraft, it is feasible to position hydrogen tanks above the passenger cabin, whereas for long-range aircraft, hydrogen is typically stored in two large integral tanks [11].

However, as hydrogen tanks require distinct geometrical design criteria, such as a low tank surface area-to-volume ratio to minimize the boil-off rate [138], it is clear that the conventional configuration utilized for kerosene-powered aircraft is not directly transferable. Furthermore, relocating the fuel from the wings forfeits the structural load alleviation benefit, potentially resulting in an increase in the wing's structural weight [5].

(a) Tank into the fuselage of a conventional tube-and-wing configuration [5]

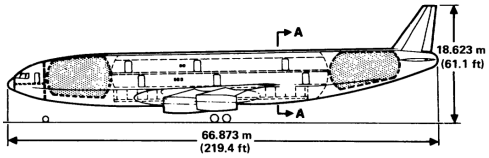

(b) Tanks in the front and rear of the aircraft [18]

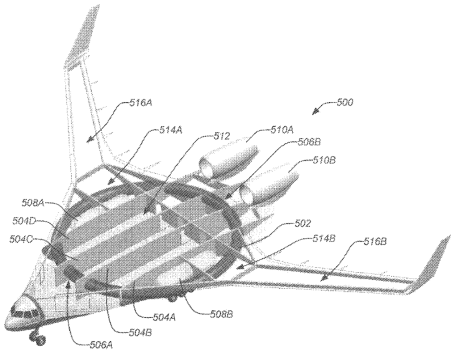

(c) Ring tank [127]

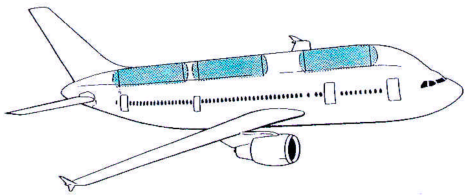

(d) Upper tank [103]

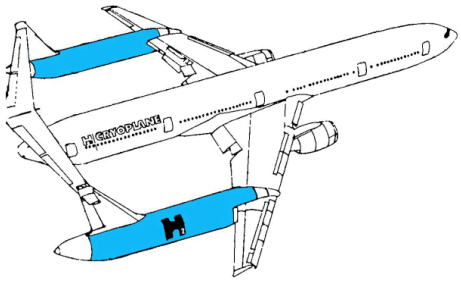

(e) Twin Tail-Boom concept [111]

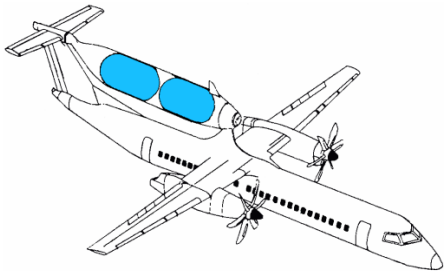

(f) Tail-Tank concept [111]

Figure 2.1 Overview of the different allocations of hydrogen tanks in hydrogen-powered aircraft.

2.1.2 Overview of fuel cell integration

In numerous aircraft designs, particularly smaller models, fuel cells are positioned within the aircraft's main body. The fuel cells are typically installed in compartments located near the aircraft's center of gravity, contributing to optimal weight distribution [139]. However, this arrangement can further limit the available space for payload and add complexity to the system, particularly in terms of cooling and the design of the electrical circuit due to the increased distances among power-train components [108]. Nonetheless, the utilization of hydrogen as a fuel source may require an increase in the wings' weight to bolster their structural integrity, countering bending and vibrations caused by aerodynamic forces. The reduced wing size and enlarged fuselage of hydrogen aircraft

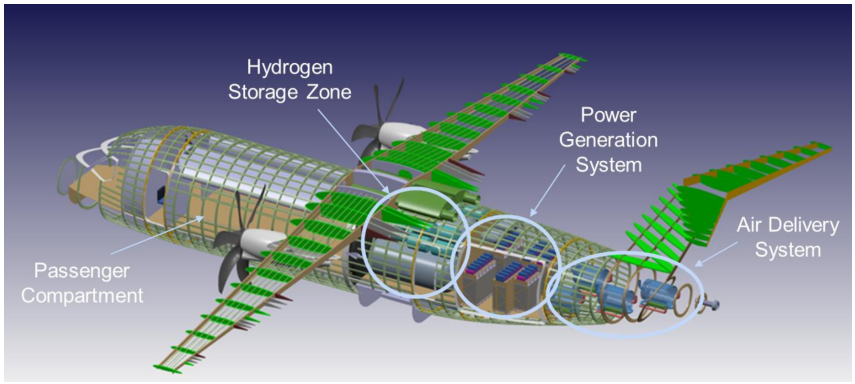

(a) Fuel Cells in the fuselage [139]

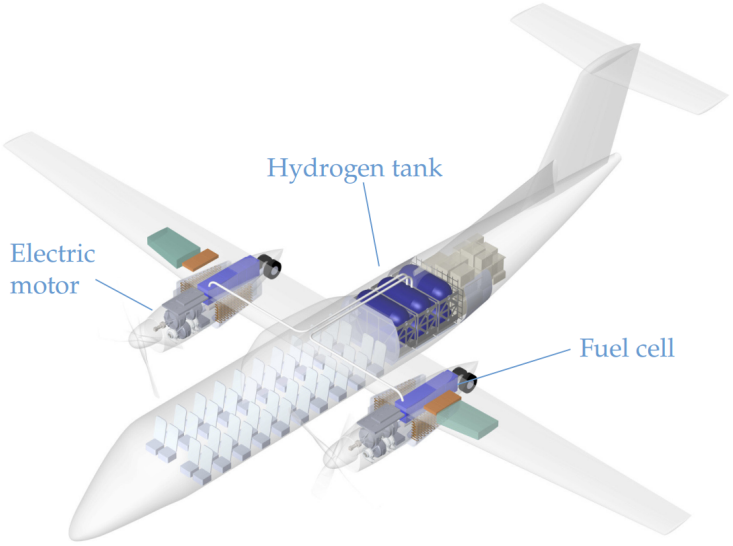

(b) Fuel Cells in underwing nacelles [5]

Figure 2.2 Overview of the different allocations of fuel cells in hydrogen-powered aircraft.

may negatively impact aerodynamic efficiency [12]. In specific scenarios, especially with larger aircraft, fuel cells might be positioned in under-wing nacelles. Locating fuel cells in under-wing pods could assist in weight distribution and maintaining the aircraft's balance [5]. These configurations are depicted in Fig. 2.2.

2.1.3 Environmental conditions and vibrational characteristics across various aircraft compartments

Since within the TTB and TT configurations, as well as Fuel Cells located in the underwing nacelle, the components are subject to extreme temperatures, higher humidity levels (in the absence of conditioning systems), and high levels of vibrations, these configurations require greater attention.

Therefore, the systems will need to withstand conditions as defined in RTCA DO-160 Section 5 [101], where testing is formulated to evaluate the performance characteristics of equipment when subjected to extreme temperature variations within its designated operational settings. This includes both internal and external aircraft equipment exposed to varying temperature-controlled and uncontrolled environments, alongside pressurized and unpressurized conditions. Additionally, it covers locations with different levels of temperature control and pressurization. This standard specifies the lower and upper temperature limits, detailing the minimum and maximum temperatures expected during flight, based on the maximum altitude or specific geographical region. Temperature ranges are defined from -55°C at 30,000 feet, -40°C at 20,000 feet, to T=70°C for high-temperature scenarios. When the aircraft is on the ground, in the absence of conditioning systems, components located in the fuselage are assumed to be subjected to a temperature $T = T_{\text{external air}} \pm 3\,^{\circ}\text{C}$. In contrast, within the nacelle beneath the wing, the temperature T is equivalent to the external air temperature.

In terms of humidity, the study hypothesizes that temperature-controlled zones maintain a humidity level of 10%, whereas areas without temperature control use the external air conditions as a reference for relative humidity, thereby being influenced by the prevailing ambient environmental factors.

To determine the typical frequency values to which components are exposed in different aircraft areas, DO 160 standards are referenced, where the relevant vibration test environments are delineated. This document provides the values of GRMS (gravity root mean square) for vibrations, representing the magnitude of vibrational acceleration.

The GRMS value indicates the effective acceleration of a vibrating system, calculated as the root mean square of the measured accelerations. This parameter is crucial in vibration analysis to quantify the intensity of vibrations experienced by a system or component. The GRMS measure signifies the amount of vibrating energy present within a structure or dynamic system [31]. Table 2.1 summarizes the reference aircraft zones and their corresponding GRMS values.

Table 2.1 GRMS values within aircraft areas.

Aircraft Zone	**GRMS (g)**
Nacelle & Pylon	8.92
Fuselage	4.12
Wing	7.94

2.2 Compressed hydrogen tanks

Composite hydrogen storage pressure vessels are typically exposed to challenging conditions, including high temperatures, cyclic pressure loads, aging, and other complex environments during charging and service. Consequently, these vessels are susceptible to fatigue damage, compromising their safety in service, as highlighted by Zhou et al. [153]. In this chapter, the effects of operating conditions and environmental factors on gaseous hydrogen tanks will be analyzed. Subsection 2.2.1 will examine the different materials used in the design of these tanks and their most common characteristics. From subsection 2.2.2 to subsection 2.2.7, instead, the various operational conditions and environmental factors to which these tanks are subjected will be analyzed.

2.2.1 Materials and failure mode

Thanks to the information obtained from Barthelemy et al. [13], Mori et al. [89], and Satyapal et al. [107], hydrogen storage can be achieved through various methods:

- In compressed form at pressures ranging from 20 MPa to 100 MPa;
- In liquefied cryogenic form at -253 °C ;
- In cryo-compressed form at intermediate low temperatures and high pressure;
- In solid form within hydrides;
- Via chemical hydrogen storage methods.

Compressed hydrogen can be stored in four types of pressure vessels as presented in Fig. 2.3. However, research is currently underway on a new category of tank, known as the V-type tank. The Type V vessel is a linerless vessel consisting solely of a composite shell. Being a linerless vessel, the Type V composite pressure vessel (CPV) is 10%–20%

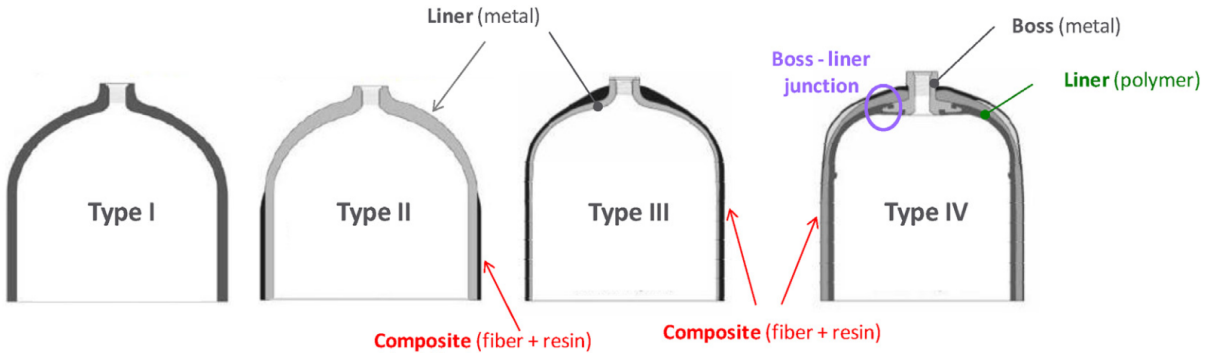

Figure 2.3 Overview of different types of hydrogen tank design [13].

lighter than the Type IV vessel, offering the lightest solution with a more efficient use of volume [74]. Metallic pressure vessels are identified as Type I, while Type II pressure vessels feature a thick metallic liner hoop-wrapped on the cylindrical part with a fiber resin composite. Considering the targeted weight efficiency for onboard storage in vehicles and airplanes, the working pressure should be to 70 MPa. This is achievable using a COPV of Type III or IV. In these vessels, the fiber-reinforced composites mainly function as protective shells to withstand internal loads such as internal pressure and temperature stratification, while the liners act as barriers between the gas and the composite, preventing leakages. Type III tanks consist of a metal liner and composite shell and offer higher strength and superior sealability. Conversely, the Type IV vessel comprises a polymer liner and composite shell, which bestows the advantages of lightweight and resistance to damage from liner collapse [74, 153].

Most common materials are:

- Metallic parts: aluminium 6061 or 7060, steel (inox or Chrome Molybdene);
- Polymer parts: polyethylene or polyamide based polymers;
- Composite: glass, aramid or carbon fibre embedded in epoxy resin Carbon fibres are preferred for 35 MPa and more applications.

Similarly, various resins can be employed, including polyester, epoxy, and phenolic, among others. Epoxy resins are preferred due to their favorable mechanical properties, stability, and compatibility with the filament winding process [13].

The primary distinction between Type III and Type IV tanks lies in their capacity to withstand various pressures and their respective weight characteristics. Type IV tanks are capable of enduring higher pressures and are inherently lighter compared to other types. On the other hand, Type III tanks offer a compromise between lightweight design and structural integrity. However, their ability to store hydrogen under a specific pressure is somewhat limited when compared to Type IV tanks. Type IV tanks are distinguished by their ability to store a greater volume of hydrogen under a given pressure, thanks to their

Table 2.2 Comparison of Type III and Type IV composite tanks.

Type	**Materials**	**Advantages**	**Disadvantages**	**Failure mode**
III	Metallic liner	High strength Reliable sealing	Perishable Heavyweight	Hydrogen embrittlement Metal liner fatigue Burst
	Composite shell			Fiber breaks Delamination Matrix cracking
IV	Polymer liner	Lightweight Structural integrity	Thermolabile	Burst Liner collapse Hydrogen leakage
	Composite shell			Fiber breaks Delamination Matrix cracking

advanced design. Therefore, Type IV tanks are often the preferred option for lightweight solutions in high-pressure hydrogen storage applications. Advantages and disadvantages of these tanks are summarized in Table 2.2. *High strength* refers to the material or structure's capability to withstand mechanical stresses without deformation or damage, crucial for the structural integrity of a tank. However, structural integrity also includes the tank's ability to retain its shape and functionality under varied operational conditions. *Thermolabile* describes sensitivity to temperature changes, leading to potential degradation when exposed to extreme temperatures. In the context of Type IV tanks, subsequent sections will reveal that the tank's materials may be temperature-sensitive, potentially leading to deterioration or diminished effectiveness at elevated temperatures. Type III tanks are considered *perishable*, indicating susceptibility to material or structural degradation over time, particularly with metal liners like aluminum, which may corrode or deteriorate due to high-pressure hydrogen exposure. This degradation, exacerbated by factors such as hydrogen embrittlement, necessitates periodic inspections and maintenance for long-term integrity.

The main failure behaviors of Type III vessels include burst and metal liner fatigue, while Type IV vessels primarily fail due to burst, liner collapse, and hydrogen leakage [74, 147]. These failure modes occur due to pressure cycles and the effects of the hydrogen environment (gas temperature and hydrogen embrittlement). Burst modes, dependent on location and consequences, are categorized into safe and unsafe modes. In safe mode, a burst occurs in the cylindrical part, whereas in unsafe mode, it occurs in the dome part.

The service life of tanks is influenced by various factors, including working conditions, structural attributes, material selection, and manufacturing processes. Working condition factors cover variables like pressure, charging and discharging processes, fire, and impact. Structural factors relate to characteristics such as length, diameter, winding angle of plies, volume fraction of fiber, and composite shell stacking sequence. Material factors pertain to the choice of composite materials, considering attributes like strength, Young's modulus, and thermal properties. Importantly, the mechanical characteristics of the composite shell are temperature-dependent, highlighting the need for temperature considerations such as charge and discharge rates and initial temperature [74].

Compressed-hydrogen tanks for vehicles are subjected to fatigue cycles during filling and consumption processes. Fast filling is crucial for the widespread adoption of hydrogen vehicles; however, it leads to an increase in the tank's interior temperature due to the Joule-Thomson effect and the heat released during gas compression. In contrast, the temperature decreases during the consumption of hydrogen gas due to pressure reduction. These significant temperature fluctuations can induce substantial thermal stress, coinciding with internal pressure changes during multiple charging and discharging cycles, ultimately leading to thermomechanical fatigue of the tank. For this reason, in the next subsection, the effects of these thermal stratifications and cycles will be examined [151].

2.2.2 Turnaround time: filling process

To ensure a refueling duration that is acceptable and comparable to that of conventional vehicles and aircraft, it is imperative to implement a rapid filling process, as highlighted in the literature [125]. However, during the compression phase of the propellant in the tank, the gas is prone to heating, which can result in a temperature increase. Should the gas experience significant temperature variations throughout the turnaround process, thermal convection might influence the tank's temperature, leading to temperature fluctuations across the tank walls due to thermal conduction.

In the context of this accelerated filling phase, an increase in the tank's pressure is directly associated with a rise in gas temperature, as depicted in Figure 2.4. This correlation underscores the critical nature of managing thermal dynamics to prevent adverse effects on the refueling process and ensure efficiency and safety.

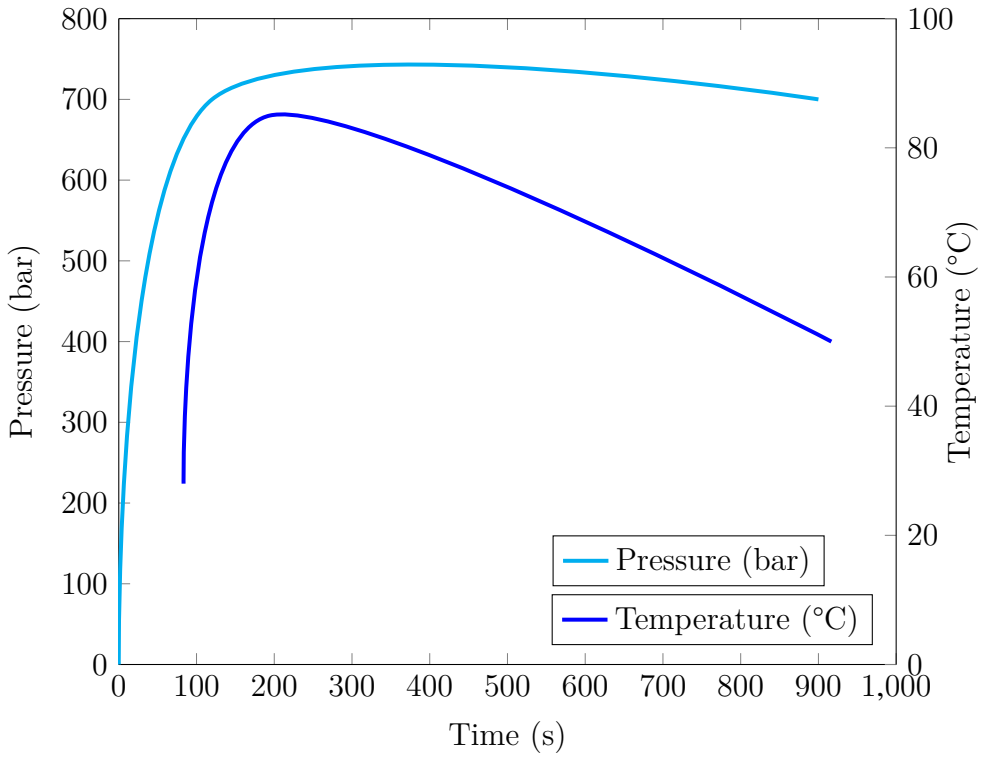

Figure 2.4 Thermo-mechanical cycle representative of a fast filling in the storage vessel [36].

Rapid filling induces thermo-mechanical stresses attributable to the increase in pressure and thermo-mechanical effects, such as the Joule-Thomson effect, the transformation of hydrogen kinetic energy into internal energy, and the compression of hydrogen at the bottom of the tank [36, 83, 145]. A critical issue throughout the entire refueling process is the rise in temperature, which is constrained by three primary factors: the safety temperature limit, the maximum filling pressure, and the tank's filling level. From a safety perspective,

due to material properties, regulations, and standards applicable to hydrogen-powered vehicles require that, under standard operating conditions, the hydrogen temperature within the tank should not exceed +85°C [87].

Empirical evidence has established that several parameters pertaining to filling conditions significantly impact the gas temperature inside the tank at the end of the filling process. Miguel et al. [87] have highlighted various methods to achieve lower maximum gas temperatures within the tank:

- When the initial pressure is higher;
- When the final pressure is lower;
- When the incoming gas temperature is lower;
- When the ambient temperature is lower;
- When the flow rate is lower.

Kim et al. [67] and Zhao et al. [150] have demonstrated that the maximum gas temperature during the fueling process decreases linearly with the increase in initial gas pressures. Specifically, Zhao et al. [150] have found that the temperature drops by 2.2 °C for every 1 MPa increase in initial pressure within the cylinder. This relationship underscores the significant impact of initial gas pressure on the thermal dynamics during the refueling process.

Melideo et al. [86] have shown that when there is a reduction in the incoming gas temperature due to pre-cooling, enhanced outcomes such as a higher average mass flow rate, an improved state of charge, and an increased total mass of gas within the tank are achieved. This finding illustrates the beneficial effects of pre-cooling on the efficiency and performance of the fueling process.

Regarding the influence of ambient temperature on the final gas temperature, there are several studies available in the literature [150, 152]. In particular, Zhao et al. [150] have obtained through their Computational Fluid Dynamics (CFD) model that an increase in ambient temperature by 1 °C is followed by an increase of 0.3 °C in the maximum temperature rise of the gas. This correlation underscores the significant impact of environmental conditions on the thermal behavior of gases during the filling process, which, in turn, will affect the thermal stresses to which the tank walls are subjected.

"Regarding the effect of the flow rate on the final gas temperature, numerous studies have highlighted that the temperature reaches a higher value with an increased mass filling rate [77, 93, 150]. These findings emphasize the direct relationship between the mass filling rate and the thermal response of the gas during the filling process, underscoring the need for careful control of flow rates to manage temperature levels effectively."

Terada et al. [121] assert that reducing the diameter of the gas jet nozzle, which supplies gas to the tank, mitigates local temperature increases within the tank, facilitating faster filling. Furthermore, according to the findings of Li et al. [72], the temperature rise within a cylinder having a larger ratio of length to diameter is higher compared to that in one with a smaller ratio. The maximum temperature is observed during the refueling process

in cylinders with a larger length-to-diameter ratio, whereas in those with a smaller ratio, it is observed at the end of the refueling process. Additionally, the temperature increase within a cylinder with a larger inlet diameter is lower than that within one with a smaller diameter.

Type III tanks have been demonstrated to yield lower gas temperatures compared to Type IV tanks. It is essential to acknowledge that due to the diverse geometry of the tanks, different fluid contact times with the tank walls, and varying temperature gradients towards the exterior, temperatures at various points within the tank will differ during refueling, leading to varying temperature gradients, commonly referred to as stratification, across the tank wall [44, 87]. To delve into this phenomenon, Miguel et al. [87] performed experiments on both Type III and Type IV tanks, wherein it was observed that the temperature increase in Type IV tanks surpassed that in Type III tanks, and this discrepancy amplified with the mass flow rate used during filling. Remarkably, in Type III tanks, filling rates could be increased by more than double those of Type IV tanks without exceeding the permissible maximum temperature limit of 85°C. Furthermore, they reported that an aluminum alloy boss proved to be more beneficial than a stainless steel counterpart due to its higher thermal diffusivity, resulting in a faster response to the inlet gas temperature compared to the latter.

To model the rapid filling process of Type IV hydrogen high-pressure storage vessels, Gentilleau et al. [36] have developed a comprehensive thermo-mechanical model. A pronounced insulating effect from the liner was observed, marked by a significant thermal gradient, which serves to mitigate the heating of the composite material. However, there is a discernible preference for heat conduction within the steel component, leading to increased temperatures in the composite, especially near the boss area. However, that the fatigue life of the head is evidently greater than that of the cylindrical part [140]

In addition, as shown by Wang et al. [135], the tensile strength and Young's modulus of the liner decrease as the temperature increases. Exposure to high temperatures will degrade the liner's performance, whereas exposure to low temperatures tends to reinforce it.

These insights lead to the conclusion that the filling process exerts a more significant impact on Type IV tanks compared to Type III tanks, as indicated in Table 2.2, where Type IV tanks are labeled as *thermolabile*. This distinction is of great significance, implying that Type IV tanks are subject to more severe temperature cycles and higher temperature gradients, particularly during rapid filling scenarios. Consequently, this results in more challenging thermo-mechanical fatigue cycles.

Regarding Type III tanks, it has been observed that dry hydrogen gas near room temperature, at pressures up to 69 MPa, does not significantly induce hydrogen embrittlement in aluminum alloys [70]. From these observations, it becomes even more evident that controlling the gas temperature by calibrating the parameters discussed in this section is crucial. This underlines the importance of temperature management within the context of maintaining the structural integrity and operational safety of hydrogen storage vessels.

2.2.3 Pressure cycling

To assess the impact of pressure cycles on these vessels, conducting hydraulic tests is deemed essential. Hydraulic tests for hydrogen storage tanks primarily focus on pressure while often neglecting temperature cycles. The fundamental aim of these tests is to evaluate the tank's ability to maintain structural integrity and containment under various pressure conditions. ISO 11119-3 [51] assert that must be able to withstand production tests of at least 12,000 pressure cycles, with one pressure cycle translating to one FlC [85].

During a hydraulic test, the vessel is filled with a fluid, usually water, and subjected to pressures that exceed those typically encountered during normal operation. The objective of this procedure is to determine whether the tank can sustain the increased pressure without undergoing deformation, developing cracks, or exhibiting leaks. The ultimate goal is to replicate extreme operating conditions to ensure the tank's durability and its adherence to established safety standards [51].

During the rapid filling process, as highlighted in the previous section, the increase in pressure leads to a rise in the temperature of the gas inside the tank. When the warm gas inside the tank cools down, exchanging heat with the colder surroundings through the tank walls, there is also a decrease in pressure. Consequently, the stabilized pressure after cooling is lower than that immediately following refueling. If the final pressure falls below the tank's NWP, the State of Charge (SOC) will be less than the desired 100%. As a result, the tank will be underfilled, compromising the system's range. To offset this effect, the target final pressure should be set above the NWP, which is why the maximum filling pressure has been established at 125% of the NWP, a value that corresponds to 87.5 MPa for a tank with a 70 MPa NWP [87].

To elucidate the impact of the maximum pressure to which pressure cycles are subjected on the lifetimes of compressed hydrogen tanks, Tomioka et al. [123] systematically varied the maximum pressure from 100% to 200% of the designed filling pressure (FP). The study involved a Type III tank (with a maximum pressure of 35 MPa). Following this, the ambient temperature pressure cycling test was also applied to a Type IV tank (with a maximum pressure of 35 MPa) for a comparative analysis with the Type III tank, where the maximum pressure applied to the Type IV tank was set at 150% of the maximum pressure. Since Type IV tanks are considered potentially superior to Type III tanks in terms of durability and strength, it has been proposed to set the pressure directly higher than NWP, without performing tests beyond 150%.

The number of cycles leading up to Leak Before Break (LBB) for Type III tanks is depicted in Table 2.3. A rise in maximum pressure is correlated with an earlier manifestation of LBB (situation in which the liner starts to leak fluid without the composite shell breaking), suggesting an accelerated fatigue effect. For Type IV tanks, when the pressure was set to 150% of the maximum design pressure, rupture occurred in the dome areas around the end boss without LBB.

Table 2.3 Lifespan of Type III and Type IV tanks subjected to pressure cycles at different filling pressures [123].

Maximum Pressure [MPa]	Type III Tank [cycles]	Type IV Tank [cycles]
35 ($FPx100\%$)	93,883	
44 ($FPx125\%$)	22,965	
53 ($FPx150\%$)	4,230	30,004
62 ($FPx175\%$)	1,739	
70 ($FPx200\%$)	871	

It must be underscored that these tests were carried out using water, not hydrogen. Therefore, factors such as the Joule-Thomson effect, hydrogen permeation, and hydrogen embrittlement were not accounted for. However, these tests can still act as a preliminary benchmark to assess the impact of hydrogen-specific properties on the fatigue behavior of tanks.

It is important to note that during hydraulic cycling, there is minimal temperature variation. In contrast, during hydrogen gas cycles, substantial temperature fluctuations occur within a single cycle, as shown in section 2.2.2. This pronounced temperature change during the hydrogen gas cycle suggests that temperature fluctuations might influence the fatigue life of the tanks. Furthermore, historical data has shown that the performance of a hydrostatic test has no correlation to the high level of safety of the pressurized cylinders and is deemed as not applicable and effective [50]. Consequently, it is crucial to evaluate the fatigue life under hydrogen gas cycling conditions and then compare these results with those obtained from hydraulic pressure-cycle tests.

2.2.4 Pressure cycles at extreme temperatures in a hydrogen environment

In hydraulic tests, vessels are subjected solely to internal pressure and not to thermal stresses, as noted by [76]. The ambient temperature pressure cycling test, as specified in the Technical standards for tanks for fuel systems of compressed-hydrogen vehicles [58] aims to evaluate the long-term fatigue life of compressed hydrogen tanks. During this test, the pressure varies between a lower limit of below 2 MPa and an upper limit exceeding 125% of the NWP, with the tank filled with a liquid. The tanks are expected to remain leak-free throughout 11,250 pressure cycles [123]. However, these tests do not consider temperature increases associated with gas or hydrogen embrittlement.

To explore the effects of the Joule-Thomson effect and hydrogen embrittlement on the durability and fatigue of composite hydrogen storage vessels, an experimental investigation was carried out under actual hydrogen conditions by Zheng et al. [151]. The study involved a Type III tank, where significant fluctuations in gas and vessel temperatures were observed with pressure changes, demonstrating thermo-mechanical cyclic loading. It is crucial to highlight that the hydrogen discharging duration in this experiment was

much shorter than typical operational conditions, potentially leading to higher temperature loads and a significant reduction in fatigue life compared to real-life applications. Therefore, the findings from this fatigue test are deemed to be relatively conservative.

In these hydrogen environment tests, failure occurred after 5,122 cycles, significantly fewer than what is typically observed in hydraulic tests, as illustrated in section 2.2.3, primarily due to significant temperature variations during hydrogen charging and discharging. Whereas hydraulic tests require vessels to withstand at least 12,000 cycles, when operating at 100% of the designed operating pressure, they can endure more than 90,000 hydraulic cycles. However, the thermal effects from hydrogen heating and the thermal stresses induced during pressure cycles significantly reduce the tank's endurance to 5,122 cycles, marking a drastic 95% decrease in fatigue life. This highlights the profound impact of thermal cycling on the integrity of composite vessels, with failures more likely under thermal cycling conditions than through mechanical fatigue alone. This type of failure is typically marked by hydrogen leakage, manifesting as soap foam on the vessel's exterior surface. The experimental results demonstrate a significant reduction in both ultimate strength and fatigue life compared to hydraulic fatigue tests [73, 151].

Regarding Type IV tanks, current literature does not address the impact of the hydrogen environment on fatigue cycles explicitly. However, polymeric materials, which are used to prevent pipeline hydrogen embrittlement as mentioned by Lei et al. [71], suggest a potential improvement in fatigue behavior. Yet, as noted in sections 2.2.2 and 2.2.3, Type IV tanks are characterized as thermolabile, with the polymeric liner susceptible to permeation. For Type IV tanks, the phenomenon of hydrogen permeation needs to be considered, which, as highlighted by Barthélémy [14] and Su et al. [117], remains a subject necessitating further investigation.

2.2.5 Impact of vibrations on the fatigue behavior of materials employed in type III and type IV tanks

The inherent vulnerability of materials used in the fabrication of Type III and Type IV tanks necessitates a comprehensive examination of their fatigue behavior under the influence of vibrations. Given the lack of existing studies or experiments specifically focusing on the exposure of Type III and Type IV tanks to vibrations, attention has been directed toward experiments conducted on the materials employed in such tanks.

The impact of vibrations on materials depends on various factors, including the specific structure of the component, the type of vibration, the duration and intensity of vibrations, and whether it is characterized as Gaussian random vibration or non-Gaussian random. Parameters such as lower frequency (Hz), upper frequency (Hz), PSD bandwidth (Hz), acceleration PSD magnitude (g^2/Hz), GRMS (g), kurtosis, etc., play pivotal roles. During cyclic vibrations, material fatigue is influenced by several factors, including the specific

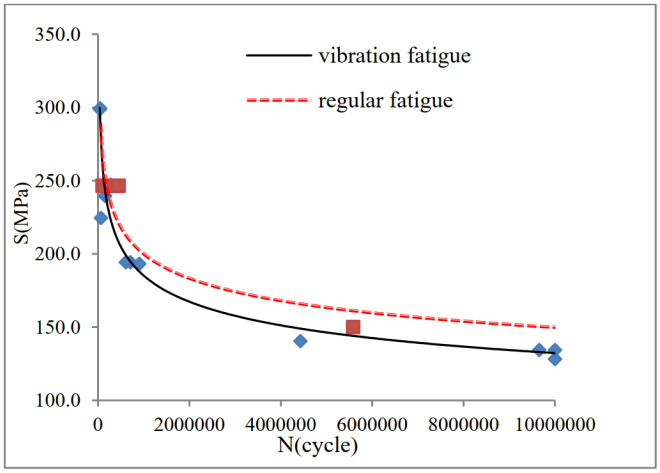

Figure 2.5 S–N curves of vibration fatigue and the regular fatigue of aluminium alloy 7050 [120].

properties of the materials used, such as their strength and ductility, the material's capacity to absorb energy, and the presence of any defects or discontinuities within the structure [31].

Regarding CFRP (Carbon Fiber Reinforced Polymer) components, they exhibit a resilient response to vibration fatigue, where the occurrence of damage is typically non-catastrophic. The failure criteria for CFRP components under vibration fatigue are not fully understood. However, the high cycle fatigue behavior of composites is often less dramatic compared to that of metal alloys, where any initiation of cracks may quickly lead to failure [26].

Voudouris et al. [131] have outlined a relationship between fatigue behavior and environmental temperature conditions through the construction of a fatigue life curve using the critical event failure criterion, considering various ambient temperatures and strain levels. The resulting S-N curve shows a significant reduction in vibration fatigue life under elevated environmental temperatures. However, it is imperative for future research to explore the fatigue behavior under sub-zero temperature conditions, which are typical conditions that aircrafts endure during operation. Currently, it may be suggested that vibrations could exhibit a more pronounced adverse effect on Type III tanks than on Type IV tanks under ambient temperatures. However, in scenarios involving elevated temperatures, the thermal susceptibility of Type IV tanks may become a significant factor.

Regarding aluminum, which is significant for the aluminum liner of Type III tanks, there is no available data where the effect of vibrations is isolated to understand its impact on the fatigue life of aluminum 6061 and 7060. However, to qualitatively understand how aluminum responds to vibrations, Yunnan Teng et al. [120] conducted vibration fatigue experiments and traditional fatigue testing on aluminum alloy 7050. The S–N curve from the vibration fatigue demonstrated trends identical to those of the traditional fatigue S–N curve. Nonetheless, they observed a significant discrepancy between the vibration fatigue and traditional fatigue curves, as depicted in Fig. 2.5. For an equal number of cycles, there was a noted reduction in alternating stress (S) by 10-20%.

2.2.6 Investigating the effects of ambient temperature on the fatigue strength of type III and type IV compressed-hydrogen tanks

Once again, the "Technical standard for containers of compressed-hydrogen vehicle fuel devices, JARI S 001" does not specify the environmental temperature to which gaseous hydrogen storage tanks are subjected. However, Tomioka et al. [124] emphasize that these tests are normally conducted at room temperature. However, it is important to note that room temperature varies by season, geographic location, and in the case of commercial aircraft, components are exposed to extreme temperatures. Tomioka et al. [124] subjected Type III and Type IV tanks to pressure-cycle tests until failure or for $45,000$ cycles under both high and low environmental temperatures. This study provides valuable

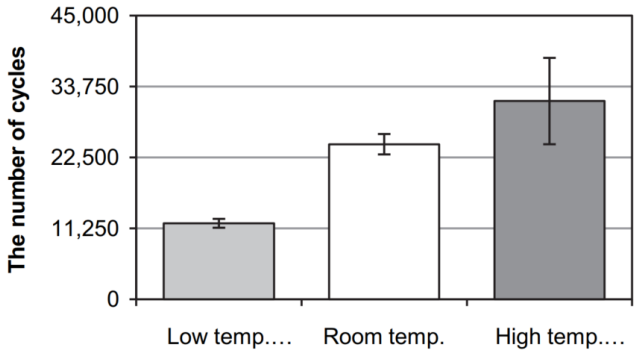

(a) Relationship between the environmental temperature and the number of cycles before leaking for the Type III test tank

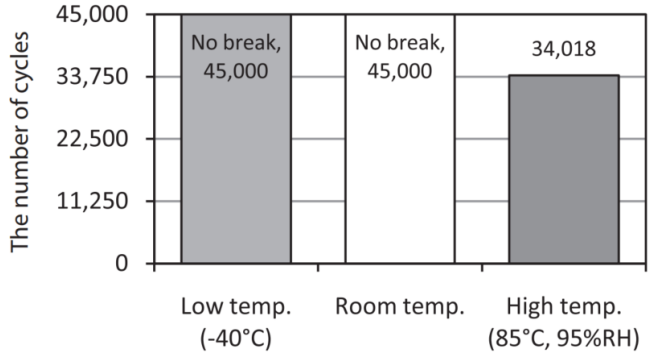

(b) Relationship between the environmental temperature and the number of cycles before breakage for the Type IV test tank

Figure 2.6 Number of filling and emptying cycles performed by Type III and Type IV tanks for different external temperatures [124].

insights into tank degradation behavior under varying environmental conditions. Three

distinct environmental scenarios were evaluated: a room-temperature condition (without temperature control), a high-temperature condition (+85 °C, 95% relative humidity), and a low-temperature condition (-40 °C). All these tests were conducted from a minimum pressure of 0 MPa to a maximum pressure of 44 MPa, corresponding to a filling pressure of 125%.

Figure 2.6a illustrates the number of cycles before leaks occur in the Type III test tank across various environmental temperatures. A comparative analysis of these results highlighted a discernible trend: the fatigue life of the Type III test tank diminishes in low-temperature environments and escalates in high-temperature environments. This indicates a direct correlation between environmental temperature and the fatigue strength of the Type III tank, emphasizing the significant impact of temperature on its performance.

The Type III tank undergoes autofrettage as part of its manufacturing process, which involves inducing plastic deformation of the liner by applying pressure exceeding the operational pressure. This technique aims to enhance fatigue strength, generating residual compressive stress in the liner and residual tensile stress in the CFRP layer when the tank is not filled. As a result, the tensile stress created in the liner during filling is counterbalanced by the residual compressive stress. This study has demonstrated that the fatigue strength of the Type III tank decreases at lower temperatures and increases at higher temperatures. The varying effects of autofrettage on lifetime changes are due to the differences in thermal expansion rates between the CFRP and the aluminum alloy, which change with environmental temperature. In high-temperature settings, the autofrettage effect is likely enhanced, leading to an improvement in fatigue strength. In contrast, the impact of autofrettage is reduced in low-temperature settings, suggesting a complex relationship between autofrettage, environmental temperature, and fatigue strength in the performance of the Type III tank. In Figure 2.6b, the graph shows the number of cycles leading to the breakage of the Type IV test tank under different environmental temperatures. Notably, no tank experienced breakage within the initial 45,000 cycles in either room-temperature or low-temperature conditions. However, in the high-temperature environment, the CFRP layer of the tank fractured after 34,018 pressure cycles, indicating that high-temperature environments significantly affect the fatigue strength of the Type IV tank. Nevertheless, it is important to note that these tests were performed with hydraulic cycles, hence these data lack the effects of gas temperature and hydrogen.

2.2.7 Influence of humidity on the fatigue behavior of materials employed in type III and type IV tanks

The effects of varying degrees of relative humidity on the fatigue life or service life of Type III and IV tanks are not documented in existing literature. However, to provide an estimate and a conceptual understanding of the probable effects that relative humidity could have on these components, this study analyzes and summarizes the effects of humidity

on the different materials used in the aforementioned tanks. On the ground, relative humidity (RH) tends to be high but decreases during takeoff, resulting in aerospace system components being subjected to humidity cycles.

Organic matrix polymers, used extensively in these tanks, are notably susceptible to water ingress. They demonstrate heightened sensitivity when exposed to both aqueous and organic fluids, leading to varying degrees of moisture permeation in humid environments, dependent on the molecular structure of the polymer. Dissolved water can act to plasticize the matrix, reducing the glass transition temperature and, by extension, the service temperature of the composite. This reduction in Tg implies a decreased resistance to elevated temperatures, significant in aerospace applications where temperature variations are common [57]. Concurrently, hydrolytic degradation, a chemical degradation process induced by water, may further reduce the thermo-mechanical properties of the composite materials, impacting the structural integrity of Type III and IV tank materials.

In the context of carbon fiber-reinforced epoxy composites, as discussed by Ray [102], moisture absorption can significantly reduce the mechanical strength of these composites, particularly at elevated temperatures. The degradation in shear strength is notably more pronounced at higher conditioning temperatures, despite similar levels of moisture absorption within carbon/epoxy laminates.

Similarly, for glass fiber-reinforced epoxy composites, moisture absorption has been shown to substantially decrease mechanical strength, particularly at higher temperatures. It thus appears that the impact of humidity is more pronounced at higher temperatures compared to standard conditions.

Furthermore, Yoshi et al. [146] highlight that high humidity (95% RH) significantly impacts the stiffness of CFRP materials, attributed to the formation of cracks and delaminations, particularly due to elevated humidity levels. Additionally, they demonstrate that the fatigue life of carbon fiber composites significantly reduces when subjected to high-humidity load cycles compared to ambient conditions.

Considering that civil aircraft are exposed to extreme cold temperatures, examining the effects of humidity at these temperatures is essential. Monitoring objects subjected to freeze-thaw cycles becomes crucial due to the effects of material aging [38]. Majewska et al. [80] showed that GFRP (Glass Fiber Reinforced Polymer) materials in a dry state exhibit negligible degradation throughout freeze-thaw cycles. However, moisture presence results in significant degradation of mechanical properties, with tensile strength and in-plane shear strength dramatically decreasing during thermal cycling. The presence of microcracks leads to increased water absorption, promoting polymer matrix plasticization or initiating delamination damage. Authors emphasize that frozen water trapped in cracks and voids can induce debonding and growth of transverse microcracks, leading to increased brittleness and degradation of composite materials.

From these studies, it is deduced that the impact of humidity on composite materials intensifies at higher temperatures compared to normal temperature conditions. The higher the relative humidity, the greater the water absorption. However, in environments with temperatures below freezing, humidity has a significantly negative impact, particularly

during freeze-thaw cycling, affecting the state of composite materials and measurement tools.

Regarding other types of aluminum such as alloys A6061, A6066, and A7075 (6000 and 7000 series), Hasunuma et al. [42] in their study mention that the fatigue lives in a *humid environment* is significantly shorter than in a *dry environment*. Therefore, generally for aluminum alloys, the fatigue life decreases considerably at extreme humidity levels compared to a dry environment.

2.3 Liquid hydrogen tank

In this section, starting from subsection 2.3.1, the generalities and materials of liquid hydrogen cryogenic tanks will be examined, followed by a detailed analysis of the insulation used in such systems in subsection 2.3.2. From section 2.3.3 to section 2.3.6, the effects of operational and environmental conditions will be explored, with a particular focus on the variables that could affect the evaporation of hydrogen from the liquid to the gaseous state.

2.3.1 Overview and materials

The reduction in mass and volume of storage tanks, as opposed to high-pressure gas storage, can be achieved through cryogenic storage of liquid hydrogen. This method leverages the properties of liquid hydrogen, which significantly increase density compared to high-pressure gas storage and allow for reduced tank mass due to the lower operating pressure. However, a notable limitation is that liquid hydrogen must be maintained at approximately -260°C, necessitating substantial insulation and meticulous design of the fuel system.

Cryogenic storage introduces several operational challenges to the fuel system [24]:

- It necessitates a hermetic insulation system to diminish liquid hydrogen boil-off and maintain cryogenic temperatures;
- Given the time-sensitive nature of liquid hydrogen storage due to boil-off, fuel typically requires production on-site or in close proximity;
- To minimize boil-off, fuel tanks must maintain a consistent pressure, which requires implementing a venting system;
- Exposure to the atmosphere must be avoided in liquid hydrogen tanks and lines to prevent air from freezing within and obstructing flow lines, with helium being the only viable purge gas.

The process of boil-off leads to an increase in pressure within the gaseous upper region of the liquid hydrogen tank, known as the ullage. This pressure must be vented upon reaching the tank's threshold. An accepted standard for boil-off rates in hydrogen aircraft suggests a maximum of 0.1% of the hydrogen weight per hour, emphasizing the importance of tank designs with low surface area-to-volume ratios to minimize thermal ingress [5]. The materials considered for tank construction include aluminum alloys, composite materials, stainless steel, and titanium alloys, with aluminum being favored for its high strength, resistance to hydrogen embrittlement, and affordability, making it a prime candidate for cryogenic tank walls. Although composites offer potential for weight reduction, their

higher costs and complex failure modes currently limit their application, although ongoing research into issues such as hydrogen permeation and thermal expansion optimization may eventually make them more viable [5]. The aluminum alloys utilized at low temperatures primarily consist of solution hardening and precipitation hardening (aging hardening) types. Solution hardening alloys typically include Al-Mg alloys (5000 series) and Al-Mn alloys (3000 series). On the other hand, precipitation hardening alloys mainly comprise Al-Cu-Mg alloys (2000 series), Al-Mg-Si alloys (6000 series), and Al-Zn-Mg alloys (7000 series) [100]. Table 2.4 summarizes the advantages and disadvantages of these materials. In terms of tank wall construction, there are two primary approaches: single-wall and

Table 2.4 Advantages and disadvantages of various liquid hydrogen storage tank wall materials [88].

Discriminators	**Metallic**	**Composite[a]**	**Hybrid construction[a]**
Advantages	Well established, currently in use; relatively low cost, easy to fabricate; insignificant permeation, alleviating need for permeation barrier.	Low mass; high specific strength and stiffness; tailorable properties.	Potential optimum design for lowest mass.
Disadvantages	Higher mass; high thermal conductivity; prone to embrittlement	Higher cost; prone to permeation by hydrogen; prone to microcracking due to constituent CTE mismatch; potential need for barrier or liner, resulting in component CTE mismatch issues; fabrication, processing, and joining issues.	Fabrication complexity; higher cost; CTE mismatch issues.

[a] CTE is coefficient of thermal expansion.

double-wall architectures [88]. Insulation likely relies on a high-vacuum-based system, which, as will be discussed in Section 2.3.2, necessitates a double-wall tank structure. However, as Adler et al. [5] highlight, the downside to vacuum-insulated tanks is their requirement for dual walls, which increases weight. Conversely, [24] argue that single-wall tanks, potentially insulated with foam, fail to meet the low heat flux requirements for aircraft applications, though they may suffice for short-term uses. Therefore, the decision between single and double-wall constructions involves a trade-off between system weight and performance efficiency.

2.3.2 Insulations

Insulation materials suited for cryogenic applications are typically classified into three categories: foams, bulk-fill, and layered insulations. Bulk-fill powder insulation include perlite, glass bubbles, and silica aerogels [30]. In aerospace applications, the insulation types frequently considered include foam, often termed spray-on foam insulation (SOFI), and vacuum-based insulation, or occasionally a combination of both [5].

Regarding the durability of these insulating materials, Colozza et al. [24] point out that foam insulation exhibits greater resistance to catastrophic failure compared to vacuum-jacketed insulation. Conversely, Adler et al. [5] argue that vacuum-based insulation methods offer higher reliability than foam-based systems. The primary disadvantage of vacuum-jacketed insulation is that any loss of vacuum results in insulation failure, leading to significant and rapid propellant boil-off. On the other hand, degradation in foam insulation occurs more gradually, predominantly due to thermal cycling, as detailed in subsection 2.3.4.

Multi-layer insulation (MLI) consists of multiple layers of highly reflective foil, which significantly reduces radiation heat transfer. This structure decreases thermal conductivity by two orders of magnitude compared to that of foam insulation. The reduced thermal conductivity associated with vacuum insulation leads to lower boil-off rates, enabling the initial fuel load to be minimized and the tanks to be smaller in size [5]. A typical MLI insulation system includes around 40 layers of double-aluminized Mylar with polyester net spacers [30]. Examples of foam and MLI insulation systems are illustrated in Fig. 2.7. As mentioned in Subsection 2.3.1, vacuum-based insulation requires a double-wall structure, whereas foam insulation is generally applied externally to the tank. The foam insulation system is composed of a buffer layer, a foam insulation layer, and a thermal protection layer, extending outward from the tank wall. The buffer layer serves as a thin layer of epoxy cryogenic glue to bond the foam to the substrate, also mitigating shear tension due to differences in thermal expansion between the substrate (typically aluminum) and the foam. The external surface of the foam layer is bonded with a thermal protection layer, consisting of a thin laminate of Kapton-aluminum-Kapton and glass cloth. This outer glass cloth enhances the damage tolerance of the surface, while the aluminum foil acts as the primary diffusion barrier, and the Kapton provides high temperature tensile strength and corrosion protection [148]. Finally, the advantages and disadvantages of the discussed insulating materials are illustrated in Tab. 2.5.

Table 2.5 Comparison of insulation materials for cryogenics tanks [88].

Location	**Insulation**	**Advantages/Disadvantages**
Outside	Foam (SOFI)	*Advantages*: Currently in use; well established; low cost; easy to implement; light weight; low density. *Disadvantages*: Limited to short duration missions due to excessive thermal conductivity; low resistance to thermal radiation; potential damage from environmental hazards.
Inside	Foam (SOFI)	*Advantages*: Low cost; structural wall not exposed to cryogenic conditions; reduced CTE mismatch issues of composite constituents. *Disadvantages*: Necessitates larger structural tank wall, resulting in increased mass; difficult to seal from cryogenic fluid; fluid infiltration leads to increased thermal conductivity; potential loss of structural wall integrity; may interfere with fluid management upon failure.
Between walls	Perlite	*Advantages*: Low cost; well established; some compressive load-bearing capability; resistance against thermal conductivity and radiation. *Disadvantages*: Limited to short duration due to excessive thermal conductivity; excessive mass for aerospace applications.
	Aerogel	*Advantages*: Extremely low thermal conductivity. *Disadvantages*: New material; not well characterized; limited mechanical properties.
	Vacuum	*Advantages*: Near zero thermal conductivity; well established. *Disadvantages*: Heavier tank walls required; costly to implement and maintain; no resistance to radiation heat transfer; catastrophic failure upon loss of vacuum.
	MLI	*Advantages*: Very low thermal conductivity and radiation heat transfer; extremely low density. *Disadvantages*: High vacuum required, heavier tank walls required; costly to implement and maintain; catastrophic failure upon loss of vacuum.

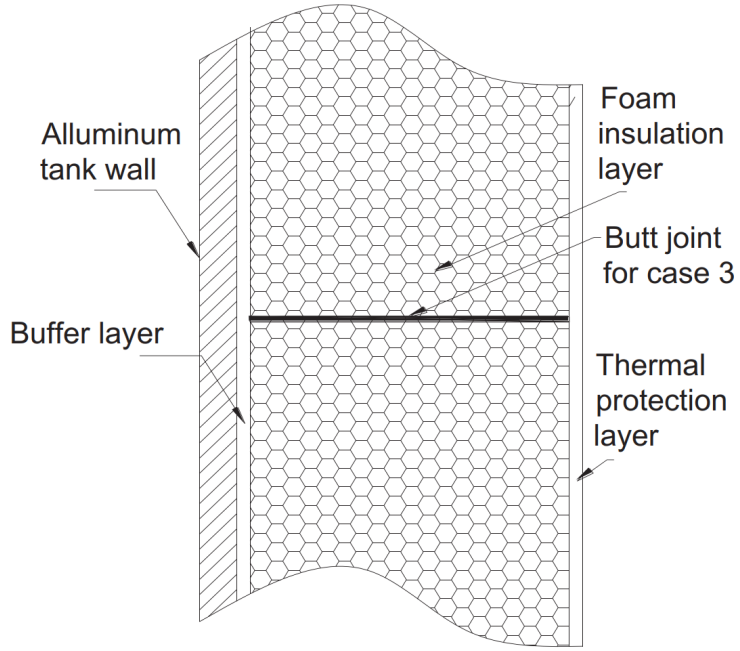

(a) Foam insulation system [148]

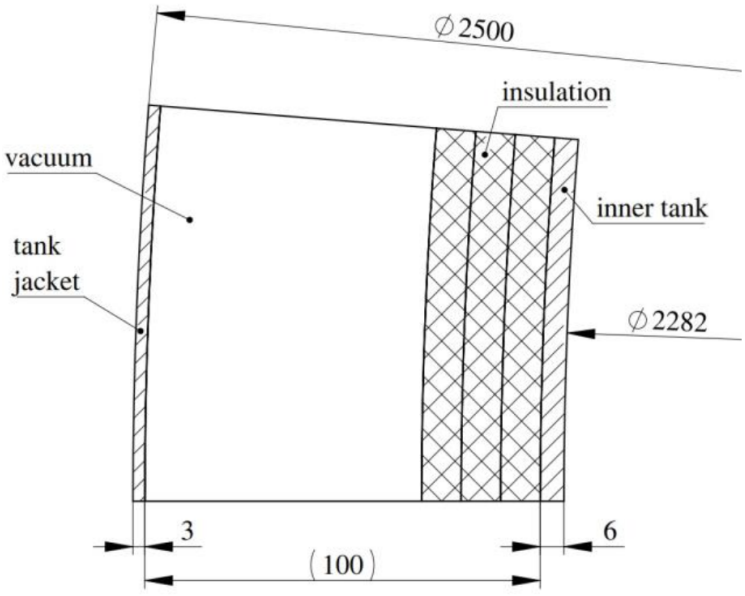

(b) MLI insulation system [30]

Figure 2.7 Overview of the insulation used in the application of cryogenic tanks.

2.3.3 Impact of mass rate filling on liquid hydrogen tank performance

During the design choices of filling time, filling level, and internal pressure in the liquid hydrogen filling processes, it is crucial to focus on the distribution of thermal stress within the tank wall due to its potential impact on tank safety. Thermal stress originates either from local temperature gradients within a solid or from the combined influences of temperature fluctuations and differences in thermal expansion coefficients among various materials [154].

Within the framework of the filling process for a liquid hydrogen storage tank, numerous factors need to be considered that may exacerbate thermal stress, even at reduced temperatures. These factors encompass:

- **Rapid Temperature Variations**: In the filling processes, the immediate interaction between the cryogenic liquid and the tank walls can result in significant and rapid temperature changes. These fluctuations can cause increased thermal gradients and, as a result, more intense thermal stresses [61];
- **Local Temperature Variations**: Although lower temperatures typically induce a compressive stress state, significant temperature gradients can lead to transient thermal stress concentrations in localized areas, especially during rapid filling or sloshing events [61];
- **Effects of Sloshing**: In scenarios where liquid sloshing occurs during the filling process, the tank contents might experience non-uniform accelerations and decelerations. Such movements can induce additional thermal stresses and affect the evaporation process [136].

During the filling of large-scale tanks with cryogenic liquids, the cooling process tends to be non-uniform, leading to significant thermal stress. The level of thermal stress in cryogenic tanks generally increases with the rate of filling. This correlation was evidenced in an experimental investigation by Kang et al. [61], who examined three different filling rates.

It was noted that both the overall cooling rate of the tank and the level of thermal stress within the tank wall escalated with the increase in the LN2 feeding rate. To alleviate transient thermal stress while optimizing the filling time, adjusting the feeding rates during a single filling operation is advisable. For instance, starting with an initial feeding rate of approximately 0.04 kg/s can decrease the thermal stress level from 41 MPa to below 15 MPa. Subsequently, a main stage with a feeding rate of 0.08 kg/s could expedite the filling process while managing thermal stresses effectively.

Regarding the methodology of filling, the research conducted by Zhu et al. [154] suggests that the top axial filling method might be the most suitable. Although the top lateral sprayer filling method achieves the quickest tank cooldown, it also leads to the highest

temperature gradients and the most intense thermal stresses. Conversely, the axial filling methods, especially the top axial approach, foster more uniform temperature distributions and reduced thermal stress levels. Notably, the peak thermal stress encountered with top axial filling is roughly 75% of that observed with bottom axial filling, despite similar patterns of thermal stress distribution.

In the context of Type III tanks utilized for cryogenic applications, a thermo-structural numerical analysis was performed by Kang et al. [60] and Kim et al. [65] on a cryogenic propellant tank composed of a metal liner and overwrapped composite layers. This analysis, which included both experimental and numerical approaches, evaluated the thermal stress distribution in circular ring specimens at cryogenic temperatures. The results indicated that while the composite layers were subjected to compressive stress, the metal liner experienced tensile stress, primarily due to the differing thermal expansion coefficients between the two materials.

Regarding Type IV tanks, Tapeinos et al. [118] state that liner cracking at the central hollow tube during pressure cycling after cryogenic chill-down is of primary concern. Although the structural integrity of the composite overwrap was not affected, the onset of liner damage should be avoided as it can lead to leaks and hydrogen embrittlement. Currently, Type IV tanks are not promising for cryogenic applications. Future work should focus on evaluating different liner materials for Type IV tanks, with an emphasis on addressing liner cracking by employing a polymer with a lower CTE [119].

2.3.4 Impact of pressure cycling at low temperature on cryogenic tanks

The design operating pressure of tanks, also referred to as the NWP or venting pressure, is a crucial consideration in the structural sizing of tanks. While lower design pressures may result in lighter tank walls, there are two critical factors necessitating higher design pressures. On one hand, the tank pressure must consistently exceed atmospheric (and cabin) pressure to prevent air ingress, which could form a combustible mixture. On the other hand, a higher venting pressure allows more liquid hydrogen to boil off before venting becomes necessary [5]. Tanks must be filled to at least 1.2 bar, maintaining a pressure slightly above atmospheric levels to prevent air from entering, which could lead to an explosive mixture [130].

ISO 21029-1 [55] assert that the capability of the inner vessel to withstand internal pressure shall be validated with the following test:

Inner vessels shall undergo a fatigue test of 10,000 cycles between atmospheric pressure and a pressure P_t, where:

$$P_t \geq 1.3(P_s + 1) \text{ bar} \tag{2.1}$$

where P_s denotes the NWP.

However, the standard highlights that when tests are carried out hydraulically, the pressure should be maintained for a sufficient duration to permit visual inspection of all surfaces and joints. The vessel must exhibit no signs of general plastic deformation.

Conversely, a pneumatic test using a gas may be conducted at the same test pressure value, but the visual inspection of the joints should occur at a pressure not exceeding 80% of the test pressure. Nonetheless, no information is provided regarding the effects that gas or liquid hydrogen could have on the cryogenic tank (such as temperature cycles and hydrogen embrittlement), while maintaining the same number of cycles as a reference. ISO 13985 [52] point out that the tank shall be designed to resist the following inner test pressure:

$$p_{\text{test}} = 1.3(\text{MWP} + 0.2) \tag{2.2}$$

where p_{test} is the test pressure, expressed in MPa; In addition, the inner tank and its accessories shall be designed to resist an outer pressure of 0.2 MPa.

However, for aluminum-lined, fiber-wrapped vessels, the standards defined by the Department of Transportation (DOT), the International Standards Organization (ISO), and the Society of Automotive Engineers (SAE) [15] may be referenced.

In the context of cryogenic composite tanks, Abumeri et al. [2] employed an aluminum sheet as a liner to prevent propellant leakage. The composite structure, incorporating carbon fiber and a modified epoxy matrix with a thermoplastic phase for enhanced toughness, is constructed around the liner using bonding material, acting as a galvanic barrier between the aluminum and carbon fibers, likely to mitigate issues arising from contact between materials with differing thermal expansion coefficients. The study indicates that under static loading, damage within the composite material initiates at an internal pressure approximately twice the designated operating pressure.

For LCFA, the results are based on the assumption that both the composite material and the liner attain a steady-state temperature equal to that of the propellant, specifically -20K. With a design pressure of 30 psi (2.068 bar), structural damage begins to occur once the cycle count reaches 100, and the liner is compromised at 600 cycles. The authors emphasize that after 1,000 cycles no fracture has occurred, indicating that the design concept is robust and effective. However, it is crucial to note that damage to the aluminum liner results in leakage, rendering the tank inoperative. Consequently, the tank is considered unusable once the liner is compromised. Furthermore, in environments subjected to vibrations or impacts, the presence of such damage could lead to catastrophic outcomes.

The study by Acevesa et al. [4] presents a comprehensive series of tests on aluminum-lined, fiber-wrapped vessels to evaluate damage incurred during low-temperature operations. Although not specified, the tank appears to be a Type III vessel used for compressed hydrogen tanks, introduced in Section 2.2. The pressure vessels underwent 900 high-pressure cycles, from 0 MPa to 25 MPa, along with 100 low-temperature cycles, following a pattern of nine pressure cycles followed by one temperature cycle, repeated 100 times. Remarkably, no failures were observed throughout the testing, and detailed inspection revealed no visible superficial damage. After cycling, burst tests were performed on both

aramid-aluminum and carbon fiber-aluminum pressure vessels. For the aramid-aluminum vessel, failure occurred through hoop mid-cylinder separation, a preferred failure mode, with a burst pressure of 94.2 MPa (13.7 ksi), significantly exceeding the minimum required burst pressure of 72.4 MPa (10.5 ksi). This discrepancy may be partly attributed to work hardening during cold cycling. Indeed, as described by Tobler et al. [122], considering the favorable effects of low temperatures on tensile, fatigue, and fracture properties, it is evident that the structural integrity of both flawed and flawless 5083-0 alloy components is not compromised at cryogenic temperatures, and the fatigue crack growth rates at such temperatures are significantly lower than at room temperature. Hence, it is deduced from these varied sources that pressure cycling processes, including filling and emptying of the tank, induce thermal stresses. These stresses affect the tank's fatigue life. Conversely, maintaining the tank at cryogenic temperatures, thus avoiding filling and emptying processes, positively impacts the tank's properties. This aspect will be explored in Chapter 4, where the advantages of maintaining a high level of liquid hydrogen fill will be introduced and demonstrated.

The study conducted by Aceves et al. [3] confirm the successful completion of the following tests:

- **Cycling, Ambient Temperature**: A total of 10,000 cycles, ranging from less than 10% to the service pressure, at a maximum rate of 10 cycles per minute.
- **Environmental cycling tests**: Conducted at a maximum rate of 10 cycles per minute, this test comprises: a) Condition for 48 hours at zero pressure, 60°C, and 95 percent humidity. b)5,000 cycles from zero to service pressure with the tank at 60°C temperature and 95% humidity. b) 5,000 cycles from zero to service pressure with the tank at -51.1°C and air at ambient temperature. c) 30 cycles from zero to service pressure under ambient conditions. d) Burst testing of the cycled vessel.
- **Cycling, Thermal**: Executed at a maximum rate of 10 cycles per minute, this test involves: a) 10,000 cycles from zero to service pressure at ambient temperature. b) 20 thermal cycles with the tank temperature varying from 93.3°C to -51.1°C at service pressure. c) Burst testing of the cycled vessel.

2.3.5 Impact of vibrations and environmental factors on insulation materials in cryogenic applications

Given the lack of data on the effect of vibrations on cryogenic tanks, the same considerations for materials investigated in Subsection 2.2.5 are applied, bearing in mind that vibrations undoubtedly impact the rate of crack propagation within materials [21]. Nonetheless, vibrations can significantly influence insulating materials. In most insulation schemes, the vacuum remains the central element, with damages due to loads or vibrations considered improbable, as emphasized by Cabulis et al. [19]. However, this does not imply that vibrations cannot indirectly degrade the vacuum state of the insulation, as if

Dewar	Material	Bulk Density (kg/m^3)	No. of Thermal/ Vibration Cycles	Compaction Level (mm)	Compaction Trend
D115	Aerogel beads	80	30	10	Stable
D116	Glass bubbles	60	30	0	Stable
D117	Perlite powder	100	30	15	Increasing

Figure 2.8 Measured bulk densities of insulation materials and final compaction levels and trends after thermal/vibration cycling [32].

vibrations contribute to the degradation of materials that encase and seal the vacuum state, then the vacuum itself will consequently degrade.

Moreover, vibrations are particularly crucial for three bulk-fill insulation materials: glass bubbles, perlite powder, and aerogel particles. Werlink et al. [137] conducted experiments on these materials to assess their mechanical behavior under vibrations. Glass bubbles and aerogel particles showed minimal compaction or settling compared to perlite powder. Specifically, the glass bubbles system, especially in vacuum-jacketed applications, could result in considerable product (and energy) savings worldwide. Conversely, the aerogel particles system, when used in double-wall (non-vacuum) setups, provides significantly better energy efficiency and enables the design of more effective tanks and piping systems.

A study conducted by Fesmire [32] involved thermal cycling and vibration tests across various bulk-fill materials. This research utilized four different bulk-fill insulation materials: perlite powder, glass bubbles, aerogel beads, and opacified aerogel beads. The aerogel beads demonstrated a total compaction of 10 mm after undergoing 30 cycles. In stark contrast, the glass bubbles showed negligible compaction after the same number of cycles, effectively remaining unchanged. Perlite, on the other hand, underwent compaction of approximately 15 mm after 30 cycles. These results are illustrated in Fig. 2.8.

He et al. [43] analyzed the vibration failure mechanism of Rigid Polyurethane Foam (RPUF) using Finite Element Analysis (FEA) and the Extended Finite Element Method (XFEM). Numerical simulations indicated that vibration stress concentration occurred in the center of the foam prism, making it susceptible to sliding and opening fatigue cracks during random vibrations. Additionally, the simulations suggested that vibration acceleration (GRMS) could promote the unstable propagation of microcracks.

The primary limitation of foam insulation is its inability to withstand repeated thermal cycles. For applications requiring aircraft maintenance or storage, the tank must alternate between cryogenic operating conditions and ambient temperatures without sustaining damage. As [5] assert, SOFI is particularly susceptible to cracking or delaminating from the tank's structural walls and may necessitate regular maintenance to maintain thermal performance. As a result, it is generally considered viable only for single-use launch vehicles. In contrast, transport aircraft are expected to conduct multiple flights per day and operate for extended periods between maintenance checks. Substantial advancements in foam insulation technology would be necessary to fulfill these demands. To mitigate

SOFI's limited tolerance for thermal cycling, it is plausible to retain some liquid hydrogen the tank to maintain cryogenic temperatures, except during extensive maintenance operations [5]. Regarding the impact of humidity on these insulators, Berardi [16] noted that high moisture levels significantly impair performance in all foam materials, with open-cell foams suffering the most pronounced reduction in thermal resistance. This finding is crucial as it illustrates how humidity can influence hydrogen evaporation by diminishing the performance of foam insulations. An example of the variation in thermal conductivity of SOFI insulation under normal environmental conditions is depicted in Fig. 2.9, highlighting how the thermal conductivity of the insulation increases over the months.

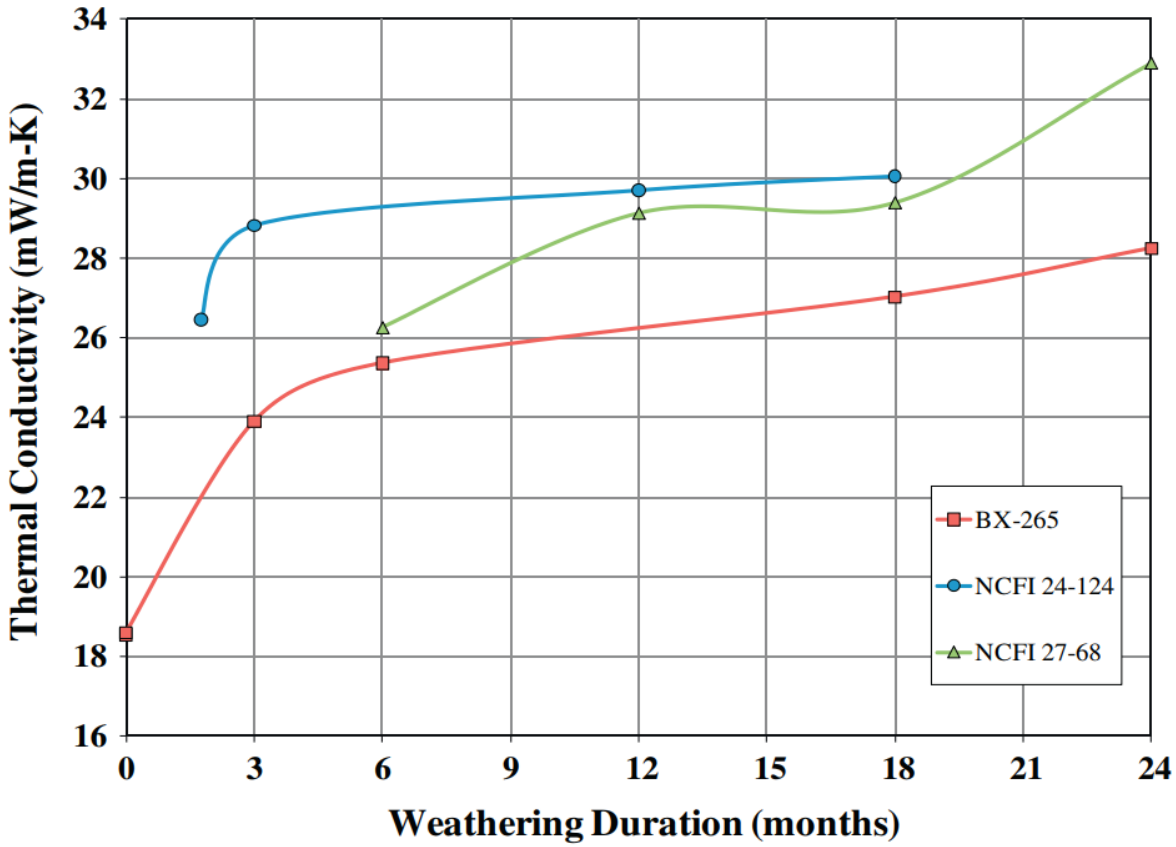

Figure 2.9 Variation in thermal conductivity with weathering duration for SOFI materials over two year [33].

Regarding the effects of thermal cycling and humidity on vacuum-jacketed and Multi-Layer Insulation (MLI) systems, there are no available data. However, to prevent the degradation of the performance of these insulators, it is crucial to avoid the use of a permeable liner. Hydrogen permeation through the materials used in composite cryogenic tanks can be problematic, especially when these tanks are designed for storing liquid hydrogen at cryogenic temperatures. This permeation may result in vacuum degradation, thus diminishing the efficacy of thermal insulation [110]. Therefore, without significant improvements in this domain, the use of vacuum and Multi-Layer Insulation (MLI) with

composite materials should be reevaluated. The decline of the vacuum state can lead to tank failure. Storage tanks experiencing vacuum failure exhibit markedly higher evaporation rates compared to those maintaining a stable vacuum, with the rates of evaporation increasing significantly within 3 to 6 hours, particularly in smaller tanks [96].

Regarding the effects of vibrations on hydrogen evaporation, [105] measured the boil-off rates of hydrogen from a cryogenic tank under various driving vibrations. They found that the rate of hydrogen evaporation is strongly dependent on the input vibration acceleration. No increase in boil-off rate was observed at low acceleration levels; however, with increasing levels of vibrations, the boil-off losses surged to as much as 12 times the value without motion. Additionally, the impact of vibrations on the boil-off rate was less pronounced for a partially filled tank. As vibration excitations intensified, the pressure within the tank increased beyond its original value. In scenarios with relatively high input accelerations, the evaporation rate was significant, and the tank pressure rose rapidly. However, during vibration, the stratification within the tank was disrupted, and the temperature field became more uniform due to fluid mixing, suggesting that initially, vibrations may have a beneficial effect.

The initial response to vibration excitation was a marked decrease in the pressure inside the tank, likely due to a rapid temperature change at the free liquid interface, which occurs once the liquid begins to move. However, when the tank is subjected to higher levels of acceleration, due to intense agitation, the input vibration energy absorbed by the liquid leads to heating of the bulk liquid and evaporation, thereby causing a rapid increase in pressure inside the tank.

2.3.6 Environmental factors impacting cryogenic tank behavior

Regarding the effects of external temperature, there is a scarcity of research on how varying ambient temperatures can influence the degradation of cryogenic tanks. However, changes in external temperature might significantly impact the boil-off rate and the operability of relief valves (a better insulation means that the external temperature has less influence on the evaporation of liquid hydrogen), as will be demonstrated in chapter 4.

Regarding the effect of external air pressure, if the aircraft fuselage environment is non-pressurized, the cryogenic tank is subjected to pressure cycles that alternate between ambient atmospheric pressure and the pressure of the surrounding air during high-altitude flight. Nevertheless, due to the absence of data on this issue, it is not possible to determine whether the effects of these cycles are significant.

When the outer wall of the tank is made of composite material or aluminum alloy, the considerations applicable to gaseous hydrogen tanks, as discussed in subsection 2.2.7, can be adopted. Reinforcing what has already been stated about aluminum alloys, according to Bray et al. [17], the crack growth rate can be up to ten times faster in moist air environments, a phenomenon also observed in other metals such as steel and titanium.

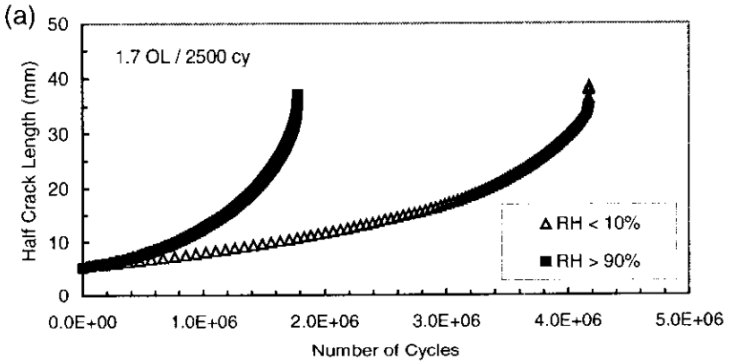

Figure 2.10 Effect of humidity in periodic overload tests on 2024-T351 plate[17].

Two principal mechanisms are proposed to explain the influence of moist air on the fatigue crack growth resistance of aluminum alloys: hydrogen embrittlement and the surface film effect.

The *surface film effect* refers to the impact of a thin surface layer that can form on the surface of aluminum alloys when exposed to humid air. This layer may consist of various compounds and oxides, resulting from the interaction between aluminum and atmospheric moisture. In the context of hydrogen embrittlement, it is theorized that water molecules react with freshly exposed aluminum metal during crack propagation, forming a hydrated surface layer. Hydrogen atoms released from this reaction diffuse into the plastic zone ahead of the crack tip, reducing the microstructure's ability to resist fatigue damage.

It has been demonstrated that crack growth rates in a humid environment can be up to 9 times faster in high humidity air compared to dry air, and the lifetime in high humidity air is only 40% of that in dry air. This is illustrated in Fig. 2.10 for a test conducted on the 2024-T351 aluminum alloy.

Furthermore, when the air surrounding the tank exhibits extreme humidity, it contains a high amount of water vapor. As the aircraft takes off and reaches cruising altitude, temperatures drop below zero. Consequently, when this humid atmospheric air contacts a cold surface with a temperature below 0°C, frost formation occurs. This is due to the solid deposition of water vapor on the surface. Although the layer of frost formation may initially seem to play a positive role by acting as insulation and reducing heat transfer into the tank once the ice layer has fully formed, it is important to consider the rate of heat transfer due to phase change at the moment the ice forms [64]. When this phase change occurs, the aircraft will be cruising, where the excess evaporated hydrogen will be supplied to the fuel cells. However, when the aircraft lands, this layer of ice will begin to thaw as soon as the surrounding ambient temperature increases. Initially, the defrosting process cools the temperatures of the surrounding surfaces through evaporation. Consequently, the rate of energy convection to the surrounding environment increases as water has a higher convection coefficient than air. In addition, when the tank is not subjected to freezing and thawing cycles, as demonstrated by [116], the tank will still experience an increase in heat transfer as the humidity increases. A topographical plot of the percent increase in heat transfer as a function of the fluid temperature and relative humidity is

shown in Fig. 2.11. Therefore, in every operational phase of the aircraft, humidity plays

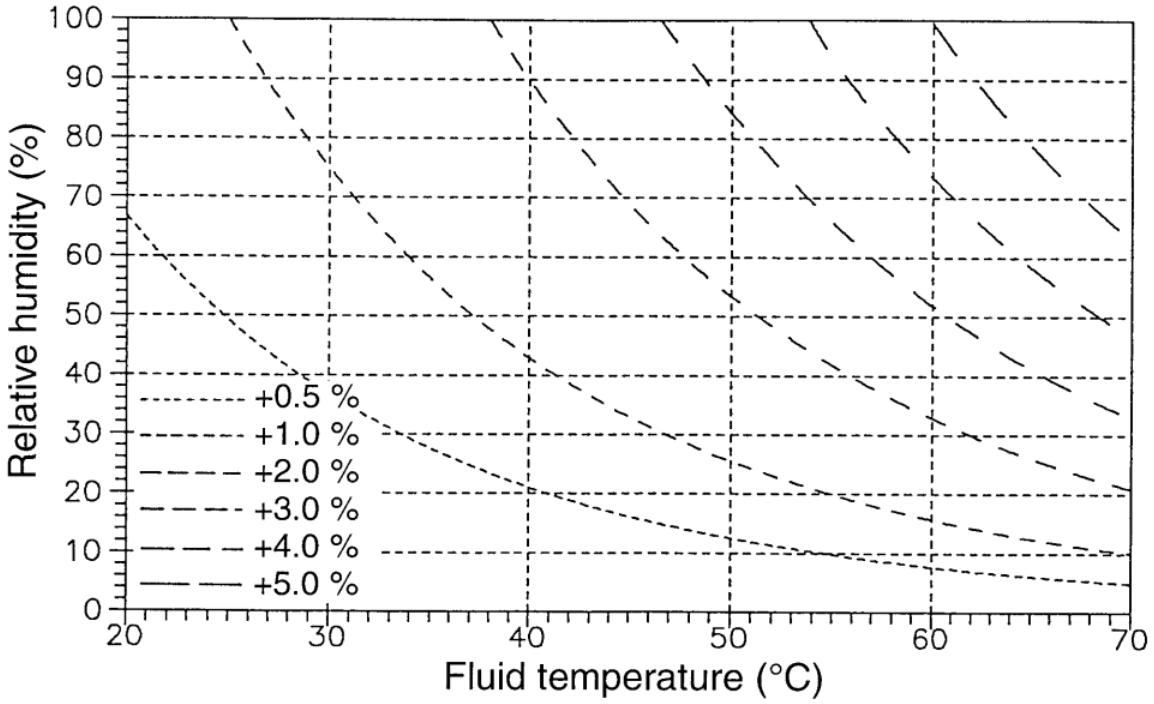

Figure 2.11 Percent increase in heat transfer as a function of the fluid temperature and relative humidity [116].

a fundamental role.

This aspect will be modeled in Chapter 3, where a thermodynamic model and a methodology will be introduced to assess a conservative approach in environments with high humidity levels.

2.4 Thermodynamic venting system and relief valves

In this section, the various valves used in cryogenic applications will be examined, as well as the different architectures and systems utilized for controlling the rate of hydrogen evaporation and the temperature of liquid hydrogen. Subsection 2.4.1 will introduce an overview of the definition of relief valves and their use, while Subsection 2.4.2 will introduce the different architectures that will be used in this study.

2.4.1 Relief valves: overview, applications and materials

A cryogenic tank, which maintains a temperature significantly higher than that of the propellant, experiences an increase in internal pressure due to the evaporation of liquid hydrogen into gaseous hydrogen. This heat transfer between the tank and its surroundings results in hydrogen boil-off. A comparison between the densities of gaseous and liquefied hydrogen indicates that the volume associated with the hydrogen boiling process increases drastically [85]. Thus, any additional pressure exceeding the tank's maximum operating pressure must be vented into the environment to prevent structural damage to the tank. This necessity underscores the requirement for a safety valve designed for cryogenic temperatures, which can open at a predetermined pressure to discharge the excess gas volume into the surroundings (for example, at the highest point of the aircraft [85]), thereby maintaining the pressure within safe limits. Moreover, the safety valve is crucial to avert catastrophic failure in the event of a rise in pressure caused by a malfunction in the stage pressurization system [81].

Safety valves encompass a range of devices engineered to relieve excess internal fluid pressure. They can be categorized into two main types: Pressure Relief Valve (PRV) and Pressure Safety Valve (PSV) [113]. Although PRVs and PSVs are often used interchangeably, they exhibit distinct differences. A safety valve is designed to open rapidly and fully once a predetermined pressure is reached, typically utilized in gas applications where system over-pressurization poses a safety or process hazard. It generally opens completely with a very slight increase beyond the set-point pressure and is designed to close only after the pressure has significantly dropped below the set pressure, ensuring complete deflation of the excess pressure. The Maximum Allowable Working Pressure (MAWP) of a system or pressure-containing vessel should be safeguarded with a safety valve. Conversely, a relief valve is tailored to open proportionally as the pressure increases beyond the set value. It is primarily used in liquid systems to moderate pressure by gradually increasing the opening as the pressure exceeds the set point. This valve is designed to open only as much as necessary to keep the pressure within safe limits, thus avoiding the complete discharge of fluid typical of safety valves [113]. In the context of cryogenic applications, safety valves are specifically referenced. Notably, [85] describes two types of resealable

safety valves: Category A and Category B valves. While Category A valves are intended for continuous operation with more than 20 opening and closing cycles per year, Category B valves are expected to operate sporadically, with fewer than 20 cycles.

In the hydrogen industry, various valve types are employed, as illustrated in Table 2.6. Sotoodeh et al. [114] list several materials used for valve applications at cryogenic temperatures, such as stainless steel 316, graphite, low alloy steel with hot dip galvanization, and carbon steel. These materials are capable of withstanding temperatures as low as -252.9°C.

Table 2.6 Valves used in the hydrogen industry [114].

	On/Off	**Flow Control**	**Non-return Function**	**Safety Function**
Valve Type	Ball valve	Globe valve	Swing check valve	Pressure safety valve
	Butterfly valve	Needle valve	Dual plate check valve	Pressure relief valve
	Wedge gate valve	Control valve	Piston check valve	
		Orbit ball valve	Axial check valve	
Construction Type	Bolted body pieces or body and bonnet	Bolted body pieces or body and bonnet	One-piece design	Bolted body and bonnet
	Welded body and bonnet	Welded body and bonnet		
Internal Operating Mechanical Element	Ball	V-shape ball	Ball	Disk
	Disk Wedge	Disk	Disk	

2.4.2 Thermodynamic venting systems and architectures

To prevent catastrophic failures of cryogenic tanks, Thermodynamic Vent Systems (TVS) have been identified as a promising solution for ensuring that only vapor is vented, rather than a liquid or liquid-vapor mixture [142]. An exemplary venting design has been explored by Meissner et al. [85], who have opted for a venting configuration that channels exhaust through the tail fin, allowing any lighter-than-air GH2 to exit at the highest point

of the aircraft, where any release into the atmosphere would ensure the avoidance of an explosive environment, as illustrated in Fig. 2.12. Through this design approach, once

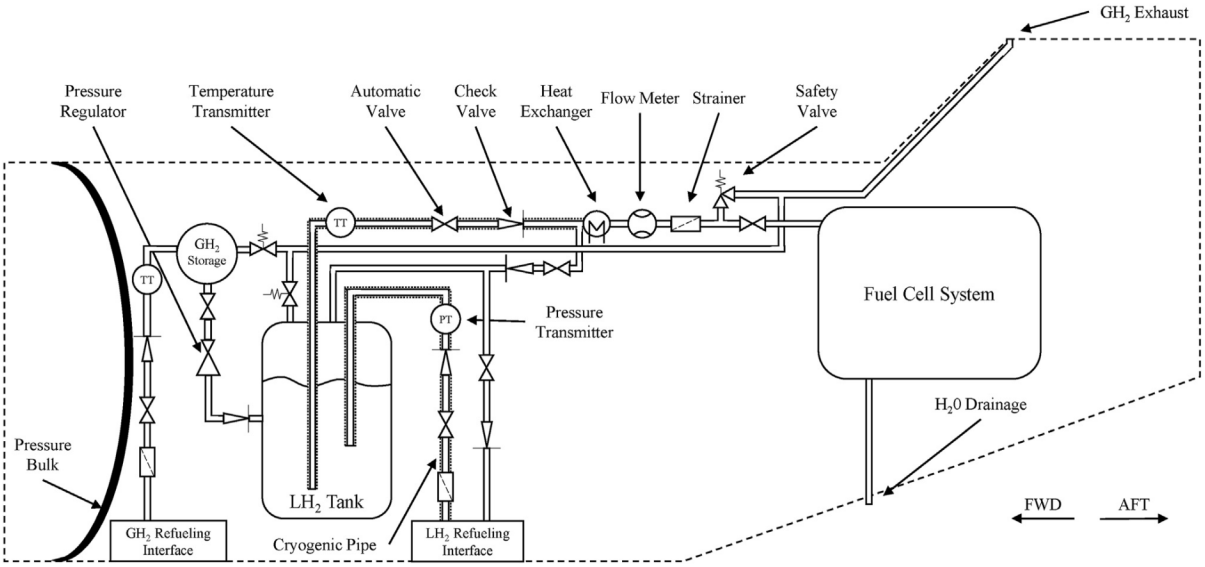

Figure 2.12 Schematic hydrogen system layout [85].

the tank reaches its maximum operating pressure or a target value, the resealable safety valves open and discharge the gas into the environment. By adopting this design principle, they argue that it could be possible to diminish technical complexity and enhance system reliability, as the system eliminates the need for pumps to transport liquid hydrogen to the vaporizer, thereby removing any associated pump maintenance and reducing hydrogen loss due to boil-off during the pumping process.

There are several methods to reduce the pressure increase within cryogenic tanks; for instance, NASA has developed innovative technologies such as high-performance thermal insulations, fluid mixing, and both passive and active thermodynamic vent systems [75], which are depicted in Fig. 2.13 [75]. Subfig. 2.13a summarizes the system considered by [85], where for a specific cryogenic storage tank, the heat leak causes thermal stratification in the fluid, generally leading to a higher rate of pressure rise in the tank compared to other configurations. Subfig. 2.13b is utilized to circulate and mix the tank fluid, eliminating temperature stratification and consequently reducing tank pressure. However, as mixer power is needed to circulate the fluid, additional energy is introduced into the system, eventually becoming heat and increasing the net fluid energy. Therefore, fluid mixing serves as a temporary solution for pressure reduction and is more suitable for short-term storage. The passive TVS concept (Subfig. 2.13c) includes components like a Joule-Thomson valve, a heat exchanger, a cryogenic pump, a vent valve, and connecting tubes. In this system, a small amount of liquid from the tank is drawn using a liquid-acquisition device and passed through a Joule-Thomson valve, leading to a lower pressure and temperature in the two-phase fluid. This mixture then passes through a TVS heat exchanger, cooling the tank fluid via passive energy exchange, mainly through thermal conduction or free convection. The fluid mixture is vaporized in the heat exchanger, and the resultant vapor is vented, thereby removing energy from the system by sacrific-

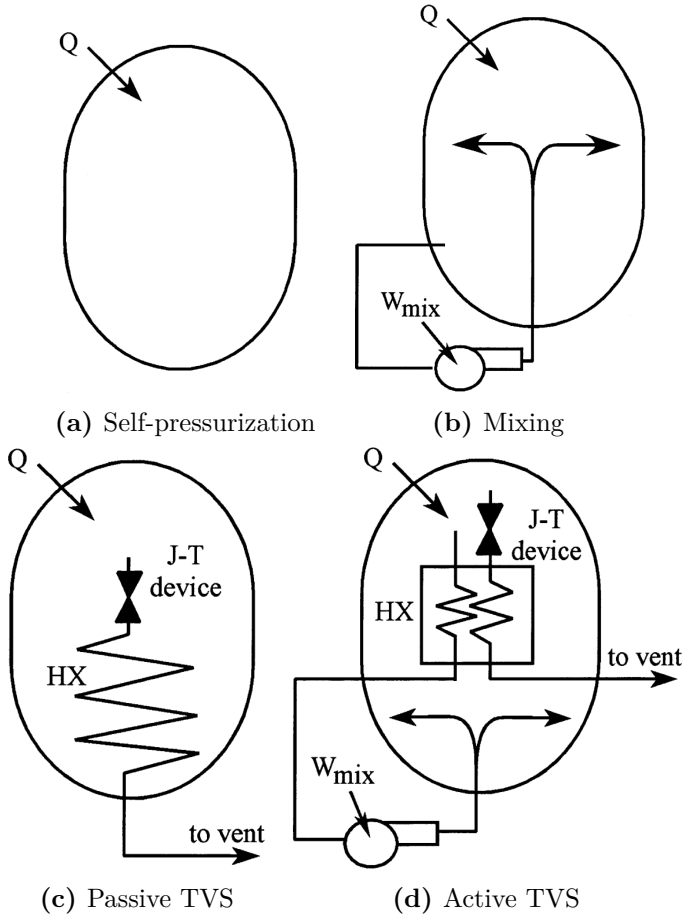

Figure 2.13 Schematic representation of self-pressurization and pressure control technologies [75].

ing a small amount of liquid. It is claimed that the passive TVS can be employed in long-term storage systems. Combining TVS and fluid-mixing techniques can lead to an efficient and quick-response pressure-control system, known as the active TVS, as shown in Subfig. 2.13d. The pressure control range is set above the initial tank pressure. When the ullage pressure exceeds the lower limit of the tank pressure control range, the re-circulation pump is activated. Initially, the ullage pressure decreases by spray-mixing vapor and liquid. However, once the tank pressure reaches the upper limit of the control range, mixing alone is insufficient to prevent excessive pressure increases. Then, a small amount of fluid passes through the Joule-Thomson valve and expands to a lower pressure and temperature state. This cooler stream absorbs heat from the re-circulation flow in the heat exchanger, then vaporizes and is vented to the atmosphere [133]. Nevertheless, systems operating at lower pressures might require a cryogenic pump to discharge gaseous hydrogen into the environment and may necessitate another cryogenic pump to supply hydrogen to the fuel cell's power system. Additionally, the inclusion of a re-circulation pump and other aforementioned components increases the system's complexity, weight, and potential maintenance requirements and efforts. Therefore, while these systems could maintain a more constant temperature inside the tank, reducing hydrogen evaporation and fuel consumption, the layout proposed by Meissner et al. [85] offers the substantial advantage of avoiding the use of cryogenic pumps and the introduction of other components,

which would add costs, maintenance efforts, and complexity to the system.

Regarding the effects of environmental factors and operating conditions on the degradation patterns of relief valves, there is no information available in the literature. For this reason, in the third chapter, a methodology will be implemented and introduced that will be capable of analyzing the indirect effect of these factors. Subsequently, in Chapter 4, it will be demonstrated that to minimize the indirect effect of these factors, it is crucial to choose an appropriate insulation.

2.5 Fuel cells

This section aims to provide an overview of the degradation processes affecting Fuel Cells, following an introduction to the operating principles in Subsection 2.5.1. From Section 2.5.2 to Subsection 2.5.6, the effects of various operating conditions (with particular emphasis on the effect of vibrations) and the impact of ambient temperature on such systems will be examined.

2.5.1 Fundamental principles and materials

A hydrogen fuel cell is a device that generates electricity through the chemical reaction between hydrogen and oxygen. Among the various fuel cell types considered for aircraft, the prominent ones are polymer electrolyte membrane fuel cells (PEMFC), also known as proton exchange membrane fuel cells, and solid-oxide fuel cells (SOFC). PEMFCs operate at relatively low temperatures (30–100°C) and exhibit rapid start-up and shutdown capabilities, making them advantageous. An elevated fuel cell temperature exceeding 80 °C leads to increased vapor pressure, resulting in water loss and heightened proton resistivity. Conversely, excessively low temperatures prompt water condensation and electrode flooding [59, 94].

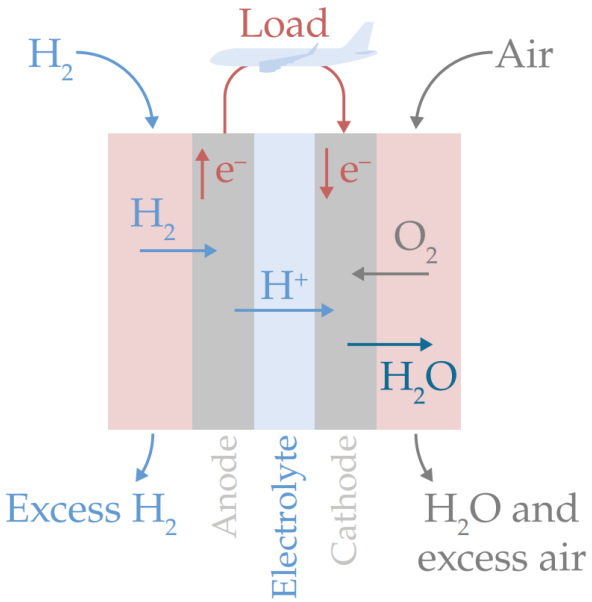

Figure 2.14 Chemical reactions of a PEMFC [5].

In hydrogen fuel cells, hydrogen is consumed at the negative electrode (anode), and oxygen is consumed at the positive electrode (cathode), with the latter typically drawn from the

ambient air. Electrons released during the hydrogen oxidation process flow through the circuit, powering the electrical load, as shown in Fig. 2.14. In the case of a PEMFC, positively-charged hydrogen ions migrate through the electrolyte, combining with oxygen and electrons at the cathode to form water. The efficiency of the fuel cell is directly proportional to the speed of the chemical reaction, influencing the amount of current produced. The electrolyte membrane, typically composed of Nafion—a polymer material resembling plastic wrap—requires consistent moisture to facilitate efficient conduction of positively-charged hydrogen ions. Conversely, the electrodes must avoid becoming inundated with water to prevent obstruction of their intricately designed porous structure [5].

As depicted in Fig. 2.15, the principal components in a single PEMFC comprise a membrane, two catalyst layers (CLs), two gas diffusion layers (GDLs), two flow channels, two distribution plates, a sealing channel, a gasket, and a MEA frame [149].

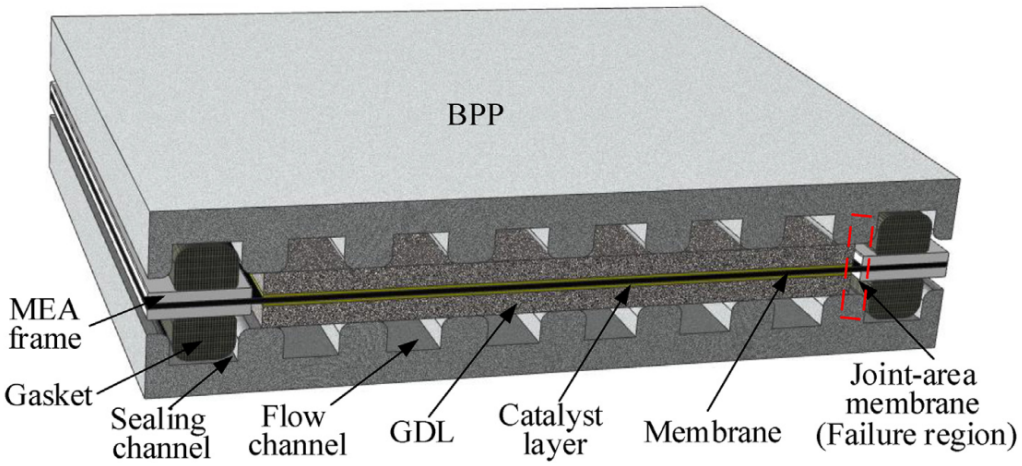

Figure 2.15 Schematic drawing of PEM fuel cell [98].

We can conceptualize fuel cells as a series of elements arranged in series, as illustrated in Fig. 2.16. In addition to the sealing elements, MEA frame, and gaskets, a cell is comprised of the following components: bipolar plate (BPP), anode gas diffusion layer (AGDL), anode catalyst layer (ACL), polymer electrolyte membrane (PEM), cathode catalyst layer (CCL), cathode gas diffusion layer (CGDL), and another bipolar plate (BPP) [149]. Considering multiple cells results in a Stack of Cells, with the exact number varying from a handful for low-power applications to several hundred for high-power applications, such as those required in aircraft [46]. The individual cell or stack of cells is then grouped by the end plates.

Figure 2.16 Breakdown of fuel cell.

2.5.2 Fuel cells degradation

Although the electrochemical and thermomechanical interactions among cell components (such as electrocatalysts, membranes, gas diffusion layers, and bipolar plates) influence durability, the membrane has been identified as a principal source of failure, encompassing mechanical damage and chemical degradation. Therefore, the membrane must possess sufficient durability to resist mechanical stresses and chemical attacks, ensuring that the fuel cell maintains its functionality under harsh internal operating conditions [69].

Literature reveals that the component most susceptible to degradation is the PEM, which is why this component will receive additional focus throughout this study. Unfortunately, the lifetime of fuel cells in laboratory settings is currently less than 3,000 hours if the membranes fail during operation [99]. It is noteworthy that fuel cell stacks intended for real transportation applications are required to operate under more severe conditions, which can hasten membrane failure. The US Department of Energy (DOE) [29] has established durability targets of 5,000 hours for automotive applications, which, as emphasized by Qiu et al. [99], have not been met by contemporary practical tests globally, suggesting that their relatively short lifespan remains a significant barrier to the commercial deployment of fuel cells.

Membrane degradation manifests in two primary forms: mechanical and chemical deteriorations, which synergistically lead to corresponding failures. Mechanical failure results from localized stress concentration and variations in mechanical stress applied to the constrained membrane during cycles of swelling and shrinking, which are responses to fluctuations in water content and temperature. This dynamic process can cause material fatigue, creep, and the development of wrinkles, delamination, pinholes, tears, or cracks, which might start and spread on the membrane's surface or throughout its bulk. The existence of inherent defects in the membrane, arising during fabrication or from improper assembly of fuel cell stacks, may intensify these problems [99]. The lifespan of a PEM can be divided into four distinct phases: the membrane fabrication process, the assembly of the fuel cell, and its short-term and long-term operational stages. A summary of the main factors affecting mechanical failure in membranes across these stages is provided in Table 2.7.

When fuel cell operation begins, the membrane experiences significant changes in stress states, influenced by variations in relative humidity and temperature, as humidified reactant gases are introduced at certain temperatures. For fuel cells, relative humidity serves a dual role, acting as both an environmental condition and an operational factor. During the operation of a fuel cell, cyclic changes in humidity and temperature are natural parts of the working environment. Under extreme conditions, these factors may lead to significant membrane failure. High levels of relative humidity and temperature cause in-plane compression and swelling of the membrane, while lower humidification and drier conditions result in in-plane tension and shrinkage. As a result, with variations in temperature and humidity, the PEM undergoes alternating cycles of expansion and contraction, amounting to fatigue cycles. Additionally, freeze-thaw cycles and weaknesses in the joint

Table 2.7 Concept table of proton exchange membrane degradation [99].

Process / Operation	**Factor Affecting Degradation**	**Specific Issue**
Fabrication Process	Membrane Defects	Thickness Variation
		Micro Crack
		Delamination
		Catalyst Orientation
		Electrolyte Cluster
		Pt Cluster
Assembly Process	Manufacturing Error	Dimensional Error
		Shape Error
		Assembly Error
	Assembly	Component Structure
		Endplate Deformation
		Assembly Force
	Bonding Frame	
Short-time Operation	Humidity and Temperature	Mechanical Strength
		In-plane Stress
		Plastic Deformation
	Freeze-Thaw Process	Sub-freezing Start-Up
	Failure along the Frame	
Long-time Operation	Cyclic Physical Loads	RH and Temperature
		Gas Flow
		Cell Vibration
	Chemical Acceleration	Molecular Structure
		Pt Dispersion
		Degradation Rate
	Effect of CL	

area between the membrane and the MEA can lead to rapid membrane failure, especially during the short-term operational phase.

In the long-term operation phase, repetitive swelling and shrinkage, variations in gas pressure, and chemical attacks during duty cycles pose significant mechanical challenges to the membrane. Consequently, fluctuating mechanical stress caused by swelling and shrinkage leads to the development of wrinkles, creep, and fatigue in the material. Over time, the cumulative effects of these processes contribute to the mechanical failure of the membrane, evidenced by the initiation and propagation of micro-pinholes or cracks, especially in areas with defects. Notably, in real-world operating conditions, this mechanical failure mechanism may be exacerbated by delamination from the CL and chemical degradation [63, 99].

2.5.3 Influence of operating temperature on the degradation of the membrane electrode assembly

The fatigue lifetime of the membrane is significantly influenced by the applied stress, temperature, and relative humidity. However, the impact of temperature is more pronounced than that of humidity, with a reduction in fatigue life observed at higher temperatures [79].

Regarding the operational temperature of fuel cells, increasing interest is shown in operating PEMFCs at temperatures around 120 °C. Higher operational temperatures present several benefits, including enhanced tolerance to carbon monoxide poisoning, improved water management, and increased efficiency of electrochemical reactions. However, the main disadvantage of operating at high temperatures is the accelerated degradation of most fuel cell components, especially the MEA. Thus, there is a pressing need to carefully assess the balance between performance and lifespan to determine which aspect proves more beneficial [78]. Nonetheless, this study does not focus on assessing which aspect is more advantageous but rather concentrates on how operational conditions impact the lifespan of Fuel Cells.

Catalyst Layers

The performance of Pt/C-type catalysts is highly sensitive to cell conditions, including electrode potential sweep, pH, relative humidity, and temperature. The predominant degradation mechanisms for Pt/C involve dissolution, agglomeration, detachment, and support corrosion. Preliminary studies on catalyst durability have shown that temperature significantly influences nanoparticle growth. Higher temperatures not only accelerate particle growth but also result in a marked reduction in small isolated particles, leading to a considerable decline in the electrochemical active surface area [78].

Catalyst support material

The durability of a PEMFC heavily relies on the catalyst support material. The corrosion of carbon support, mainly related to cell potential, significantly contributes to the degradation of the entire CL. The degree of carbon degradation largely depends on the morphology of the support material. For example, carbon nanofibers exhibit superior durability compared to carbon nanotubes and traditional commercial carbon support materials in thermal corrosion tests.

Research indicates that lowering the cell temperature closer to the freezing point of water enhances the durability of the support material. The reduction in ECSA due to carbon corrosion is minimized at 0°C, primarily due to reduced kinetics of carbon oxidation to CO/CO2. However, an increase in temperature to 20°C significantly accelerates the loss in ECSA [78].

Gas Diffusion Layer

In PEM fuel cells, the GDL plays a vital role in facilitating the transport of reactant gases from flow channels to the CL. The durability of the PEM fuel cell significantly relies on the stability of the GDL. Various degradation mechanisms can impact the GDL, including chemical degradation, erosion induced by gas flow, dissolution by water, freeze/thaw effects, and mechanical compression.

An investigation was conducted on the variations in cell resistivity through freeze/thaw cycles ranging from -30 °C to 70 °C. Different types of GDLs, such as carbon fabric, paper, and carbon felt, were utilized. The felt-type GDL exhibited minimal increases in the ohmic resistance of the cell (R_{ohm}), whereas both carbon fabric and paper-type GDLs showed a rapid increase in R_{ohm} [78].

Proton Exchange Membrane

In PEMFCs, the membrane situated between the two CLs is fundamental for proton transport, supporting the catalyst layers, and separating reactions at the anode and cathode sides. Consequently, an ideal membrane material should meet several requirements, including high proton and low electron conductivity, low fuel and oxidant permeability, as well as high mechanical and chemical stability, all while being cost-effective.

At temperatures above 100 °C, there is an increased risk of dehydration due to the evaporation of water from the membrane pores. This evaporation disrupts the hydrogen bond network, leading to a decrease in conductivity. Beyond affecting proton conductivity, dehydration at higher temperatures also negatively impacts the mechanical stability of the membrane. Prolonged exposure to dry conditions can cause the membrane to become brittle and lead to crack formation. This situation facilitates gas crossover and uncontrolled reactions between hydrogen and oxygen, leading to the creation of hot spots and pinhole formation, ultimately resulting in membrane failure.

Therefore, it is crucial to address the complex interactions between dehydration, mechanical, and chemical degradation, especially those accelerated at higher temperatures, to optimize the operation of PEMFCs at elevated temperatures [78].

2.5.4 Humidity cycling in polymer electrolyte membrane fuel cells

Humidity plays a pivotal role in the efficient operation of a fuel cell; for example, the combined impact of low humidity and localized temperature increase can create regions vulnerable to membrane failure [68]. During PEMFC operation, protons generated at the anode side are transported through the PEM to the cathode, moving within the membrane as hydrated protons carried by water. The higher the number of protons traversing through the membrane, the more water is transported from the anode to the cathode. As water moves through the membrane, its content decreases on the anode side while increasing on the cathode side. This concentration gradient leads to water back diffusion

towards the anode [78]. Referring to the work conducted by Song et al. [112] and Yan

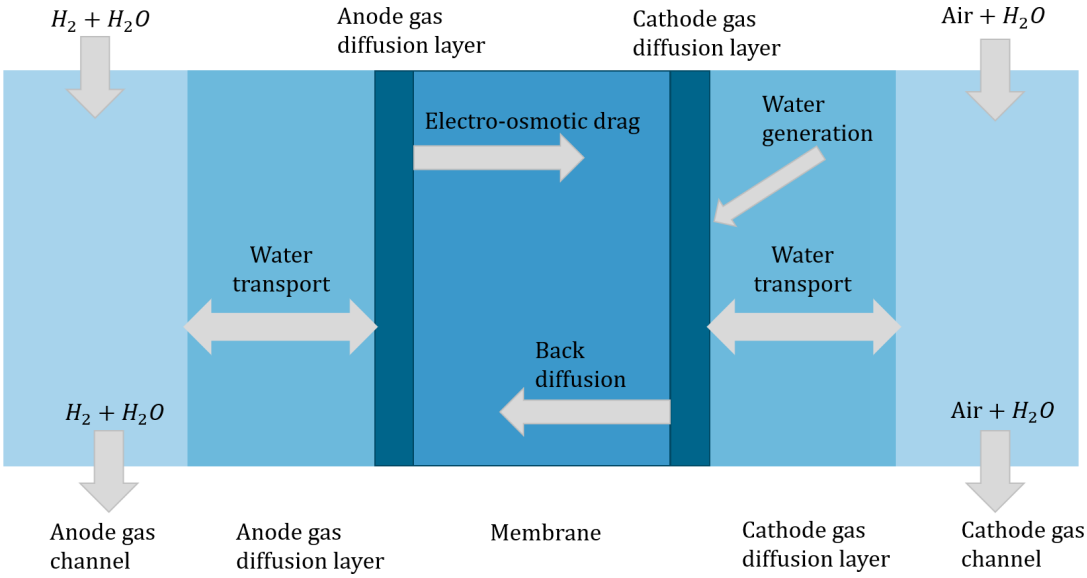

Figure 2.17 Schematic of the water transport process in typical hydrogen PEMFC.

et al. [143], the water transport modes in the PEM are illustrated in Fig. 2.17. Membrane dehydration results in poor proton transfer, reduced ionic conductivity, and increased ohmic resistance. To maintain the membrane sufficiently hydrated, hydrogen and air must be humidified. However, if the water content in the membrane is excessively high, liquid water can form from saturated water vapor, diluting the concentration of the reactive gas and blocking the pores of the GDL, leading to oxygen mass transport limitation. When membrane electrode dehydration occurs, membrane conductivity decreases, ohmic resistance increases, resulting in a significant fuel cell voltage loss. This leads to the fuel cell polarization curve decreasing with decreasing relative humidity. As the membrane resistance increases, the output voltage drops, requiring an increase in output current to achieve the same power. This results in an elevation of fuel cell temperature, further decreasing the RH and leading to a continuous deterioration in fuel cell performance [78].

As mentioned earlier, due to temperature and humidity fluctuations, PEMFCs undergo repetitive swelling and shrinkage cycles, resulting in fatigue cycles. Aindow et al. [6] proposed a model in which the internal stresses suffered by the membrane as a result of incellular moisture cycles can be simulated by mechanical fatigue tests. Thus, mechanical fatigue tests can be used to evaluate the resistance of the membrane to mechanical failure caused by moisture cycles. Mechanical fatigue testing was performed in a dynamic mechanical analyzer (DMA) at 60 °C and 90% relative humidity (RH) under different values of stress amplitude, and the results were used to plot the S–N curve. The stress amplitude for the S–N curve was then mapped to the equivalent change in RH as a methodology for characterizing membrane mechanical resistance to humidity cycling [6]. As shown in Fig. 2.18, for a durability requirement of 10^6 cycles, the maximum ΔRH to which the membrane could be subjected is $\propto 30\%$.

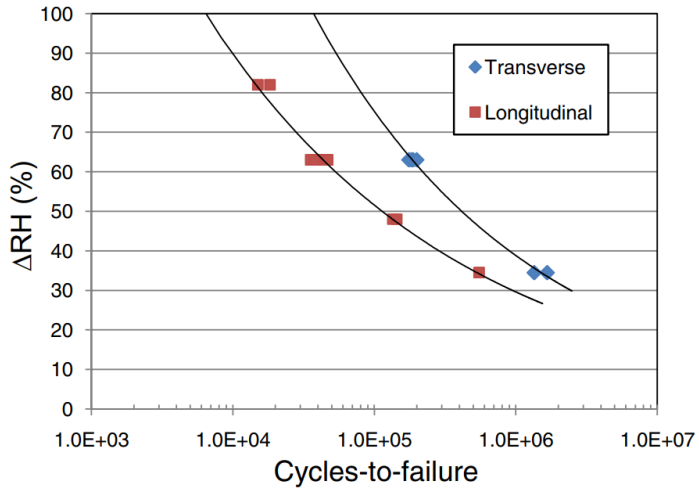

Figure 2.18 Membrane failure resistance (ΔRH–N) curves obtained by converting the stress amplitude in the S–N curves to an equivalent change in RH [6].

From these considerations, it is deduced that ensuring proper humidification of gases entering the flow channel is crucial for guaranteeing optimal functioning of both the PEMFC and the GDL. However, high ΔH values resulting from load variations or on/off cycles impact the fatigue life of the membrane. Therefore, ensuring that the membrane is consistently and appropriately well-humidified is essential to minimize these ΔH values as much as possible. Nevertheless, regarding the effect of the humidity of the air surrounding the fuel cell on its components, there is no information available.

2.5.5 Mechanical degradation during freeze-thaw process

Commercial airliners may be subjected to subfreezing operating conditions more severe than those experienced by vehicles, yet they undergo similar start-up procedures at subfreezing temperatures. Therefore, fuel cells must be capable of operating smoothly in low-temperature environments [99]. Water freezing inside pores may lead to mechanical damage due to an increase in volume when the water changes from liquid to ice [78]. For the membrane, various studies have verified that the thermal effect and freezing of residual water from the last operation are among the main problems leading to mechanical damage of the membrane. Regarding start-up at subfreezing temperatures, there are differing opinions. Some argue that the degradation of the fuel cell's start-up in a subfreezing temperature environment of -40°C is negligible, and degradation becomes significant only at extremely low temperatures such as -80°C [91]. However, other sources have demonstrated that significant physical damage occurs even at higher temperatures [22, 66, 99, 132, 144].

Yan et al. [144] investigated fuel cell cold-start under a wide range of operating conditions. Cell cold-start was examined at temperatures of -5°C, -10°C, and -15°C. Results showed that a single cell could start at -5°C if the cell was pre-purged and insulated. If the

fuel cell was shut down without purging, it could not be subsequently started up. The cell was capable of starting operation with the proper starting procedure at -10°C. With higher air stoichiometry and higher feed gas temperature at −10°C, it was possible to start up the cell using a current step from 0 to 100 mA cm^{-2}. However, if the current step was 0–200 mA cm^{-2}, the cell failed to start up Their results showed that the MEA, gas diffusion layer, and membrane in the fuel cell were damaged, leading to system failure or performance degradation.

Alink et al. [8] demonstrated that a fuel cell stack, which was dried before freezing after being subjected to repeated sub-zero cycles, exhibited slight performance degradation after 120 freeze-thaw cycles. Conversely, the stack that was frozen in the wet state showed serious degradation after 62 freeze-thaw cycles and 9 cold start-ups. Following multiple sub-zero exposures, steady-state operation at higher current densities became impossible due to flooding effects. The cathode electrode of the stack displayed an increase in porosity and a decrease in electrode surface area, while no cracks were found on the electrode surface, only micro-cavities.

Regarding operations at subfreezing temperatures, once again, Yan et al. [144] verified that fuel cell performance at chamber temperatures of 25°C, 0°C, -5°C, and -10°C remained stable and reproducible. However, at a chamber temperature of -15°C, fuel cell performance became unstable. After four cycles, the cell voltage decreased and suddenly collapsed to zero. This sudden collapse occurred with the cathode temperature below -5°C. Therefore, considering that operational conditions in commercial airliners may result in fuselage temperatures reaching -60°C during cruise phase, this could pose a significant barrier to the application of fuel cells in such environments.

McDonald et al. [84] conducted a study to understand the physical and chemical changes in fuel cell membranes resulting from freeze/thaw cycling. Nafion membranes and MEA were subjected to 385 temperature cycles between +80°C and -40°C over a three-month period to examine the effects on key properties. No catastrophic physical or chemical failures were observed in the dry freeze-thaw cycled fluoropolymer membranes and MEAs. However, a decrease in toughness, percent elongation, ultimate strength, and density was detected, as well as a reduction in the anisotropy of tensile strength. Nevertheless, this study was conducted considering an initial dry state of the PEMFC, which favors the possibility of sustaining these cycles at subzero temperatures.

These results suggest that minimizing the removal of water from the flow channels is essential for operation at sub-zero temperatures, considering its detrimental impact on membrane degradation. However, Qiu et al. [99] argue that a moderate amount of residual water from the last run is beneficial for proton conductivity and activation of the fuel cell. Therefore, the removal of water from the flow channels represents once again a compromise between degradation and performance of the fuel cell. In addition, under cold ambient conditions, typically below -30°C air temperature, a FCS needs assistance to start generating electricity in a short period of time [106].

Regarding the impact of reduced external air pressure at high altitudes, Chen et al. [20] argue that harsh environments characterized by low pressure and air deficiency can lead to damage to MEA and degradation of fuel cell performance. Nevertheless, it is posited that

while on one side, this challenge might be mitigated by increasing airflow and pressure, on the other side, excessive air stoichiometry and pressure could result in membrane drying. Consequently, the determination of optimal operating conditions emerges as a critical issue that warrants thorough investigation. This necessity also extends to the effects of atmospheric pressure variations, perceived as fatigue cycles, on the components of fuel cells.

2.5.6 Impact of vibrations of fuel cell

Reliability under mechanically harsh conditions remains a significant challenge for the commercialization of fuel cell technology in the automotive and aerospace industries. Extensive research, primarily through experimental and finite-element analysis, has been undertaken to evaluate the impact of vibrations on the integrity and performance of fuel cells. However, these studies yield inconclusive results: while some have identified considerable adverse effects on fuel cell performance, others have reported negligible impacts, and a few have even suggested that vibration could enhance fuel cell performance. This indicates that the outcomes of most studies are highly case-specific, with results and conclusions varying significantly from one scenario to another [39]. Nonetheless, this study exclusively reports the negative effects of vibrations on the durability, degradation, and performance of fuel cells. This conservative approach aims to determine the most suitable area in an aircraft to install fuel cells and to assess the potential benefits of employing vibration damping devices.

Hou et al. [48] investigated the effect of strengthened road vibration on the performance degradation of PEM fuel cell stacks, demonstrating a significant decrease in gas-tightness under prolonged, intensified road vibrations. Similarly, Imen et al. [49] revealed in their experiment that vibrations significantly degrade performance in terms of power output. Specifically, they conducted a 44-hour experiment comprising 11 steps, each lasting four hours, during which they observed a decrease in fuel cell power by approximately 0.6% per step, resulting in a total power reduction of 6.6%.

However, to assess the impact of different fuel cell placements within an aircraft, it is crucial to know the frequencies and amplitudes to which the fuel cells have been subjected.Banan et al. [9] presented the effects of external vibrations on the propagation of micro-scale defects (such as cracks and delaminations) in automotive PEM fuel cells. They subjected the cells to vibrations ranging from 5 to 40 Hz in frequency and from 1 to 4 g in amplitude, alongside hygrothermal cycles. They found that at a vibration condition of $A = 4$ g and $\omega = 40$ Hz, the delamination length reached 0.1 mm after 2.94×10^4 hygrothermal cycles, occurring 13% faster than in scenarios without vibrations (0.1 mm after 3.27×10^4 cycles).

A more detailed discussion on the effects of varying vibration amplitudes and frequencies was investigated by Banan et al. [10] in their previous work. They asserted that increasing the vibration amplitude results in a higher rate of delamination propagation for a constant vibration frequency of 40 Hz. It was also observed that crack propagation did

not occur for amplitudes less than 0.5 g, attributed to the insufficient force applied for crack propagation. The worst-case scenario was identified with $A = 4$ g and $\omega = 40$ Hz, while the best-case scenario was with $A = 1$ g and $\omega = 5$ Hz. In their final simulation at 300 hours, it was found that the delamination length increased threefold when increasing the frequency from 5 Hz to 40 Hz at $A = 4$ g, whereas at $A = 1$ g, the delamination increased twofold. Moreover, for $\omega = 40$ Hz, the increase in the final delamination length due to an increase of amplitude from 1 g to 4 g was approximately three times larger than the case with $\omega = 5$ Hz. Therefore, delamination propagation is significantly influenced by both amplitude and frequency, with the impact of vibration frequency becoming more pronounced at higher amplitudes.

2.6 Basic concepts of maintenance in civil aviation

In this section, starting from Subsection 2.6.1, an overview of maintenance will be introduced, followed by a discussion of various maintenance policies in Subsection 2.6.2. In Subsection 2.6.3, the models and mathematical parameters that will be used in this study will be defined. Finally, in Subsection 2.6.4, the failure rates analyzed in this study will be defined and introduced.

2.6.1 Maintenance overview

Aircraft maintenance (*Maintenance, Repair, and Overhaul – MRO*) is regulated by the EASA Implementing Rule Continuing Airworthiness (Part 145) [45]. Once aircraft are delivered post-production, it is imperative to ensure they continuously maintain airworthy condition throughout their operation; this necessitates regular inspections and maintenance activities.

Like other technical systems, aircraft are subject to wear and tear. Therefore, the service life of many aircraft components is limited. To guarantee long-term airworthiness, it is essential to ensure that fatigue damage, environmental wear, and accident damage are identified in a timely manner to prevent a critical extension. The necessary measures for this purpose must be structured and defined for the entire operational life-cycle of the aircraft and its components [47].

The term *maintenance* is defined in the DIN 31051 standard as the combination of all technical, administrative, and managerial actions during the lifecycle of a unit under scrutiny, to maintain or restore it to a condition in which it can perform the required function [47]. Maintenance can be perceived as a multidisciplinary activity encompassing the understanding of degradation mechanisms and their correlation through data collection and analysis, providing quantitative models to predict the effects of different maintenance measures, and the strategic management of maintenance. Systems and components of a facility, vehicle, or aircraft are prone to degradation and wear. Without countermeasures, this will eventually lead to the failure of the concerned unit. A unit is considered failed if it is no longer able to perform its intended function [47]. For instance, in the context of pressure vessels, *vessel failure* is defined as a condition wherein a crack, leak, or other defect has occurred in the pressure-retaining components of the vessel, necessitating repair or replacement [97]. Understanding failure behavior is a prerequisite for determining an effective and efficient maintenance strategy.

A component, system, vehicle, or aircraft is subjected to various stresses throughout its lifecycle. Tab. 2.8 illustrates examples of stresses that can act individually or in combination, leading to performance decline and physical degradation, thus reducing the product's useful life.

Table 2.8 Stress conditions [47].

Stress type	Stress conditions
Thermal	Stationary temperature
	Temperature spans
	Temperature cycles
	Temperature gradients
	Heating rates
	Heat dissipation
Mechanical	Pressure magnitude
	Pressure gradient
	Vibration
	Shock load
	Buckling
	Compressive and tensile stress
Chemical	Aggressive vs. inert environment
	Humidity level
	Contamination
	Ozone
	Pollution
	Fuel spills
Physical	Radiation
	Electromagnetic interference
	Barometric altitude
Electrical	Current strength
	Voltage
	Power
	Resistance

2.6.2 Maintenance strategies

A maintenance strategy is a management approach crafted to fulfill predefined maintenance goals. Specifically, a maintenance strategy encompasses guidelines that dictate the necessary maintenance activities upon the occurrence of particular events, such as equipment failure, reaching time or usage thresholds, or exceeding condition limits [47]. An aircraft, analogous to an automobile, incorporates specific components that necessitate regular inspections at predetermined intervals, or require proactive replacement due to particular requirements, to maintain their operational condition. These prearranged and thus anticipated maintenance activities are commonly referred to as scheduled maintenance and constitute the standard task suite during a layover. The considerable volume of such predetermined maintenance tasks aids in facilitating the planning process, enabling the meticulous organization of personnel, documentation, materials, as well as the necessary equipment and tools [45]. The type and extent of routine maintenance actions can be found in the Maintenance Planning Document (MPD) and are tailored within a

maintenance program by the aircraft operators. For each aircraft and each inspection, specific measures are delineated that must be routinely carried out. Through referencing the MPD, maintenance measures are elaborated in detail on the job cards, which also provide an estimated duration for the execution of the work [45]. Scheduled maintenance tasks, which can be systematically organized by time, type, and extent, include procedures like inspections, condition monitoring, calibration, or part replacements [47].

Prior to exploring various maintenance strategies, it is crucial to differentiate between scheduled and unscheduled maintenance. When malfunctions or damages are encountered during operation or are identified during a maintenance session, and if their correction is not encompassed by standard job cards, such instances are classified as non-routine tasks. Examples of these include issues like corrosion or wear and tear. Consequently, non-routine maintenance represents a form of unplanned maintenance, which is also referred to as unscheduled maintenance [45]. Within the domain of aviation maintenance, a further classification exists between routine and non-routine maintenance. Routine maintenance comprises actions delineated within a maintenance program and executed consistently. Notably, while all routine maintenance is scheduled, not all scheduled maintenance qualifies as routine. Non-routine maintenance consists of procedures not listed in the maintenance program but undertaken due to operational malfunctions or damages identified during standard checks [47].

The academic literature presents various maintenance strategies [28, 47, 82]:

- **Breakdown or Corrective Maintenance**: This run-to-failure approach involves maintenance after a failure is identified to restore functionality. While minimal maintenance organization and maximal component usage are benefits, this strategy suffers from unpredictable maintenance schedules and the lowest reliability.
- **Preventive maintenance**: This strategy focuses on pre-emptive actions to prevent system failures. It encompasses statistically and reliability-based maintenance, targeting component use and age, and condition-based preventive maintenance, monitoring operational parameters.
- **Fault finding**: Activities under this category aim at detecting faults through systematic inspection.
- **Overhaul**: This involves comprehensive analysis and adjustment to restore components or systems to acceptable operational standards.
- **Predictive maintenance**: Defined as condition-based maintenance conducted according to predictive analyses, this strategy aims to forecast the remaining lifespan of components to schedule timely interventions. This approach, which enhances system reliability, entails steps such as data acquisition, feature extraction, diagnostics, and prognostics, albeit requiring considerable investment.

These strategies are collectively illustrated in Fig. 2.19. However, it is imperative to acknowledge that no single approach holds universal superiority. Often, multiple maintenance strategies are employed concurrently to optimize the effectiveness and efficiency of maintenance procedures. This amalgamation of strategies enables organizations to tailor

their maintenance programs to meet specific operational needs and enhance overall system reliability and performance [82].

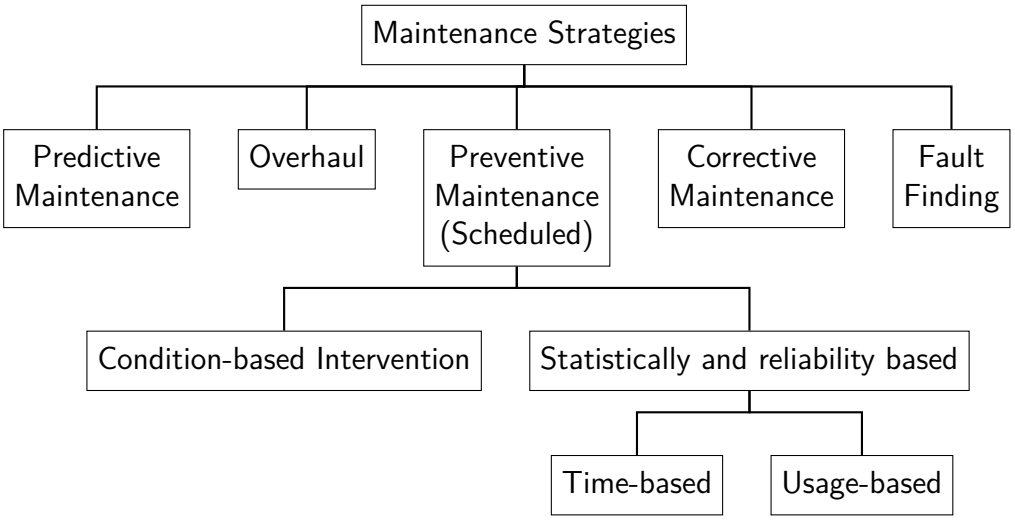

Figure 2.19 Hierarchy of maintenance strategies [82].

2.6.3 Mathematical methods for preventive maintenance

To determine maintenance intervals, Meissner et al. [85] highlights three distinct alternatives: comparative analysis of existing standards, statistical analysis of historical failure rates, and failure degradation models based on life-cycle experiments. The first approach involves deriving initial maintenance interval estimates from existing standards, such as those set by the ISO. However, since these standards are generally developed for ground-based industrial applications rather than aerospace uses, they may not adequately reflect the severity of functional failure consequences or meet the specific reliability requirements for aerospace systems.

The second approach employs statistical models—typically Poisson and Weibull distributions—utilizing historical data on failure rates for both repairable and non-repairable items. Although this method does not prevent part failure outright, it facilitates timely repairs, ensuring no operational interruptions at the system level.

The third approach involves developing physical models to gain an in-depth understanding of component degradation behavior, leading to predictive maintenance. As previously mentioned, predictive maintenance relies on condition monitoring and diagnostic techniques to forecast potential failures, allowing maintenance actions to be executed just before failures occur.

To address the gaps posed by ISO standards, a methodology is adopted that examines the second approach (historical failure rates) and modifies it. The objective is to understand

how failure rates identified in literature vary with changing operating conditions and environmental factors, through the analysis of previously conducted laboratory tests or experiments found in literature, with the aim of producing degradation patterns of aircraft systems for various operational and environmental conditions.

Key metrics for describing the reliability or failure rate of products include the reliability function and the failure rate. The failure density function $f(t)$ at time t is derived from the reliability function $R(t)$ and the reliability at time t is defined as:

$$f(t) = \frac{dF(t)}{dt} = -\frac{dR(t)}{dt} \tag{2.3}$$

For the time-dependent failure rate $\lambda(t)$ applies:

$$\lambda(t) = \frac{f(t)}{R(t)} \tag{2.4}$$

A commonly used metric for describing the reliability of products is the Mean Time Between Failures (MTBF). The MTBF can be determined according as follows:

$$MTBF = \int_0^\infty t f(t) dt \tag{2.5}$$

In the case of a constant failure rate, it is given by:

$$MTBF = \frac{1}{\lambda} \tag{2.6}$$

Especially in aviation, a frequently used reliability measure is the Mean Time Between Unscheduled Removals (MTBUR). Removal in this context is triggered by a fault report, meaning an error or malfunction. Similarly, the Mean Time Between Removals (MTBR) includes the average time between removals or exchanges in the context of preventive maintenance [47].

However, Manzini et al. [82] assert that the distinction between repairable and non-repairable components is fundamental, since the mathematical models describing their failure behaviors differ significantly. The term *non-repairable* refers to components that cannot be repaired once they fail and are typically replaced instead; while *repairable* components can be fixed after failure and thus are subject to multiple cycles of operation, failure, and repair. It is important to note that components, often not returning to their optimal initial conditions after repair, should be considered to have an increased failure rate once repaired. A system comprising both repairable and non-repairable components, whose operation depends on all components, is inherently non-repairable, since the failure of a non-repairable component halts the entire system. For example, a complex system (e.g., a nuclear plant, a refinery) consisting of both repairable and non-repairable components is modeled, in a preliminary analysis, as if it were non-repairable, for the purpose of

studying what is defined as the system's behavior at first failure or *catastrophic breakdown* (e.g., an explosion at the plant).

Subsequently, reliability is quantified as MTBF for repairable product and MTTF for non-repairable product [115]. The typical trends of the conditional failure rate are depicted in

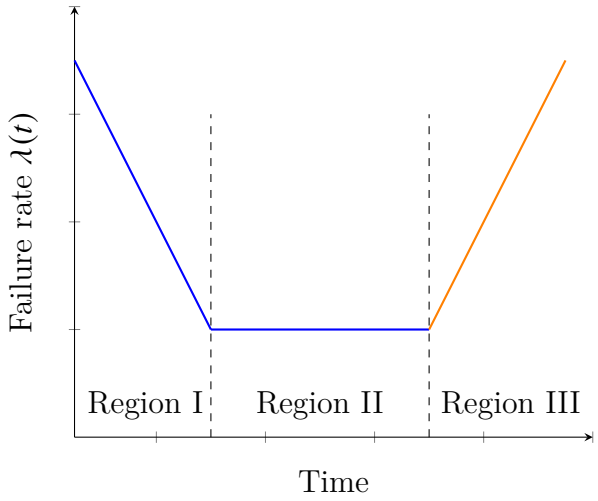

Figure 2.20 Bathtub curve.

Fig. 2.20. This trend, known as the *bathtub curve*, is initially decreasing (component run-in phase) due to early failures, constant for a time interval (useful life of the component), and finally increasing (component wear phase). This behavior is representative of a large portion of mechanical components (and complex mechanical systems) subject to wear. The component undergoes progressive aging (degradation) characterized by an increase in the rate of breakdown [82].

Mathematically, the most important failure patterns can be described using the Weibull and Exponential distributions. The Exponential distribution is a frequently used probability distribution function in the areas of maintenance and reliability. It is simple to manage with its constant failure rate, making it suitable for describing the failure behavior of many technical units over their lifespan. The probability density function $f(t)$ is defined as follows:

$$f(t) = \lambda e^{-\lambda t} \quad \text{for } t \geq 0, \lambda > 0 \tag{2.7}$$

The cumulative distribution function $F(t)$ is given by:

$$F(t) = \int_0^t \lambda e^{-\lambda x} dx = 1 - e^{-\lambda t} \tag{2.8}$$

The Weibull distribution can be used to describe various physical phenomena and thus different failure behaviors. The probability density function of the Weibull distribution is described by the distribution parameter β and the form parameter α as follows:

$$f(t) = \frac{\beta}{\alpha^{\beta}} t^{\beta-1} e^{-(t/\alpha)^{\beta}} \quad \text{for } t \geq 0, \alpha > 0, \beta > 0 \tag{2.9}$$

And the cumulative distribution function $F(t)$ is:

$$F(t) = \int_0^t \frac{\beta}{\alpha^{\beta}} x^{\beta-1} e^{-(x/\alpha)^{\beta}} dx = 1 - e^{-(t/\alpha)^{\beta}} \tag{2.10}$$

The exponential distribution represents a special case of the Weibull distribution when the shape parameter $\beta = 1$. Besides these (and other) parametric distribution functions, the use of non-parametric failure distribution functions may be necessary in real problems when the observed failure behavior does not fit any other known function [47].

2.6.4 Investigation and evaluation of failure rates

Type III and Type IV Vessel

Concerning the failure rates of Type III and IV gaseous hydrogen tanks, this study will consider the number of fatigue cycles performed as detailed in the extensive documentation provided. For these types of tanks, reference will be made to the number of cycles obtained under normal atmospheric conditions conducted with hydraulic tests (to compare the gap in ISO standards). Considering the data discussed in Subsection 2.2.3, the failure rates of Type III and Type IV tanks will be calculated as follows:

$$\lambda_{TypeIII} = \frac{1}{93,883} \left[\frac{1}{\text{cycles}} \right]$$

$$\lambda_{TypeIV} = \frac{1}{94,000} \left[\frac{1}{\text{cycles}} \right]$$

As highlighted in Subsection 2.2.3, Tomioka et al. [123] subjected Type IV tanks directly to a NWP of 150%, as these types of tanks are more resistant to pressure cycles. Therefore, with the aim of adopting a conservative approach for this study, it is assumed that at 100% of the NWP, the Type IV tanks are capable of enduring 94,000 pressure cycles, which are equivalent to 94,000 FlCs. As Meissner et al. [85] point out, a visual inspection of the external tank structure will have to be performed at that interval.

Cryogenic Tank

Regarding the failure rates of tanks used for cryogenic applications, Meissner et al. [85] adopt a failure rate of $\lambda = 1.6 \times 10^{-6}$ per hour, whereas Pelto et al. [95] propose a value of $\lambda = 1 \times 10^{-9}$ per hour, and Abu Kasim et al. [1] opt for a rate of $\lambda = 1.8 \times 10^{-10}$.

However, these studies do not elucidate the specific nature of the failure rates, such as whether they were determined while maintaining the tank at operating pressure and temperature without undergoing any cycles, or whether they involved cycles of temperature and pressure.

Furthermore, Rosyid et al. [104] suggest that the specific impact of hydrogen on the lifespan of materials under cyclic loads (such as filling and emptying) could be considered by multiplying the failure rates of the exposed parts (for instance, the spontaneous failure of the tank) by a factor of 6. However this approach, particularly in critical and scientific contexts such as civil aviation, may not be considered.

For this study, the most conservative value proposed by [85] will be adopted as a reference. Given the ambiguous nature of the aforementioned failure rates, for subsequent assessments, an introduction is made to a failure rate that depends on the number of cycles of a cryogenic tank subjected to temperature and pressure cycles. By deducing the number of cycles that a cryogenic tank may endure from Subsection 2.3.4, a failure rate of $\lambda = \frac{1}{600}[\frac{1}{\text{cycles}}]$ is obtained, which is significantly high.

Fuel Cell

Collong et al. [23] introduces an average failure rate for leakage due to PEMFC degradation of $\lambda = 7.34 \times 10^{-5}$, while [1] reports a fuel cell stack failure rate $\lambda = 5.5 \times 10^{-5}$, resulting in the cessation of current production. However, as previously discussed in Subsection 2.5.3, the recent study by [99] indicates that the lifespan of fuel cells in laboratory conditions currently does not exceed 3,000 hours if the membranes fail during operation, emphasizing that fuel cell stacks for actual transportation applications must endure much harsher conditions, which accelerate membrane degradation. Nevertheless, there appears to be a divergence between the failure rates reported in the literature and those observed in the latest laboratory tests.

Relief and Cryogenic Valves

Regarding the failure rates of relief valves used in cryogenic applications, there is a lack of information, thus necessitating the performance of new laboratory tests. However, in Chapter 3, a methodology will be introduced for assessing the theoretical failure rate of relief valves for cryogenic applications, based on the number of cycles they are required by standards to withstand in such applications.

Concerning cryogenic valves, the following values corresponding to the valve sub-components have been identified in the literature:

Table 2.9 Estimated failure rates for cryogenic valve sub-components [35].

Valve component	**Failure rate**
Metallic Bellows	from 10^{-4} to 10^{-5} fails per valve per year
Seat Seal	10^{-3} fails per valve per year (first year)
	from 10^{-4} to 10^{-5} fails per valve per year (following years)
Static Seal	from 10^{-5} to 10^{-6} fails per valve per year
Pneumatic Actuator	from 10^{-6} to 10^{-7} fails per valve per year

Regarding cryogenic check valves, Veenstra et al. [126] have revealed through an accelerated lifetime test consisting of 300,000 cycles that there was no leakage flow through the valve after the initial 100,000 cycles.

However, there is a significant gap in the literature regarding the failure rates of the components considered for this study. Furthermore, there is a lack of scientific evidence and sufficient documentation for the few failure rates available.

3 Methodology

This chapter embarks a systematic methodology aimed at evaluating and analyzing the impact of various operating conditions and environmental factors on the structural integrity and performance of critical components within hydrogen-powered aircraft.

The methodology described employs a structured approach to derive metrics and factors that characterize different operating and environmental conditions. Moreover, parameters to delineate various system design approaches, such as the utilization of different materials, insulations, and the placement of components in various parts of the aircraft are proposed.

The adoption of these metrics and factors will facilitate the evaluation of diverse scenarios, offering a comprehensive framework for application under real-world operational and environmental conditions. Section 3.1 will introduce a methodology to calculate degradation indices for each component, enabling the computation of failure rate trends as operating conditions and environmental factors vary, thereby aiding in the assessment of maintenance efforts.

Given the lack of literature on the effects of operating and environmental conditions on the degradation of relief valves, Section 3.2 will introduce a thermodynamic model aimed at performing computational analysis to calculate the number of operating cycles of relief valves. Through this methodology, it will be possible to assess how various design variables, such as tank geometry, types of insulating materials, support structures, and different operational strategies, including venting pressure and filling levels, affect the frequency of relief valve activations. Finally, in Section 3.3, the calculations related to the geometric dimensions of the tanks, the quantities of liquid hydrogen required, and the total thermal resistance of the system will be introduced

3.1 Development and definition of degradation indices for hydrogen aircraft components

In this section, a new methodology for evaluating the effects of various operational conditions and environmental factors will be introduced and detailed. Specifically, in Subsection 3.1.1, the metrics, indicators, and degradation indices that will be used for the execution

of case studies in Chapter 4 will be presented, with the aim of demonstrating the interconnections between model inputs and outputs. In Subsection 3.1.2, illustrative examples of calculations will be introduced.

3.1.1 Degradation index calculation

The following Table 3.1 summarizes the components under consideration, along with the respective operating and environmental conditions. Additional components, as well as operating conditions and environmental factors (air pressure, dust, presence of sulphates in the air, etc.) may be added.

Table 3.1 Operating conditions, environmental factors, and components.

Operating Conditions	Environmental Factors	Components
Turnaround time	Humidity	Fuel cell
Temperature cycling	Temperature of the surroundings	Liquid hydrogen tank
Pressure cycling		Hydrogen gas tank
Vibrations		Relief valves

The proposed methodology incorporates three primary parameters: the metric m, the indicator S, and the degradation index I, the failure rate λ, alongside a secondary parameter intended to represent the average degradation throughout the entire system, defined as the Average Total Degradation Index ($ATDI$).

Development of Metrics m

The development of metrics, denoted as m, is identified as a critical element in this study, aiming to quantify the impact of diverse operating conditions and environmental factors on aircraft components. Assigning these metrics facilitates a detailed evaluation of how specific conditions affect the lifespan of individual components. It is crucial to acknowledge that the decision to use a spectrum of values for m rather than a singular value arises from the understanding that different operating conditions and environmental factors impose varying degrees of impact on component durability. The establishment of these metrics follows a scale ranging from negligible impact to extremely negative.

In terms of determining the m value, it will be assigned based on the impact of the i-th condition or factor on the number of fatigue cycles or operating hours of the component taken as reference. Where there is existing literature, the quantitative value of m will be defined; conversely, in the absence of data, a qualitative value m^* will be assigned. For the latter scenario, scenario simulations will be represented qualitatively, with the expectation that new laboratory tests will be conducted to allow for the subsequent calculation of a quantitative m value. In the absence of data related to the reduction of service life in terms of operating hours or fatigue cycles, the metric m^* will be calculated in cases where there is data on component degradation. In the case that this data is not available, the metric m^* will not be calculated, thus the degradation will be analyzed theoretically. Regarding

the impact on the number of cycles or operating hours, two extreme reference conditions will be considered. The first considers the number of fatigue cycles or life hours under optimal operating conditions or environmental factors (thus, the best scenario in which $S = 1$). On the other hand, the reference will be made to the number of fatigue cycles or life hours under the most severe operational or environmental condition (thus, the worst scenario in which $S = 5$), representing the state that most significantly affects component durability. By comparing these extremes, the percentage decrease in the number of cycles or operating hours will be calculated, using the following formulas:

$$m = \frac{\text{Number of cycles}(S = 5) - \text{Number of cycles}(S = 1)}{\text{Number of cycles}(S = 5)} \tag{3.1}$$

$$m = \frac{\text{Operating hours}(S = 5) - \text{Operating hours}(S = 1)}{\text{Operating hours}(S = 5)} \tag{3.2}$$

Consequently, from these equations, the metric m can assume a value ranging from 0 to 1. If the metric m assumes the maximum value of 1, this signifies that under the worst-case scenario, the specific operating condition or environmental factors cause the imminent failure of the component. Thus, the metric m represents how critical is the operating condition or environmental factor considered.

This methodology facilitates a more thorough comprehension of the dynamic nature of degradation patterns, recognizing that some conditions may exert a more significant effect on the component's lifespan than others. The adoption of multiple values for m allows for a nuanced assessment, in harmony with the complex interaction between various operating conditions and environmental factors and their distinct influences on the structural integrity and performance of aircraft components.

Definition of Indicators S

The S indicators represent the intrinsic state of any operating conditions or environmental factors, ranging from mild to extreme:

Table 3.2 Overview of the S indicator.

Indicator S_i	**Degradation**	**Reduction in service life %**
1	Mild	$m \times 1 \times \frac{2}{10}$
2	Moderate	$m \times 2 \times \frac{2}{10}$
3	Severe	$m \times 3 \times \frac{2}{10}$
4	Critical	$m \times 4 \times \frac{2}{10}$
5	Extreme	$m \times 5 \times \frac{2}{10}$

The S indicator represents the severity of operating conditions and environmental factors. Higher values of S indicate more severe conditions. For instance, S = 1 could indicate the presence of low vibration levels , whereas S = 5 may denote the system being subjected to high levels of vibrations or extreme temperature surroundings.

The decision to scale S from 0 to 5 embodies a deliberate modeling choice to underscore the indicator's sensitivity to condition severity. As S increases, the anticipated degradation of the component escalates, leading to an increase in the failure rate and a reduction in MTTF. This strategic calibration is crucial in developing a comprehensive metric capable of accurately reflecting the nuances of degradation within the context of hydrogen-powered aircraft systems.

The evolution of the indicator S is calculated based on the outcome obtained from evaluating m under the worst condition (S= 5). For example, if calculations for S = 5 yield an m = 0.6, consequently, I = m×S = 3. Considering Tab. 3.3, this corresponds to a 60% reduction in the component's service life under the most severe operational or environmental condition (S = 5). To model S, the proportionality index p will be used:

$$p = I \times \frac{0.2}{5} \tag{3.3}$$

The proportionality factor p is defined in this way because S is divided into 5 intervals rather than 10 (otherwise, it would have been $p = I \times \frac{0.1}{10}$), and the *scale of degradation* (Tab. 3.3) ranges from 0 to 5, where I = 5 represents a 100% reduction in the component's service life, thus creating a 10:5 ratio. If $I = 3$, $p = 3 \times \frac{0.2}{5} = 0.12 = 12\%$. Hence, from $S = 1$ to $S = 5$, the service life of the component is gradually reduced by 12%, culminating in a 60% reduction at $S = 5$. Further calculation examples will be illustrated in Subsection 3.1.2.

Degradation Index Calculation I

The degradation index I for each component is based on the product of the metric m and the indicator S:

$$I = m \times S \tag{3.4}$$

As the indicator S varies, the degradation status of the reference component will either improve or deteriorate. Therefore, thanks to the S-indicator, although the proposed formula is linear, it encompasses exponential, parabolic or any type of degradation. Upon calculating the index for the considered component, it becomes crucial to evaluate these indices, which effectively represent the component's degradation rate. For the correct interpretation of these indices, specific ranges have been delineated in Table 3.3.

Average Total Degradation Index (ATDI)

$$ATDI = \frac{(I_{\text{Liquid Hydrogen Tank}} + I_{\text{Gaseous Hydrogen Tank}} + I_{\text{Valves}} + I_{\text{Fuel Cells}} + \ldots)}{n} \tag{3.5}$$

This index encapsulates the degradation of the considered system of components. It can be applied only to environmental conditions and vibrations, as each component has its own operational conditions. This index will be useful to evaluate how the total system degradation varies with changes in environmental factors, in light of different operational scenarios and the different allocation of components within the aircraft (with and without air conditioning and pressurization systems), in order to determine the optimal value of various environmental conditions. For example, by varying the external temperature

Table 3.3 Scale of degradation index interpretation.

Degradation index ranges I	Interpretation
$[0, 1]$	Mild Degradation Level: Decrease in the number of fatigue cycles or operating hours from 0 to 20%.
$(1, 2]$	Moderate Degradation Level: Decrease in the number of fatigue cycles or operating hours from 20 to 40%.
$(2, 3]$	Severe Degradation Level: Decrease in the number of fatigue cycles or operating hours from 40 to 60%.
$(3, 4]$	Critical Negative Degradation Level: Decrease in the number of fatigue cycles or operating hours from 60 to 80%.
$(4, 5]$	Extremely Negative Degradation Level: Decrease in the number of fatigue cycles or operating hours from 80 to 100%.

from -20°C to 50°C, the temperature range in which the least degradation of the system is expected will be identified.

Failure rates

Once the index I has been calculated, to compute the new failure rate, the following formula is proposed:

$$\lambda_{\text{new}} = \frac{\lambda_{\text{old}}}{(1 \pm f(x))} \tag{3.6}$$

The plus or minus sign is due to the fact that failure rates are typically calculated under normal operational and environmental conditions, hence average conditions. Therefore, if we consider worse operational and environmental scenarios, we must subtract; conversely, if we consider better scenarios, we simply need to add. However, the formula presented takes into account only one operational or environmental condition. To consider all conditions, the failure rate must be scaled using the following formula:

$$\lambda_{\text{new, total}} = \frac{\lambda_{\text{old}}}{(1 \pm f(x)) \times (1 \pm f(x)) \times (1 \pm f(x)) \ldots} = \frac{\lambda_{\text{old}}}{\sum_{i=1}^{n} (1 \pm f_i(x))} \tag{3.7}$$

where n represents the set of operational conditions and environmental factors.

In this way, it will be possible to evaluate the impact of all the conditions studied in this investigation and to assess different operational scenarios and design solutions. In this context, it is necessary to introduce the percentage reduction in service life $f(x)$ as follows:

$$f(x) = \frac{2 \times I}{10} \tag{3.8}$$

The introduction of this coefficient is necessary because the degradation index I can assume a maximum value of 5, corresponding to a 100% reduction in the component's service life. In this case, the failure rate calculated through Equation 3.6 reach an asymptotic state (goes to infinity), since the condition where the component instantly breaks would be met. For a 100% percentage reduction in service life, the coefficient $f(x)$ should assume

the value of 1, which would lead to zero in the denominator of equation 3.6. Thus, to correlate the degradation index to the percentage reduction in terms of service life, the mathematical formula for $f(x)$ has been constructed accordingly. The conceptual map summarizing the aim of this methodology is presented in Fig. 3.1.

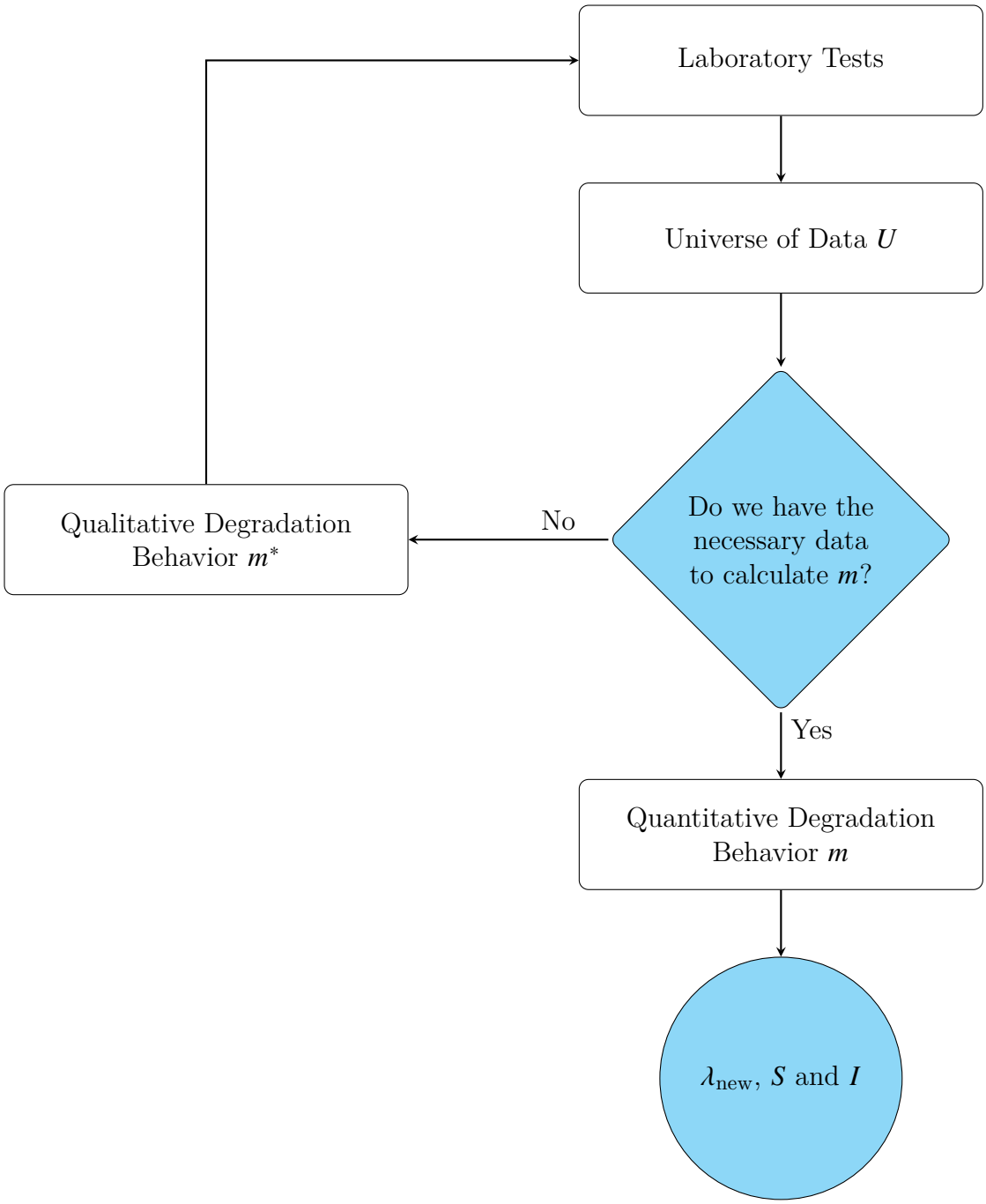

Figure 3.1 Concept map for calculating failure rates.

3.1.2 Calculation methodology

The introduced methodology must be applied by following the steps listed in Fig. 3.2.

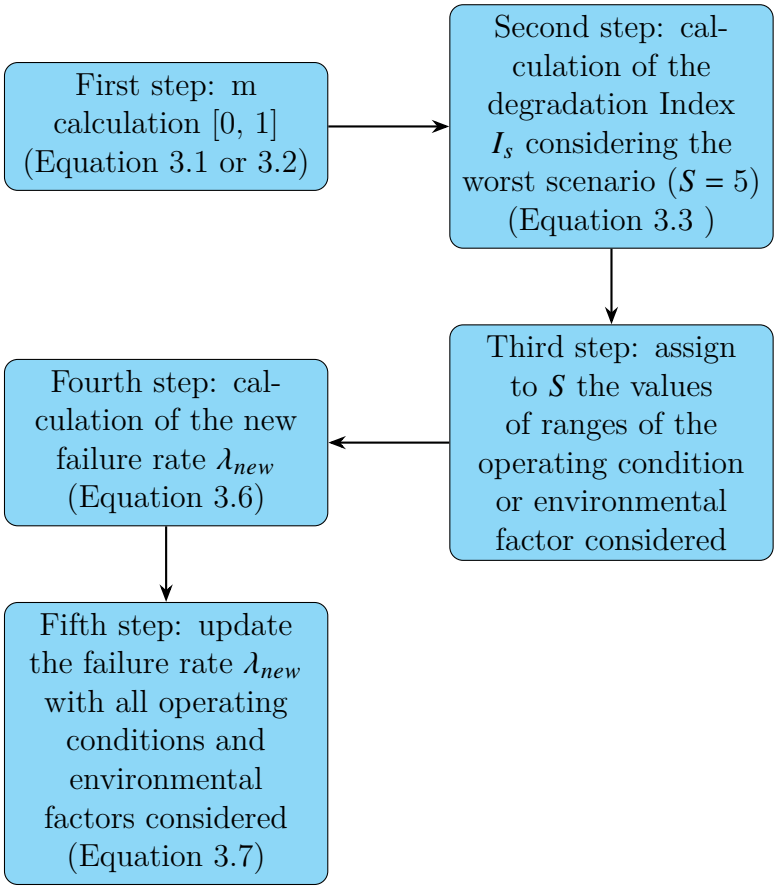

Figure 3.2 Conceptual map of the methodology steps.

First step: m calculation

In this first step, either Equation 3.1 or 3.2 is used. For instance, as will be demonstrated in Chapter 4, in terms of Type III tanks, an external temperature of -40°C yields a metric m of:

$$m = \frac{\text{Number of cycles}(S = 5) - \text{Number of cycles}(S = 1)}{\text{Number of cycles}(S = 5)} = \frac{30,000 - 12,000}{30,000} = 0.6$$

Referring to the different values that the external temperature can assume, if we have a database with different values of the number of fatigue cycles or operating hours that the component can withstand, two values are required: the highest (best-case scenario) and the lowest (worst-case scenario), with their respective reference temperatures.

Second step: calculation of the degradation Index considering the worst scenario

I is calculated in the worst-case scenario. Thanks to its more critical value, the S indicator will be modeled from the best to the worst scenario. With a metric m = 0.6, a maximum degradation index of $I = m \times S = 0.6 \times 5 = 3$ would be obtained, indicating an 60% reduction in the component's lifespan under the most severe conditions, as shown in Tab. 3.3.

Third step: assign to S indicator the values of ranges of the operating condition or environmental factor considered

Defining this indicator for various environmental factors and operating conditions could serve as a starting point for developing a decision-making tool in the design and maintenance of hydrogen-powered aircraft. The inherent flexibility of the S indicator allows for a nuanced portrayal of the dynamic relationship between a component's degradation and diverse operating and environmental situations. Notably, within the spectrum of $S = 0$ to $S = 5$, the degradation of the component is expected to escalate, signifying an increased failure rate (or a decreased MTBF).

The most severe intrinsic state of an operating condition or environmental factor, corresponding to an S Indicator of 5, should reflect the largest impact on reducing the component's lifespan. For instance, if regulations and standards stipulate that Type IV tanks must be tested up to an ambient temperature of 85°C, then this temperature would certainly fall within the range corresponding to S=5. However, for Type III tanks subjected to autofrattage, at elevated ambient temperatures, the lifespan of Type III tanks increases, while at low sub-zero temperatures, it significantly decreases (as showed in Subsection 2.2.6). Therefore, for the latter $S = 5$ would correspond the lowest temperature from the tests conducted in the laboratory (according to the temperature ranges agreed upon by the ISO standards and the extreme climatic conditions to which the tanks could be subjected).

For the cited example, the values that incorporate the S indicator are illustrated in Tab. 4.3. In this context, the proportionality factor p introduced in Equation 3.3 needs to be calculated in order to model the degradation index I (and thus model the degradation) through the indicator S. With a maximum degradation index of $I = 3$, the proportionality factor p is equal to $p = 0.12$. This means that within $S = 1$, ranges of external temperature must be incorporated such that the component's lifespan decreases up to 12%. Subsequently, within $S = 2$, external temperature values must be incorporated that cause a reduction in the component's lifespan from 12% to 24%. This calculation procedure should be extended up to the maximum indicator ($S = 5$), which, for this example, encompasses external temperature values that cause a reduction in the component's lifespan from 48% to 60%. This procedure must be applied to all operating conditions and environmental factors, considering their respective degradation indices and proportionality factors.

Fourth step: calculation of the new failure rate λ

As a fourth step, the degradation index needs to be calculated. Once the indicator S has been generalized, the degradation index I must be calculated based on the intrinsic

state of the operational condition or environmental factor considered. Thus, if we have an average ambient temperature of 30°C, looking in Tab. 4.3, this temperature corresponds to an indicator of $S = 2$, and a degradation index of $I = 1.2$. Consequently, the coefficient of $f(x)$ must be calculated through Equation 3.8, and finally, the new value of λ can be derived through Equation 3.6.

Fifth step: update the failure rate λ with all the operating conditions and environmental factors considered

As the final step, Equation 3.7 should be applied, in which the initial failure rate is updated with the various operating conditions and environmental factors, and modeled according to the intrinsic state of the condition or factor considered.

3.2 Hydrogen evaporation dynamics: modeling and computational analysis

The current understanding lacks clarity on how hydrogen evaporation may impact the degradation of relief valves and cryogenic tanks over time. Critical factors such as the rate of evaporation, ambient air temperature, thermal insulation conductivity, and tank geometry significantly affect the MTTF or the MTBF of such components in cryogenic applications. To address this gap, constructing a thermodynamic model is essential. This model will enable the computation of key thermodynamic parameters.

This will be achieved through the utilization of Matlab, which will simulate the dynamics of hydrogen evaporation through computational analysis. Firstly, in Subsection 3.2.1, a thermodynamic model will be presented to calculate the evaporation of hydrogen over time. Secondly, in Subsection 3.2.2, a thermodynamic model will be introduced to calculate the pressure increase inside the cryogenic tank, which will allow for the evaluation of the number of valve opening and closing cycles, enabling a comprehensive assessment of the expected failure rates of relief valves. Furthermore, in Subsection 3.2.3, a calculation methodology will be proposed to determine the MTTF and failure rate once the number of times the relief valve is activated (as shown in Subsection 3.2.2), is obtained. Finally, in Subsection 3.2.4, a model will be presented to indirectly assess how the degradation of a particular insulation influences the degradation of relief valves and cryogenic tanks.

3.2.1 Thermodynamic model

To assess the LH2 boil-off, a thermodynamic model needs to be developed. The initial step involves modeling the heat entering the tank, analyzing it as a one-dimensional heat flow from the surroundings to the liquid hydrogen. This model was inspired by the work of [24], which highlighted that initially, the outside surface temperature of the tank (Ts) needs to be determined. This wall temperature is based on the heat flow into the insulation from convection and radiation, and heat flow to the liquid hydrogen by conduction through the insulation. The heat transfer mechanisms are illustrated in Fig. 3.3.

Fig. 3.3a shows the one-dimensional model of heat transfer, while Fig. 3.3b displays the thermal balance at the outer wall of the tank. Since the temperature of the hydrogen is significantly lower than that of the ambient temperature, all the heat transfer contributions in this model are directed inward. The incoming heat (Q_{in}) is described by the sum of convection and radiation components:

$$Q_{in} = Q_{convection} + Q_{radiation} = Ah(T_\infty - T_s) + \varepsilon\sigma A(T_\infty^4 - T_s^4) \tag{3.9}$$

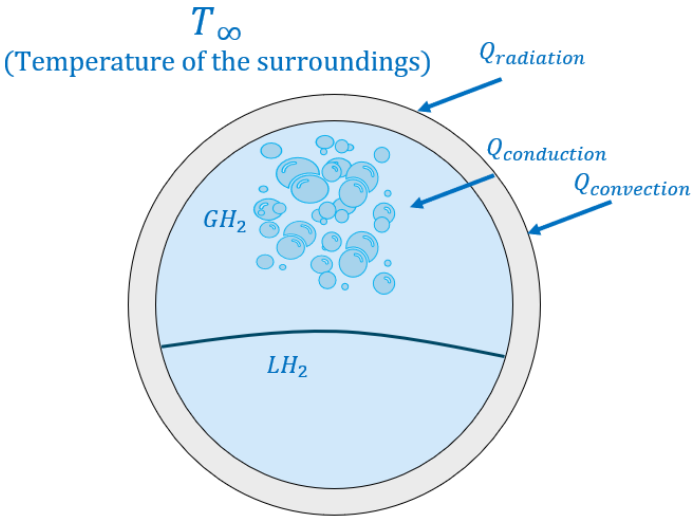

(a) One dimensional heat transfer for liquid hydrogen tank

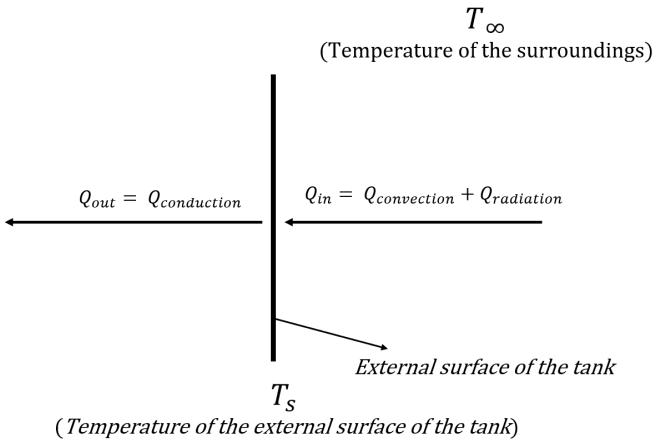

(b) Thermal equilibrium at the wall

Figure 3.3 Thermodynamic balance overview.

The outgoing heat (Q_{out}) is defined by the conduction through the insulation:

$$Q_{out} = Q_{conduction} = \frac{(T_s - T_{LH2})}{R} \tag{3.10}$$

Where:

- T_∞ denotes the ambient temperature surrounding the tank;
- T_s represents the temperature of the outer tank wall, which is the surface temperature of the tank exposed to the environment;
- T_{LH2} is the temperature of the liquid hydrogen within the tank, indicating the internal content's temperature;
- ε is the emissivity of the insulation surface/outer tank wall (a typical emissivity value of 0.045 is assumed by [88]);

- σ is the Stefan-Boltzmann constant $5.67 \times 10^{-8} \frac{W}{m^2 K^4}$;
- h is the convection coefficient for the air surrounding the tank;
- R is the total thermal resistance
- A is the heat exchange surface area.

The tank is considered to be in an isolated environment with no active air movement, hence the convection coefficient is based on natural convection of the air surrounding the tank. This coefficient can be represented by:

$$h = \frac{N_{\mathrm{UD}} \cdot K_{\mathrm{g}}}{D} \tag{3.11}$$

Where the thermal conductivity of the air (K_{g}) depends on the fluid properties at a given temperature and pressure, D is the equivalent diameter and N_{UD} is the Nusselt number. In the context of heat transfer analysis for tanks, it is essential to evaluate the convective heat transfer coefficient h, which is encapsulated by N_{UD}. The calculation of N_{UD} varies depending on the geometry of the tank, with distinct formulas for spherical and cylindrical shapes.

The Nusselt number for a spherical tank is given by:

$$N_{\mathrm{UD}} = 2 + 0.589 R_{\mathrm{AD}}^{1/4} \left[1 + \left(\frac{0.469}{P_r} \right)^{9/16} \right]^{4/9} \tag{3.12}$$

While for a cylinder:

$$N_{\mathrm{UD}} = \left[0.60 + 0.387 R_{\mathrm{AD}}^{\frac{1}{6}} \Big/ \left(1 + (0.559/P_r)^{\frac{9}{16}} \right)^{\frac{8}{27}} \right]^2 \tag{3.13}$$

Here, R_{AD} represents the Rayleigh number, which is influenced by the temperature difference between the fluid inside the tank and the surrounding environment, the gravitational force, and the properties of the fluid such as viscosity and thermal diffusivity. The Rayleigh number R_{AD} is defined by the equation:

$$R_{\mathrm{AD}} = \frac{g\gamma(T_\infty - T_s)D^3}{\nu\alpha} \tag{3.14}$$

where g denotes the gravitational acceleration, γ is the volumetric thermal expansion coefficient (which is $1/T_\infty$ for a gas such as air), ν is the kinematic viscosity, and α is the thermal diffusivity.

The Prandtl number (P_r) is a dimensionless number, which is defined in terms of the properties of the fluid, specifically air in this context. The Prandtl number is given by the formula:

$$Pr = \frac{\mu_{\mathrm{air}} \cdot c_p}{k_{\mathrm{air}}} \tag{3.15}$$

where μ_{air} is the dynamic viscosity of the air, c_p is the specific heat capacity at constant pressure, and k_{air} is the thermal conductivity of air.

In the analysis of air as the working fluid, the properties such as thermal diffusivity (α) and kinematic viscosity (ν) are temperature-dependent:

$$\alpha = -3.119 \times 10^{-6} + 3.541 \times 10^{-8} T_\infty + 1.679 \times 10^{-10} T_\infty^2 \tag{3.16}$$

$$\nu = -2.079 \times 10^{-6} + 2.777 \times 10^{-8} T_\infty + 1.077 \times 10^{-10} T_\infty^2 \tag{3.17}$$

All this information was obtained from Colozza et al. [24], Cuccurullo et al. [25], and Verstraete [130]. Concerning the values of various parameters such as the thermal conductivity of air and air viscosity, specific heat of the air, these values can be easily found in thermodynamic tables. By equating Equation 3.9 with Equation 3.10, an equation with two unknowns is obtained: T_s and h.

$$Q_{in} = Ah(T_\infty - T_s) + \varepsilon\sigma A(T_\infty^4 - T_s^4) = Q_{out} = \frac{(T_s - T_{LH2})}{R} \tag{3.18}$$

To solve this problem, the process is carried out iteratively: an initial value of T_s is assumed, the heat transfer coefficient h is calculated through the previously shown process, and it is substituted into Equation 3.18. Once the value is substituted into the equation, the new temperature T_s is calculated, and the percentage error is determined, which typically should not exceed 5% [25]. However, for this model a percentage error of 1% was used. Therefore, with the initial value of T_s set, the system of equations will continue to calculate h until the percentage error on the temperature T_s is less than 1%.

Once the outer surface temperature of the insulation is known, the heat luck can be calculated:

$$Q_{out} = \frac{(T_{s,new} - T_{LH2})}{R} \tag{3.19}$$

The calculation of boil-off rate (M) in $\frac{kg}{s}$ of the liquid hydrogen is performed through an energy balance between the heat flow through the insulation and the energy required to boil the liquid hydrogen [24]. From [141], the liquid hydrogen evaporation rate is computed by using:

$$M = \frac{Q_{out}}{h_e} \tag{3.20}$$

M represents the mass of hydrogen evaporated per second, Q_{out} is the heat outflow in joules per second ($\frac{J}{s}$) and h_e is the latent heat of vaporization of liquid hydrogen, often expressed in kilojoules per kilogram ($\frac{kJ}{kg}$). The evaporation rate (ER%) for hydrogen within a tank over the duration of one hour is defined by the equation:

$$\text{ER\%} = \frac{m_{ev}}{m_{H2}} \times 100 \tag{3.21}$$

Where:

- m_{H2} is the mass in grams of the amount of liquid hydrogen in the tank.

- $m_{ev} = M \times 3600 \times 1000$ is the mass in grams of hydrogen that has evaporated within one hour.

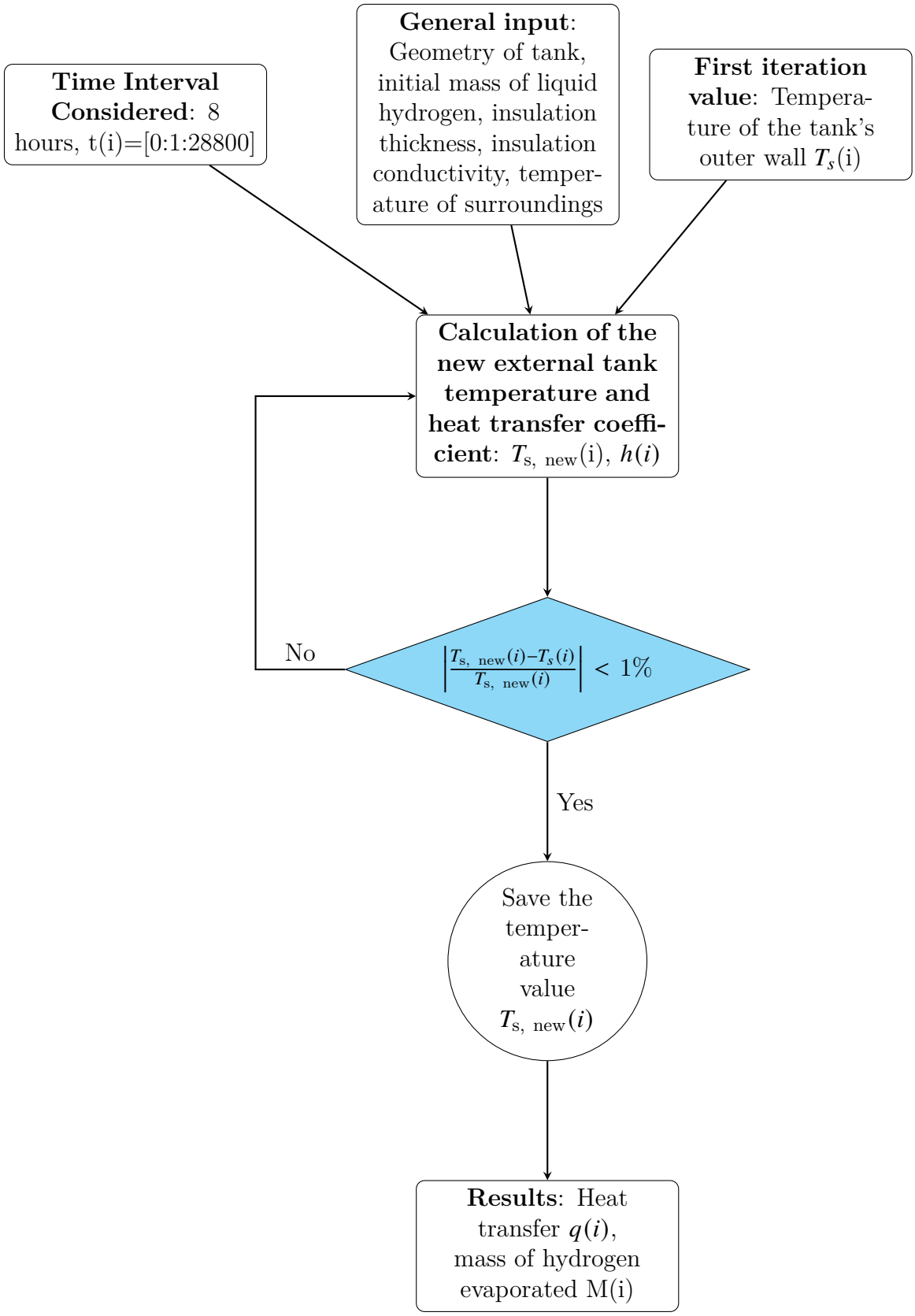

Figure 3.4 Flow chart of the iteration process, calculation of the evaporated hydrogen mass over time and of the heat flux over time.

At present, the acceptable boil-off rate for aircraft is 0.1% or less by weight per hour [141].

However, in the models proposed by the literature, the variation of temperature over the span of an hour is not taken into account (although negligible considering the use of high-performance insulation). Instead, given an external temperature, the heat flow and consequently the evaporation rate are calculated. To consider a more precise model and take into account the evolution of the external temperature from a period of 8 to 13 hours (the typical overnight downtime of an aircraft at an airport), the previously presented model has been improved through the use of the software Matlab. Here, the iteration process to find the values of h and Ts and the calculations to compute the outgoing heat flow Q_{out} and the evaporated hydrogen mass M, are updated and calculated every second. Thus, taking an 13-hour interval, Matlab returns 46,800 values for each aforementioned parameter. In this case, the total evaporation in one hour will be obtained by summing the first 3,600 values from the array of M, since the value of each parameter is updated second by second. The overview of this methodology is summarized in Fig. 3.4.

3.2.2 Analysis of pressure control in cryogenic storage systems

Lin et al. [75] propose a model to calculate the increase of pressure and pressure fluctuations in a homogeneous cryogenic storage tank. This model is derived by applying the first law of thermodynamics and the law of conservation of mass to a control volume that encompasses the tank's liquid and vapor contents, which are assumed to be in a homogeneous state. The control volume does not include internal tank hardware, and the control surface aligns with the inside surface of the tank wall. For self-pressurization of a closed, constant-volume cryogenic tank experiencing only heat leak, with no work done on the fluid by pumping and no mass flow into or out of the tank, the rate of pressure change is expressed as follows:

$$\left(\frac{dP}{dt}\right)_{\text{hsp}} = \frac{\phi Q_w}{V} \tag{3.22}$$

where $\frac{dP}{dt}$ represents the pressure rise rate over time, ϕ is the energy derivative, Q_w is the heat transfer per unit time (is the Q_{out} calculated in Equation 3.19 per unit time), and V is the tank fluid (liquid and vapor) volume, not including volume occupied by internal tank hardware.

The energy derivative ϕ can be expressed in terms of average density ρ or specific volume v as follows:

$$\phi = \frac{1}{\left(\frac{\partial u}{\partial P}\right)_{\rho}} = v\left(\frac{\partial u}{\partial P}\right)_{v} \tag{3.23}$$

The tank fill level β, fluid quality x, and density or specific volume ratio are related as follows:

$$(1-x)/x = (\rho_f/\rho_g)[\beta/(1-\beta)] \tag{3.24}$$

where β = percent fill/100, ρ_f is the density of the liquid hydrogen and ρ_g is the density of the gaseous hydrogen. Rearranging gives an expression for x:

$$x = \left[1 + (\rho_f/\rho_g)[\beta/(1-\beta)]\right]^{-1} \tag{3.25}$$

The quality is used to calculate the average tank fluid (liquid and vapor) density ρ:

$$\rho = \left[x/\rho_g + (1-x)/\rho_f\right]^{-1} \tag{3.26}$$

Once the average tank fluid density is calculated, knowing the initial pressure in the tank, it will be possible to calculate the value of ϕ through the following thermodynamic diagrams shown in Fig. 3.5:

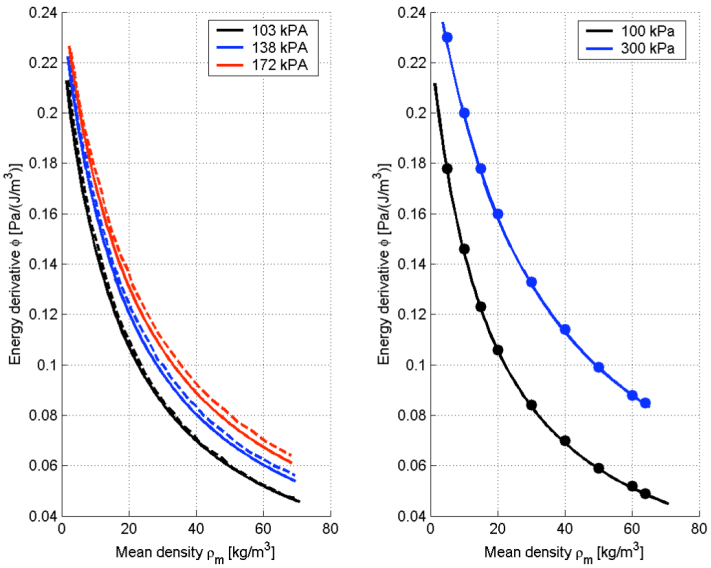

Figure 3.5 The energy derivative in function of pressure and density [128].

Since ρ, and therefore ϕ, are mass-averaged properties for the total tank fluid mass, their values vary with the tank fill fraction. Fig. 3.5 illustrates the parameter ϕ as a function of average fluid density and tank pressure for hydrogen at saturated, two-phase conditions. It is observed that ϕ decreases with increasing average fluid density ρ and increases with increasing tank pressure P. Consequently, the pressure rise rate increases linearly with the tank volumetric heating rate $\frac{Q_w}{V}$ and the parameter ϕ . These correlations are very important, as they will allow in Chapter 4 to demonstrate that the lower the fill level, the higher the pressure increase inside the tank, thereby increasing the workload of the relief valves.

Usually, the homogeneous model, which assumes a uniform temperature in the tank, will yield the lowest pressure rise rate for a tank. Ground tests with cryogenic hydrogen have shown that the actual pressure rise rate spans a range from approximately 1 to more than 10 times faster than the homogeneous model prediction for well-insulated tanks [75]. The lesser degree of thermal stratification in low heat flux conditions results in a pressure rise rate that is closer to the homogeneous prediction [41], which is why the solutions proposed in Subfig. 2.13b, Subfig. 2.13c and Subfig. 2.13d are advantageous from this perspective. Lin et al. [75] and Verstraete [130] adopt a pressure rise rate of 2 times the homogeneous model's prediction. However, for the following study, the following equation is proposed:

$$\left(\frac{dP}{dt}\right)_{\text{hsp}} = \frac{2FS\phi Q_w}{V} \tag{3.27}$$

where FS is the safety factor due to the influence of humidity and vibration load. FS is therefore the sum of $FS_{humidity} + FS_{vibrations}$, based on the data presented in Subsections 2.3.5 and 2.3.6. In particular, a safety factor of 1.1 will be considered when the air humidity exceeds 70% and the ambient temperature is higher than T=30°C, assuming that Equation 3.27 has been verified under normal environmental conditions. Regarding vibrations, this study considers the operational scenario when the airplane is stationary at

the airport, so $FS_{vibrations}$ will be considered equal to zero. However, the safety factor must be considered (and calculated) in case different operational scenarios were assumed.

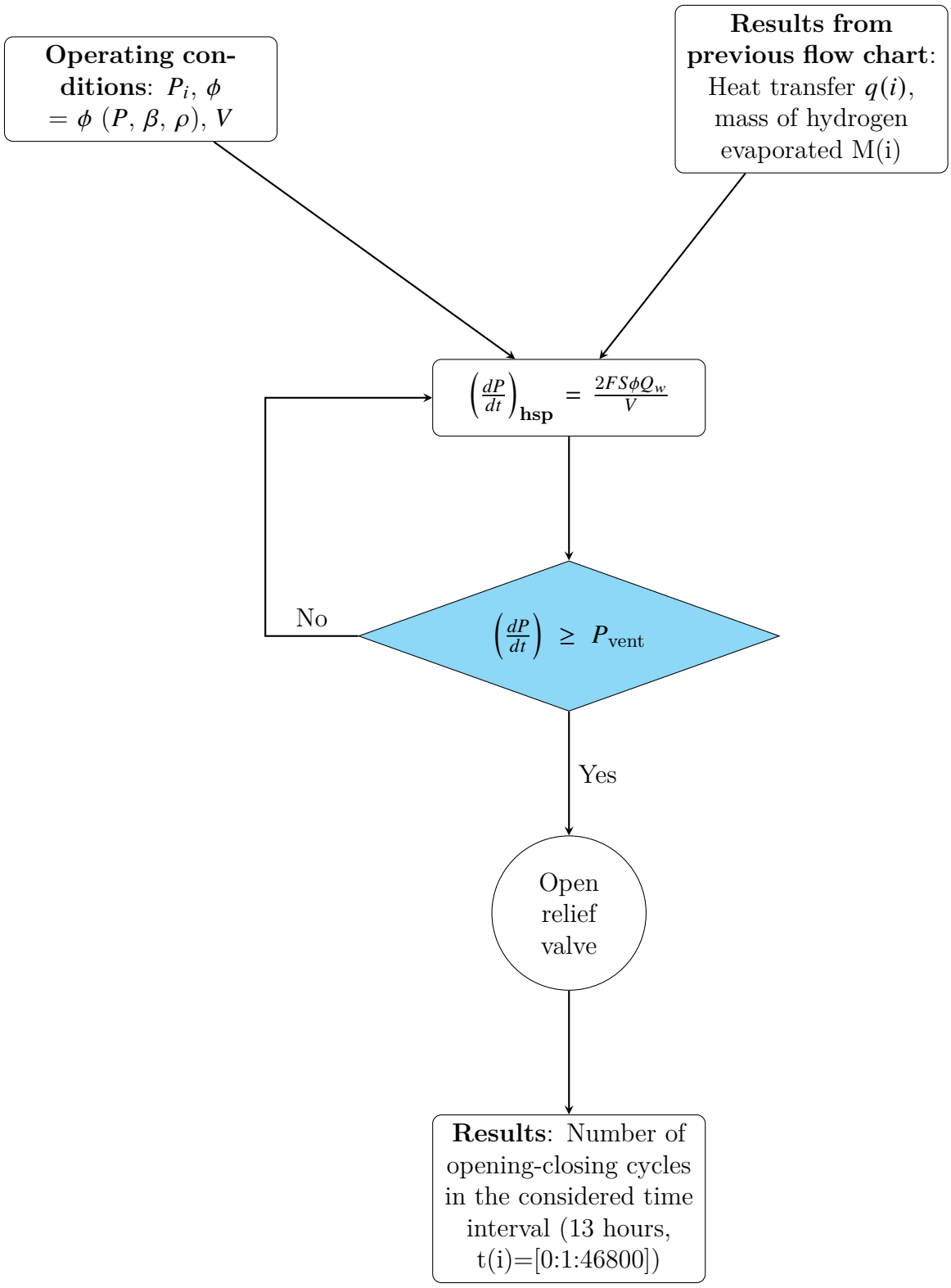

Figure 3.6 Flow chart of the if loop of the internal tank pressure control.

The main aim of this computational analysis is to determine the number of times the relief valve triggers to reduce the pressure inside the tank. For this purpose, the equations presented in Subsection 3.2.3, particularly formula 3.27, have been implemented in Matlab and integrated into the code developed according to the guidelines of Subsection 3.2.2. The logic of the model works as follows: starting from a previously developed model that calculates, second by second, the amount of heat entering the tank, Equation 3.19 is substituted into Equation 3.27. This allows for the calculation of the internal pressure increase at every moment, for the desired time interval.

Consequently, to establish the number of relief valve interventions, an if loop has been implemented. In this loop, a threshold pressure value (P_{vent}) is defined; whenever the internal pressure reaches this value, the model simulates the opening of the valve, assuming that this brings the tank's pressure back to the initial value P_i. The code calculates not only the trend of pressure over time - results that will be presented in Chapter 4 - but also provides the number of activations of the relief valve. Thanks to this methodology, it will be possible to evaluate how different design variables, such as the geometry of the tank, types of insulating materials, support structures, as well as different operational strategies such as ventilation pressure and fill level, influence the frequency of relief valve activations. The summary flow chart of this model is presented in Fig. 3.6.

3.2.3 Direct analysis: from the number of valve opening-closing cycles to the failure rate

Ensuring the correct function of relief valves is vital. For this reason, the DIN EN ISO 21011 standard [53] stipulates that Category A cryogenic service valves, those intended to be operated with normal frequency, must withstand at least 2,000 operational cycles. Considering the scarcity of data in the literature regarding cryogenic relief valves capable of sustaining such a number of cycles, this study assumes the use of a valve suitable for these conditions. This hypothesis takes into account various negative factors such as vibrations, temperature and pressure cycles, the effect of ice formation on valve degradation, and the effect of hydrogen embrittlement.

The direct analysis proposed here begins with the initial number of optimal operational cycles of the valve. Subsequently, through the number of opening and closing cycles calculated using the methodology introduced in the previous subsections, the expected MTTF for the valve is estimated.

The initial step towards calculating the failure rate involves determining the expected number of years (ENY) the valve operates correctly.

$$ENY = \frac{N_{SL}[\text{cycles}]}{N_{CD}[\text{cycles/day}] * 365[\text{days/year}]} \tag{3.28}$$

ENY is contingent upon the frequency of relief valve activations, essentially depending

on N_{CD}. N_{CD} refers to number of actual operating cycles per day, calculated using the methodology outlined in Subsection 3.2.2. N_{SL} is the number of cycles the valve can withstand in its service life (in this a value of 2,000 cycles is assumed). Following the calculation of ENY, MTTF is computed accordingly. Subsequently, the failure rate can be determined through the inverse formula ($\lambda = \frac{1}{MTBF}$).

$$MTBF = ENY[\text{years}] * 365[\text{days/year}] * OHD[\text{h/day}] \tag{3.29}$$

- OHD = operating hours per day

Given that N_{CD} is influenced by various factors such as the cryogenic tank's insulation, materials, external temperature, venting pressure, filling level, and other parameters, the failure rate for relief valves is not constant. Instead, it will vary according to the operational conditions of the tank, materials, insulation, and environmental factors.

In Chapter 4, it will be demonstrated that the failure rate of relief valves is strongly dependent on the venting pressure. Furthermore, the opposite trend, due to the increase in venting pressure, between the failure rate of cryogenic tanks and relief valves will be argued and illustrated. Concerning relief valves, the goal will be to obtain the trend illustrated in Fig. 3.7, where the variation of the curve will be analyzed considering different insulation and different filling levels. Additionally, different operational scenarios will be analyzed by changing and alternating parameters on the x-axis, where the dependency of failure on filling level, thermal resistance due to insulation, materials, and tank geometry, and from hydrogen evaporation, will be expressed. All this, considering different environmental conditions. Nevertheless, the developed methodology is highly versatile, as it can be applied to all components of the system involved in counteracting the increase in pressure inside the tank.

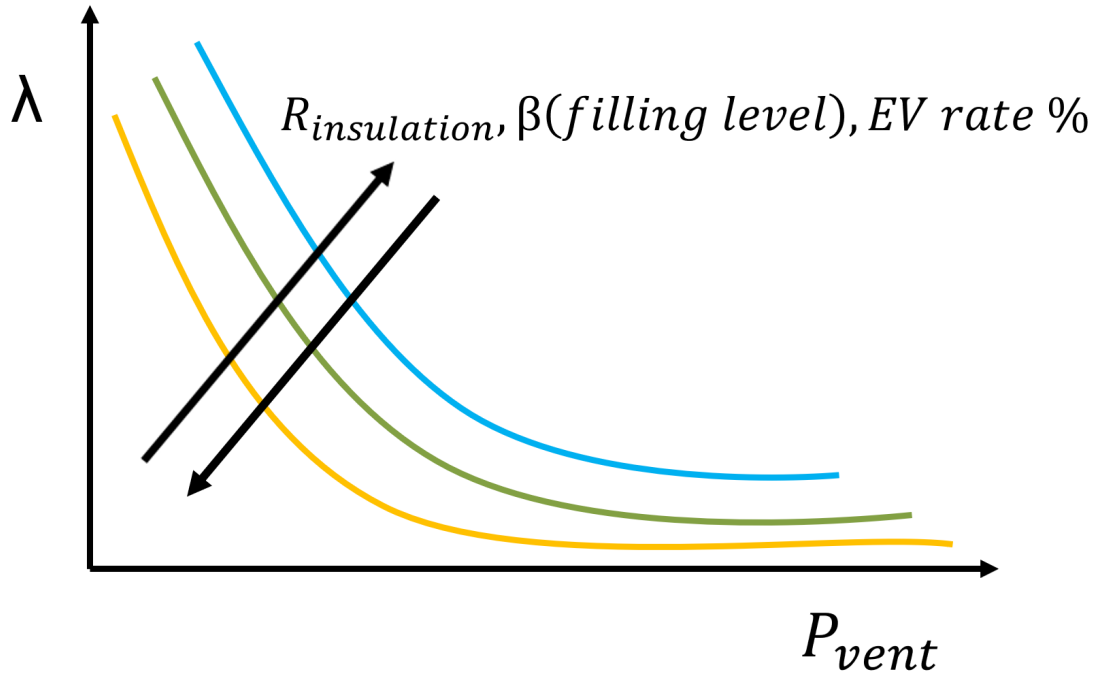

Figure 3.7 Relief valve failure rate theoretical trend.

Regarding the venting pressure, all possible cases will be examined. However, according to [133], the rate of LH2 evaporation loss in one day decreases from 0.17% to 0.14% as the control range increases from 6.9 kPa to 20.4 kPa. Therefore, if the tank's higher weight load and pressure proof are permissible, a larger control range is preferred. Typically, the venting pressure equals the operating pressure, but from this preliminary analysis, the venting pressure should be reduced as much as possible to lead to a minimum tank weight [138]. In addition, to minimize the boil-off of LH2, the pressure at which the tank is filled needs to be significantly lower than the venting pressure in the tank [130]. For this study, therefore, operating pressures of liquid hydrogen lower than the tank's designed operational pressure will be used as a reference; it will also be evaluated how a venting pressure higher than the tank's operational pressure impacts the tank's fatigue life. The set pressure tolerances of pressure relief valves shall be ±3% of set pressure or ±0.1 bar (0.01 MPa), whichever is greater [54]. In this study, two operating pressures will be examined: 2 bar, which according to [5] is the optimal operating pressure for long-duration high-altitude aircraft; and 3 bar, used by [85], with vent pressures between 1.5 and 3.1 bar for both operating pressures.

To assess the direct effect of the hydrogen evaporation rate on the valve failure rate, equations 3.19, 3.20, 3.21and 3.27 were manipulated. Specifically, to ensure that the hydrogen evaporation rate remains below 0.1%, the following equations are derived:

$$m_{ev} = 0.001 \times m_{H_2} \tag{3.30}$$

$$M = \frac{0.001 \times m_{H_2}}{3.6 \times 10^6} \tag{3.31}$$

Consequently, the maximum permissible heat leak from the system to maintain a 0.1% evaporation rate, denoted as $Q_{out_{max}}$, is given by:

$$Q_{out_{max}} = \frac{10^{-9} \times m_{H_2} \times h_e}{3.6} \tag{3.32}$$

Manipulating Equation 3.32 with Equation 3.27 results in the following formula:

$$\frac{dP}{dt} = \frac{2 \times FS \times \phi \times 10^{-9} \times m_{H_2} \times h}{3.6 \times V} \tag{3.33}$$

This represents the pressure increase due to conditions ensuring a 0.1% evaporation rate.

To determine the pressure increase inside the tank for various evaporation rates, the following formula is introduced:

$$\frac{dP}{dt} = \frac{2 \times FS \times \phi \times (10^{-9} \times m_{H_2} \times h_e)}{3.6 \times V} \times \frac{EV\%}{0.001} = 2 \times FS \times \phi \frac{(10^{-6} \times m_{H_2} \times h_e)}{3.6 \times V} \times EV\% \tag{3.34}$$

Through this formula, it is possible to disengage from design parameters such as material choices and insulations, and by using m_{H_2}, h_e, and V, it is possible to evaluate how different hydrogen evaporation rates affect the pressure increase within the cryogenic tank.

3.2.4 Indirect analysis: incorporating the insulation degradation in the computational analysis

Since the current literature does not present specific studies on the effect of insulation degradation on the operation of relief valves, a new research approach is proposed. It is particularly noted that for some insulating materials, such as MLI, there are no models describing how operational and environmental conditions can influence their degradation. To investigate the impact that insulation degradation may have on the operating cycle of relief valves, an indirect method is suggested. This approach involves estimating the failure rate of the valves for different levels of thermal resistance R. In this context, it is hypothesized that a decrease in thermal resistance R could affect the frequency of opening and closing of relief valves, thereby allowing a better understanding of the interaction between insulation degradation and valve reliability.

To assess the impact of insulation degradation, the computational thermodynamic model previously introduced has been modified. Reference will be made to Equation 3.19; through the developed Matlab code, it's possible to vary the thermal resistance R from a scenario where the insulation is fully degraded (lacking insulation, where the tank materials act as the sole insulating barrier for liquid hydrogen) to the initial design value of the thermal resistance R, which depends on the insulation, tank geometry, and the tank materials themselves. Consequently, employing Equation 3.29 and the computational analysis previously described, the frequency at which the relief valve is activated for each distinct value of R will be calculated, thus evaluating the potential effect of insulation degradation on the relief valves.

3.3 Calculation of the number of liquid hydrogen tanks required and the thermal resistance of the system

To simulate the evaporation of liquid hydrogen, understanding the initial mass of hydrogen and the volume of the tank is crucial. Thus, reference will be made to the Airbus 320 model, which has a maximum fuel capacity of 27,200 litres [7]. Multiplying this quantity by the density of kerosene at 15°C, $\rho_{\text{kerosene}} = 0.808 \frac{kg}{l}$ [92], gives 21,977.6 kg. However, the specific energy of liquid hydrogen is approximately three times greater than that of kerosene [40, 90], hence, the mass of hydrogen liquid required to deliver the same energy is 7,326 kg. This mass, through the density of liquid hydrogen $\rho_{LH2} = 71 \frac{kg}{m^3}$ [24], corresponds to a volume of 103.5 m^3. To calculate the number of spherical or cylindrical tanks required, constraints were set on the maximum radius of the sphere and the cylinder. The constraint

on radius selection is justified by the fact that the cabin of the A320 has a fuselage width of 3.95 m. Considering the TTB configuration (2.1e), multiple cylindrical tanks are used. Therefore, multiple cylindrical tanks with a maximum radius of 1 meter were considered for this study to allow passengers to sit in the cabin. The major constraint on the radius of spherical tanks is due to the fact that they could be placed as in configuration 2.1b. However, as shown in the table 3.4, to ensure the same energy supply, the A320 is not large enough. In fact, with a smaller radius of 1.8 meters, approximately six spheres in total would be needed (excluding insulation and components). The same applies to cylindrical geometry. Considering a radius of 1 meter, with the current geometries, there would not be enough space for the allocation of additional components plus the cabin for passengers. For long-haul flights, the introduction of cylindrical and spherical tanks, to guarantee the same amount of energy, leads to the introduction of new generation aircraft.

A cylindrical tank has a larger surface area with equal capacity, while the pressure inside the cylindrical tank is greater and not equally distributed, requiring a larger and thicker wall. These factors result in the mass of the cylindrical tank being greater than that of the spherical tank [141]. Additionally, a spherical tank is chosen over a cylindrical one because the cylinder has a greater area, increasing the thermal exchange surface which would mean having a greater influence (albeit slight) on the evaporation of liquid hydrogen.

Table 3.4 Geometric characteristics of liquid hydrogen tanks for a total volume of 103.5 m^3.

Cylindrical Tank*		**Spherical Tank****	
Height [m]	Number of Cylinders	Radius [m]	Number of Spheres
3.65	9.00	1.40	9.00
4.10	8.00	1.45	8.00
4.68	7.00	1.52	7.00
5.46	6.00	1.60	6.00
6.55	5.00	1.70	5.00
8.19	4.00	1.83	4.00
10.92	3.00	2.00	3.00
16.39	2.00		

* Radius = 1 [m], ** Radius $\leq$ 2 [m]

Referring to Table 3.4, currently the most probable configurations are: Subfig. 2.1b, where the tanks could be placed in both the front and rear of the aircraft; Subfig. 2.1d, in which the tanks would be positioned above the passenger cabin for the entire length of the aircraft; the configuration in Subfig. 2.1c, where the tanks would be connected in a ring, allowing for weight distribution; and the TTB configuration in Subfig. 2.1e, where the tanks would be connected to the wings through support structures. Table 3.5 summarizes the likely configurations varying with the number of tanks that could be allocated in the

aircraft.

Table 3.5 Number of tanks with respective liquid hydrogen masses and probable placement.

Number of Tanks	Mass of Hydrogen [kg]	Volume [m^3]	Configuration
2.0*	3,663.0	51.8	Fig. 2.1e*
3.0	2,442.0	34.5	Fig. 2.1d*, Fig. 2.1b**
4.0	1,831.5	25.9	Fig. 2.1d*, Fig. 2.1b**
5.0	1,465.2	20.7	Fig. 2.1d*, Fig. 2.1b**
6.0	1,221.0	17.2	Fig. 2.1c, Fig. 2.1d*
7.0	1,046.6	14.8	Fig. 2.1c, Fig. 2.1d*
8.0	915.7	13.0	Fig. 2.1c, Fig. 2.1d*
9.0	814.0	11.5	Fig. 2.1c, Fig. 2.1d*

* Cylindrical Tanks, ** Spherical Tanks

However, due to spatial constraints, cylindrical tanks seem to be more suitable. In this study, both cylindrical and spherical tanks will be considered, assuming different operational scenarios and configurations, with the goal of understanding which configuration might be more advantageous: ergo, what changes from a configuration with spherical tanks (with a limit on the radius) to a configuration with larger cylindrical tanks.

The insulating materials that will be referenced are SOFI, vacuum layer and MLI with a thickness of 0.2 meters. According to [141], heat transfers from external to internal through three parallel paths: by coils, by insulation, and by four point-contact insulating supports.

The thermal resistance of a tank with spherical geometry is defined as [25]:

$$R_{\text{insulation}} = \frac{1}{4\pi k}\left(\frac{1}{r_1} - \frac{1}{r_2}\right) \tag{3.35}$$

While for cylindrical geometry [25]:

$$R_{\text{insulation}} = \frac{\ln\left(\frac{r_2}{r_1}\right)}{2\pi k L} \tag{3.36}$$

Where k is the thermal conductivity of the insulation, r_1 and r_2 are the inner and outer radii of the insulation. The thermal resistance of the coil is defined as [141]:

$$R_{\text{coil}} = \frac{L_{pipe}}{2\pi\lambda_{pipe}A_{pipe}} \tag{3.37}$$

The total thermal resistance is [141]:

$$R = \frac{1}{\frac{4}{R_{\text{structure support}}} + \frac{1}{R_{\text{insulation}}} + \frac{1}{R_{\text{coil}}}} \tag{3.38}$$

For this study the resistance of the coil $R_{\text{coil}} = 4206.6\ \frac{\text{K}}{\text{W}}$ and the resistance of the structure support $R_{\text{structure support}} = 749.3\ \frac{\text{K}}{\text{W}}$ [141].

4 Results

This chapter conducts an extensive investigation into the degradation mechanisms impacting key components of hydrogen-powered aircraft; the approach employed is specifically designed to mirror real-operating conditions. The primary focus of this examination revolves around understanding the nuanced influence of operating conditions and environmental factors on critical elements, including fuel cells, cryogenic tanks, Type III and Type IV tanks, and cryogenic valves. In Section 4.1, degradation indices and the consequent failure rates (where possible) will be calculated, in addition to an analysis of the strategies that may be pursued to mitigate the negative effects of environmental factors and vibrations.

Additionally, in Section 4.2, the results of the computational analysis will be presented, providing further insights into the performance of the components of the TVS under varying conditions. This dual-pronged approach, combining empirical degradation indices with thermodynamic simulation outcomes, contributes to a more robust and holistic understanding of the degradation patterns affecting hydrogen-powered aircraft components.

Finally, in Section 4.3, the most suitable configurations for the allocation of components will be presented, in order to optimize their lifespan.

4.1 Calculation of component degradation indices under varied operating and environmental conditions

In this section, starting from Subsection 4.1.1, the effects of all operating conditions and environmental factors on Type III and Type IV tanks will be examined, along with the corresponding degradation indices and the assignment of the S indicator intervals. Based on these results, in Subsection 4.1.2, the baseline failure rates will be scaled, taking into account all operating conditions and environmental factors. In Subsections 4.1.3 and 4.1.4, analyses of cryogenic tanks and fuel cells will be presented, calculating the degradation indices where possible and highlighting strategies to enhance the lifespan of such components.

4.1.1 Analysis of the effects of operating conditions and environmental factors on type III and IV tanks for hydrogen gas applications

Influence of the filling pressure

Beginning with the analysis of Type III tanks, reference is made to Tab. 2.3, where the most conservative values among those measured in different tested tanks have been selected. Subsequently, in order to calculate the probable number of cycles for various FP percentages different from those listed in the table, a linear interpolation was performed using Matlab software. The trend resulting from this process is depicted in Fig. 4.1.

Utilizing Equation 3.1, the value of m for the specified data range was determined to be:

$$m = \frac{93,883 - 5,122}{93,883} \approx 0.991$$

As a consequence, the maximal degradation index I (at $S = 5$), was computed to be $I = m \times 5 = 4.95$. This leads to the identification of the proportionality factor p, calculated as $p = \frac{0.2 \times I}{5} = 0.198$. Further insights were garnered through Fig. 4.1, where intervals of the FP% were aligned with the S indicator, facilitating the depiction of component life diminishment from 0 to 99%, as demonstrated in Tab. 4.1.

In the analysis pertaining to Type IV tanks, an estimated life-cycle of 94,000 cycles has been determined based on a conservative approach (as delineated in Subsection 2.6.4). Furthermore, an assessment at 125% of the FP, conducted under ambient temperature conditions, has yielded a minimal cycle count of 45,000 (no failure was recorded, Fig. 2.6b).

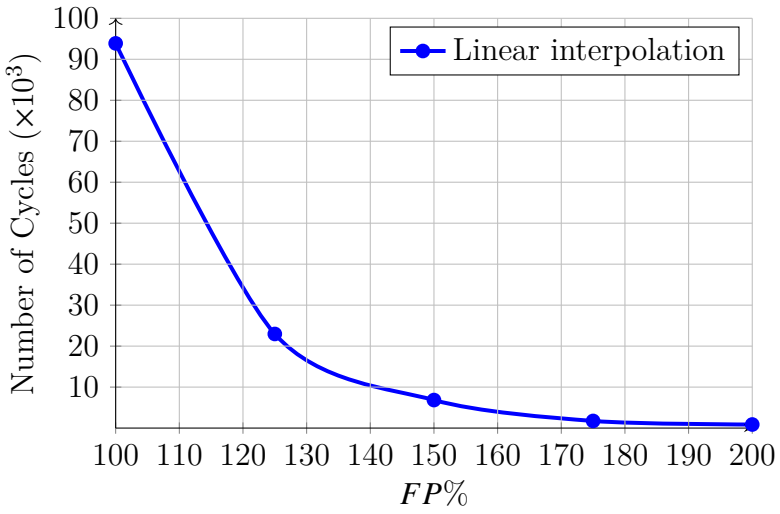

Figure 4.1 Influence of the FP% on fatigue life of Type III tank

Table 4.1 Assignment of FP% intervals to the S indicator for Type III tanks.

FP Range %	**Service Life Reduction $f(x)$%**	**S**	I
100.00 to 106.00	0 to 19.80	$S = 1$ (up to 19.80%)	0.99
106.00 to 113.00	19.80 to 39.60	$S = 2$ (up to 39.60%)	1.98
113.00 to 119.00	39.60 to 59.40	$S = 3$ (up to 59.40%)	2.97
119.00 to 130.00	59.40 to 79.20	$S = 4$ (up to 79.20%)	3.96
130.00 to 200.00	79.20 to 99.00	$S = 5$ (up to 99.00%)	4.95

Thus, for this study this value was used conservatively: it is assumed that after 45,001 cycles there is tank rupture. Additionally, at an increased stress level of 150% of the FP, the cycle threshold has been conservatively adjusted to 30,004, as evidenced by the data presented in Tab. 2.3. The interpolation based on these datasets is methodically illustrated in Fig. 4.2, providing a comprehensive visualization of the life-cycle under varying conditions.

Utilizing Equation 3.1, the value of m for the specified data range was determined to be:

$$m = \frac{94000 - 30004}{94000} \approx 0.68$$

Consequently, the maximum degradation index I in this case would assume a value of $I = m \times 5 \approx 3.40$, with a proportionality factor $p = \frac{0.2 \times I}{5} = m \times 0.2 = 0.136$. Through Fig. 4.2, intervals of the FP% were assigned to the indicator S, guiding the reduction of the component's life from 0 to 68%, as illustrated in Table 4.2.

Hydrogen Environment

Referring to Subsection 2.2.4, it is noted that a Type III Tank exposed to a hydrogen atmosphere could endure 5,122 cycles at 100% of the FP. This observation indicates that the thermal effect attributable to hydrogen heating, along with the probable degradation

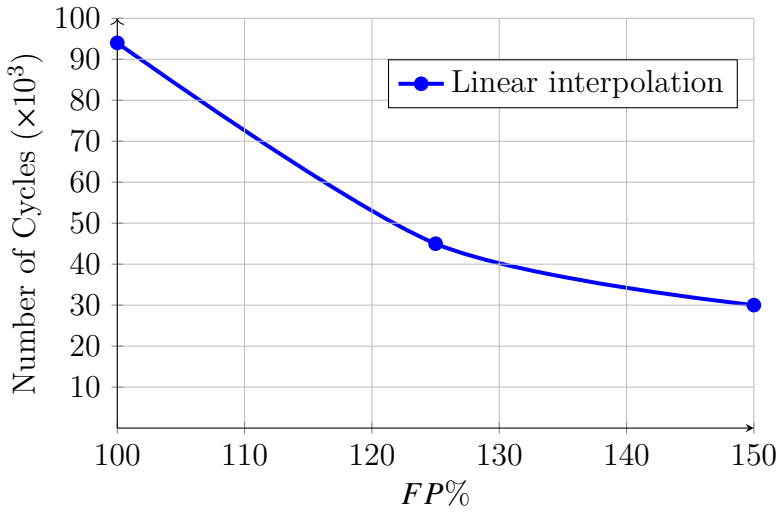

Figure 4.2 Influence of the FP % on fatigue life of Type IV tank

Table 4.2 Assignment of FP% intervals to the S indicator for Type IV tanks.

FP Range %	**Service Life Reduction $f(x)$ %**	**S**	I
100.00 to 108.00	0 to 13.60	$S = 1$ (up to 13.60%)	0.68
108.00 to 112.00	13.60 to 27.20	$S = 2$ (up to 27.20%)	1.36
112.00 to 120.00	27.20 to 40.80	$S = 3$ (up to 40.80%)	2.04
120.00 to 130.00	40.80 to 54.40	$S = 4$ (up to 54.40%)	2.72
130.00 to 150.00	54.50 to 68.00	$S = 5$ (up to 68.00%)	3.40

induced by hydrogen embrittlement, significantly diminishes the service life of the tank. The metric m is calculated as follows:

$$m = \frac{93,883 - 5,122}{93,883} \approx 0.945$$

In this context, reference is made to the number of filling and emptying cycles obtained through a hydraulic test with a 100% FP for Type III tanks, as introduced in Subsection 2.2.3. Within this framework, it is not feasible to model the indicator S. However, the hydrogen environment is observed to cause a reduction in the fatigue cycle number by $f(x) = 94.5\%$, consequently, the degradation index I is calculated as $I = \frac{f(x) \times 10}{2} = 4.725$ (which corresponds to multiplying the found metric m by $S = 5$).

Regarding Type IV tanks, there is an absence of data in the literature concerning tests performed in a hydrogen environment. Nevertheless, it has been highlighted in Subsections 2.2.1 and 2.2.2 that Type IV tanks are *thermolabile*. This characteristic allows for the prediction of a worse performance than that attributed to Type III tanks; thus, the metric m is expected to assume at least a value of $m = 0.945$. However, these results were achieved under very unfavorable filling rate conditions. In the tests conducted by [151], the gaseous hydrogen reached temperatures above 85°C. Consequently, these tests may yield better results if conducted using the strategies outlined in Tab. 4.5.

From these analyses, it becomes apparent that there exist significant discrepancies between the conventional hydraulic tests, as outlined in [27], and the tests conducted under actual hydrogen environmental conditions, particularly concerning the fatigue life of Type III and Type IV for hydrogen gas tanks. When these tanks are exposed to real-world hydrogen conditions, they are subjected to thermo-mechanical cyclic loading, which stems from the Joule-Thomson effect coupled with hydrogen embrittlement. These factors, significantly impacting the integrity and longevity of the storage vessels, are not adequately represented in the standard hydraulic test protocols.

Ambient Temperature

In accordance with [37], the temperature ranges considered for ambient conditions extend from -40°C to 85°C. These ranges encompass all possible operational scenarios, from the tank's performance in subzero environments to its placement in warmer areas such as within the propulsion system.

As showed in Subsection 2.2.6, Type III and IV tanks were tested at 125% of the FP. From Fig. 2.6a, it is observable that at 125% of the FP, Type III tanks can withstand ambient temperatures of -40°C, 27.5°C (the average temperature between 20 and 35°C, as utilized by the authors in [124]), and 85°C (with 95% RH) before leaking, corresponding to 12,000 cycles, 24,500 cycles, and 30,000 cycles respectively.

Furthermore, as depicted in Fig. 4.1, under a 125% FP, Type III tanks can endure 22,965 cycles. However, [123] does not report the ambient temperature at which the experiments were conducted. Nevertheless, the study suggests that the experiments were carried out indoors, thus a conservative average temperature of 19°C is assumed.

In this scenario, an ambient temperature of -40°C corresponds to an $S = 5$ rating, whereas the most favorable condition, $S = 1$, is associated with a temperature of 85°C. As discussed in the Subsection 2.2.6, this correlation is attributed to the effects of autofrettage and differences in thermal expansion rates. The theoretical interpolation of the data is presented in Fig. 4.3.

The value of m is calculated as follows:

$$m = \frac{30,000 - 12,000}{30,000} = 0.6$$

resulting in a maximum degradation index I of $I = m \times 5 = 3$, with a proportionality factor $p = \frac{0.2 \times I}{5} = m \times 0.2 = 0.12$. Using Fig. 4.3, theoretical intervals of the FP% were assigned to the indicator S, guiding the reduction of the component's life from 0 to 60%, as shown in Tab. 4.3.

From Fig. 2.6b, it is observed that Type IV tanks at 125% of the FP can withstand at least 45,000 cycles at temperatures of both -40°C and 27.5°C (this is the average temperature between 20°C and 35°C, as employed by the authors in [124]), with no instances of failure noted. Given that the tanks did not experience failure, this cycle count has been adopted as a reference point, employing a conservative approach. At 85°C (with 95% RH), the

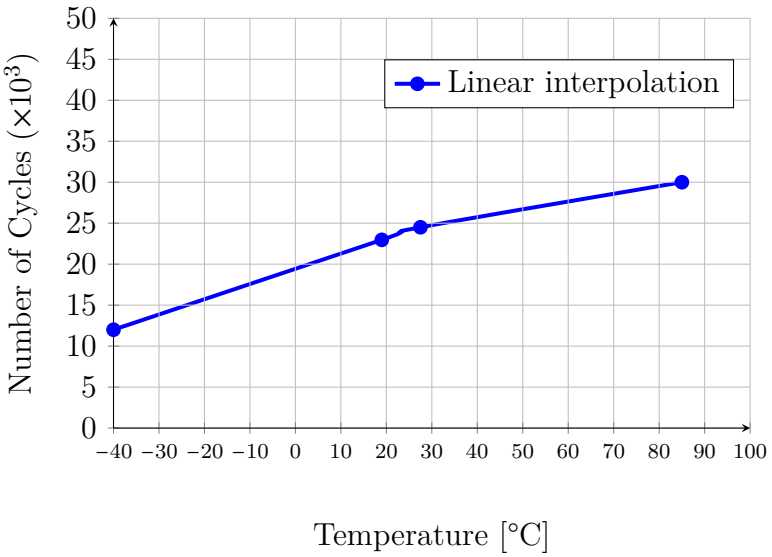

Figure 4.3 Relationship between ambient temperature and number of life cycles for Type III Tanks at 125% FP.

Table 4.3 Assignment of theoretical ambient temperature ranges to the S Indicator for Type III tanks.

Temperature [°C]	**Service Life Reduction $f(x)$%**	**S**	***I***
85 (95% RH) to 40	0 to 12.0	1 (up to 12.0%)	0.6
40 to 10	12.0 to 24.0	2 (up to 24.0%)	1.2
10 to 0	24.0 to 36.0	3 (up to 36.0%)	1.8
0 to -20	36.0 to 48.0	4 (up to 48.0%)	2.4
-20 to -40	48.0 to 60.0	5 (up to 60.0%)	3.0

Type IV tank can withstand 34,018 cycles. The theoretical interpolation of the data is depicted in Fig. 4.4.

The value of m is calculated as follows:

$$m = \frac{45,000 - 34,018}{45,000} = 0.244$$

Consequently, the maximum degradation index I is derived to be $I = m \times 5 = 1.22$, with a proportionality factor p calculated as: $p = \frac{0.2 \times I}{5} = m \times 0.2 = 0.0488$. Through Fig. 4.4, theoretical ranges of the room temperature were assigned. Through Fig. 4.4, theoretical ranges of the room temperature are allocated to the indicator S to the indicator S, effectively guiding the reduction of the component's life from 0 to 60%, as demonstrated in Tab. 4.4.

Filling strategies and timing

The analysis of the rapid filling process for hydrogen storage vessels, as discussed in Subsection 2.2.2, offers substantial insights into the effects of filling rate on the thermal

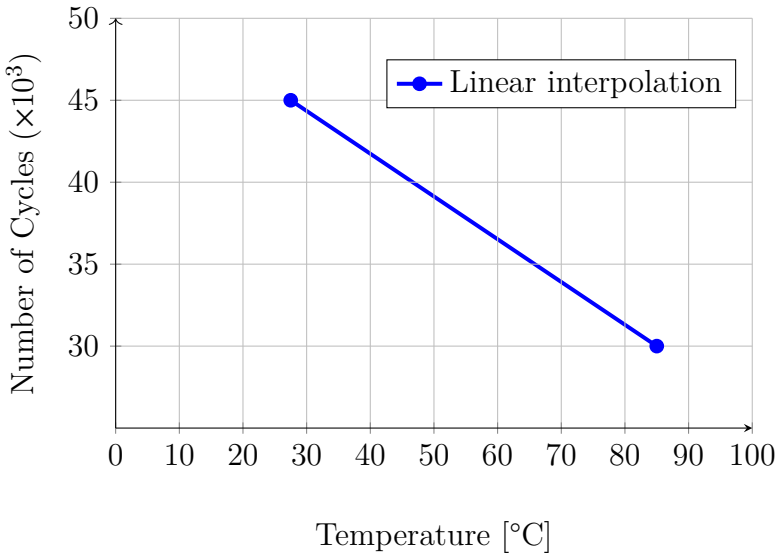

Figure 4.4 Relationship between ambient temperature and number of life cycles for Type IV Tanks at 125% FP.

Table 4.4 Assignment of theoretical ambient temperature ranges to the S Indicator for Type IV tanks.

Temperature [°C]	**Service Life Reduction $f(x)$ %**	**S**	I
-40 to -20	0 to 4.88	1 (up to 4.88%)	0.24
-20 to 0	4.88 to 9.76	2 (up to 9.76%)	0.48
0 to 10	9.76 to 14.64	3 (up to 14.64%)	0.73
10 to 40	14.64 to 19.52	4 (up to 19.52%)	0.97
40 to 85 (95% RH)	19.52 to 24.40	5 (up to 24.40%)	1.22

and mechanical stresses experienced by the tank. The critical interplay between the filling rate and the thermal dynamics within the tank has direct implications for the safety and efficiency of the refueling process, as underscored by key findings from empirical studies.

Initially, the established relationship between the increase in tank pressure and the corresponding rise in gas temperature during rapid filling is highlighted. Managing these thermal dynamics is crucial to preventing negative impacts on the refueling process, as an uncontrolled increase in filling rate can result in temperature rises exceeding industry-standard safety limits. Furthermore, the analysis underscores that several filling condition parameters (such as initial pressure, final pressure, incoming gas temperature, ambient temperature, and flow rate) have significant impacts on the internal gas temperature at the conclusion of the filling process. Literature suggests that a reduction in the filling rate leads to a more favorable thermal response, thus reducing the likelihood of surpassing the critical temperature threshold. Additionally, the review indicates that pre-cooling the incoming gas serves as an effective method to lower the maximum gas temperature within the tank, enhancing the safety and efficiency of the fueling process. The relationship between ambient temperature and the final gas temperature inside the tank further

highlights the effect of environmental conditions on the refueling dynamics. Moreover,

Table 4.5 Summary of strategies to improve the hydrogen fueling process.

Strategy	Description
Filling rate control	Reduce the speed at which hydrogen is pumped into the tank to mitigate excessive temperature increases.
Pre-cooling of incoming gas	Lower the temperature of hydrogen before entering the tank to reduce the peak temperature achieved during refueling.
Ambient conditions control	Monitor ambient temperatures to minimise thermal effects.
Tank material and design	Utilize materials with similar thermal expansion coefficients and optimize tank design to enhance thermal management during filling.

the research underscores the significant influence of tank design and material on thermal behavior during refueling. Notably, Type III tanks, which are typically constructed from aluminum alloys, tend to exhibit lower gas temperatures than Type IV tanks, attributable to differences in material thermal properties and tank geometries. This distinction is vital for the design and selection of hydrogen storage vessels, stressing the necessity for materials with superior thermal diffusivity and optimized design to counteract rapid temperature increases. The most important enhancement strategies are summarized in Tab. 4.5.

Humidity

The Subsection 2.2.7 underscores the significantly detrimental impact of moisture on the structural integrity of carbon fiber-reinforced and glass fiber-reinforced epoxy composites, which are commonly used in the construction of Type III and IV tanks. Studies have demonstrated a noticeable reduction in the mechanical and shear strengths of these composites, particularly at elevated temperatures following moisture absorption. This degradation is due to hydrolytic and chemical deterioration processes initiated by water ingress, adversely affecting the thermo-mechanical properties of the tank materials.

Moreover, the impacts of humidity are intensified under thermal cycling conditions prevalent in aerospace applications. Elevated levels of relative humidity lead to stiffness reduction, crack formation, and delamination within carbon fiber composite materials, significantly diminishing the fatigue life of these components. Moisture notably impairs the mechanical properties of GFRPs, especially when subjected to freeze-thaw cycles typical in high-altitude environments. Distinctively, while dry GFRP materials may resist such thermal cycling with minimal impact, the introduction of moisture results in a considerable decrease in tensile and in-plane shear strengths, attributable to micro-crack formation and the plasticization of the polymer matrix.

Collectively, these findings illuminate a critical vulnerability of Type III and IV tanks to environmental humidity, particularly under thermal cycling and elevated temperature

conditions. The presence of moisture not only induces physical damage through microcrack creation and delamination but also chemically modifies the composite materials, resulting in a compounded effect that significantly reduces the service life and structural reliability of these tanks. However, due to a lack of data, it is not possible to assign the metric m and the scale of indicator S. Nevertheless, the conducted investigation clearly demonstrates the necessity for rigorous environmental conditioning and humidity control in the operation of Type III and IV hydrogen storage vessels, particularly in aerospace and vehicle applications where they are subjected to harsh and fluctuating climatic conditions. Therefore, the placement of these tanks in extremely humid environments should be avoided.

Table 4.6 Strategies for moisture control.

Strategy	**Description**
Moisture control	Implement dehumidifiers or maintain controlled environments to mitigate the adverse effects of moisture absorption.
Temperature regulation	Maintain stable temperatures or employ preconditioning procedures before exposure to extreme conditions.
Protective coatings	Apply water-repellent coatings to reduce water ingress in composite materials, thus preserving their structural integrity.

Vibrations

The analysis of the inherent vulnerability of Type III and Type IV hydrogen storage tanks to vibrations reveals that the fatigue behavior of materials under the influence of vibrations is complex, influenced by factors such as frequency range, GRMS and the presence of defects within the material structure. Components made of CFRP, essential to both types of tanks, exhibit a certain level of resilience against vibration-induced fatigue. However, the specific failure criteria under such conditions are not clearly defined, highlighting a potential area for further research. In addition, elevated temperatures result in a more marked reduction in fatigue life, pointing to a specific vulnerability especially relevant to Type IV tanks due to their composite nature and potential thermal sensitivity.

Table 4.7 Strategies for vibration management.

Strategy	Description
Vibration monitoring	Implement regular inspections and monitoring for signs of fatigue, particularly in components known to be exposed to significant vibration levels. Early detection of crack propagation may prevent components failure.
Material selection	In configuration with high levels of vibration, it would be advisable to use composite materials in applications with low ambient temperatures, while aluminium alloys could be considered for applications involving extreme ambient temperatures.

4.1.2 Calculation of failure rates for type III and IV tanks for hydrogen gas storage applications

As documented in Subsection 2.6.4, for Type III and IV tanks, the reference failure rates based on the number of life cycles up to the breakdown of the components are respectively: $\lambda_{TypeIII} = \frac{1}{93{,}883} = 1.07 \times 10^{-5} \left[\frac{1}{\text{cycles}}\right]$ and $\lambda_{TypeIV} = \frac{1}{94{,}000} = 1.06 \times 10^{-5} \left[\frac{1}{\text{cycles}}\right]$. Initially, these failure rates must be adjusted according to the operational conditions to which these tanks are exposed. Post-filling, the stabilized pressure after cooling is lower compared to that immediately after refueling. To counteract this phenomenon, the target final pressure is established to exceed the NWP, hence the maximum filling pressure has been determined to be 125% of the NWP, as elaborated in Subsection 2.2.3. Referring to Fig. 4.1, Fig. 4.2, Tab. 4.2 and Tab. 4.3, at 125% of the FP the Type III and IV tanks experience a lifespan reduction of $f(x) = 0.756$ e $f(x) = 0.5212$, respectively. Consequently, employing Equation (2.20), the revised failure rates are:

$$\lambda_{125\%\text{ FP, Type III}} = \frac{\lambda_{\text{old}}}{(1 \pm f(x))} = \frac{\lambda_{\text{old}}}{(1 - 0.756)} = \frac{1}{22965} = 4.35 \times 10^{-5} \left[\frac{1}{\text{cycles}}\right]$$

$$\lambda_{125\%\text{ FP, Type IV}} = \frac{\lambda_{\text{old}}}{(1 \pm f(x))} = \frac{\lambda_{\text{old}}}{(1 - 0.5212)} = \frac{1}{45000} = 2.22 \times 10^{-5} \left[\frac{1}{\text{cycles}}\right]$$

By applying Equation (3.7), it's possible to scale the effects of the hydrogen environment (including gas temperature and potential hydrogen embrittlement) on Type III tanks, for which a degradation index of $I = 4.725$ has been calculated in the Subsection 4.1.1, corresponding to a lifespan reduction of $f(x) = 94.5\%$. The same percentage reduction will be applied to the Type IV tanks; however, as previously mentioned, the effect could be even worse due to the thermolability of the polymer liner in Type IV tanks and hydrogen

permeation. Therefore:

$$\lambda_{\text{hydrogen, Type III}} = \frac{\lambda_{\text{old}}}{(1-f(x)) \times (1-f(x))} = \frac{\lambda_{125\%\text{ FP, Type III}}}{1-0.945} = \frac{1}{1263} = 7.91{\times}10^{-4} \left[\frac{1}{\text{cycles}}\right]$$

$$\lambda_{\text{hydrogen, Type IV}} = \frac{\lambda_{\text{old}}}{(1-f(x)) \times (1-f(x))} = \frac{\lambda_{125\%\text{ FP, Type IV}}}{1-0.945} = \frac{1}{2475} = 4.04{\times}10^{-4} \left[\frac{1}{\text{cycles}}\right]$$

The tests previously taken into consideration were performed at ambient temperature, which according to Tab. 4.3 and Tab. 4.4, indicates that for Type III tanks the starting indicator is $S = 2$. Therefore, for Type IV tanks $S = 4$ is the starting point. Considering Type III tanks, as the tests were conducted at ambient temperature and since the performance of these tanks improves at higher ambient air temperatures, it implies that from $S = 2$ to $S = 5$, the MNCTF should increase by a proportionality factor $p = 0.12$ (calculated previously in the Subsection 4.1.1). Thus, for $S = 5$ the MNCTF should be scaled by an amount $\Delta f(x) = 0.12 + 0.12 + 0.12 = 0.36$. Conversely, from $S = 2$ to $S = 1$, the MNCTF needs to be scaled down. Regarding Type IV tanks, from $S = 4$ to $S = 5$, the MNCTF should be scaled by a proportionality factor of $p = 0.0488$, while towards $S = 1$, the MNCTF will increase by a proportionality factor $p = 0.0488$. Specifically, at $S = 1$ the MNCTF should be increased by an amount $\Delta f(x) = 0.0488 + 0.0488 + 0.0488 = 0.1464$. Starting from the previously obtained values of λ ($\lambda_{\text{hydrogen, Type III}} = \frac{1}{1263} = 7.91 \times 10^{-4} \left[\frac{1}{\text{cycles}}\right]$, $\lambda_{\text{hydrogen, Type IV}} = \frac{1}{2475} = 4.04 \times 10^{-4} \left[\frac{1}{\text{cycles}}\right]$), by varying the indicator S from 1 to 5, the results highlighted in Tab. 4.8 and Tab. 4.9 are obtained.

Table 4.8 Impact of theoretical ambient temperature ranges to the failure rate λ for Type III tanks.

Temperature [°C]	**S**	λ [1/cycles]
85 (95% RH) to 40	1 (+12%)	$\lambda_{\text{new}} = \frac{\lambda_{\text{old}}}{(1+\Delta f(x))} = 7.07 \times 10^{-4}$
40 to 10	2*	$\lambda_{\text{old}} = 7.91 \times 10^{-4}$
10 to 0	3 (-12%)	$\lambda_{\text{new}} = \frac{\lambda_{\text{old}}}{(1-\Delta f(x))} = 9.00 \times 10^{-4}$
0 to -20	4 (-24%)	$\lambda_{\text{new}} = \frac{\lambda_{\text{old}}}{(1-\Delta f(x))} = 1.04 \times 10^{-3}$
-20 to -40	5 (-36%)	$\lambda_{\text{new}} = \frac{\lambda_{\text{old}}}{(1-\Delta f(x))} = 1.23 \times 10^{-3}$

* The tank was subjected to fatigue cycles at room temperature; thus, within this range, the failure rate does not need to be updated

Table 4.9 Impact of theoretical ambient temperature ranges on the failure rate λ for Type IV tanks.

Temperature [°C]	**S**	λ [1/cycles]
-40 to -20	1 (+14.64%)	$\lambda_{new} = \frac{\lambda_{old}}{(1+\Delta f(x))} = 3.52 \times 10^{-4}$
-20 to 0	2 (+9.76%)	$\lambda_{new} = \frac{\lambda_{old}}{(1+\Delta f(x))} = 3.68 \times 10^{-4}$
0 to 10	3 (+4.88%)	$\lambda_{new} = \frac{\lambda_{old}}{(1+\Delta f(x))} = 3.85 \times 10^{-4}$
10 to 40	4*	$\lambda_{old} = 4.04 \times 10^{-4}$
40 to 85 (95% RH)	5 (-4.88%)	$\lambda_{new} = \frac{\lambda_{old}}{(1-\Delta f(x))} = 4.24 \times 10^{-4}$

* The tank was subjected to fatigue cycles at room temperature; thus, within this range, the failure rate does not need to be updated

Plotting the results, Fig. 4.7 and Fig. 4.8 are obtained.

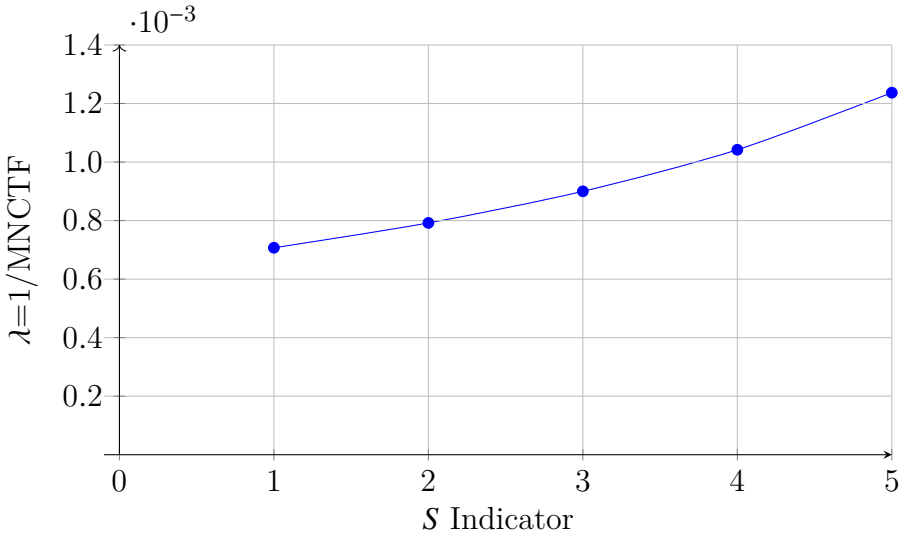

Figure 4.5 Impact of theoretical ambient temperature ranges on the failure rate λ for Type III tanks

The highest value obtained in Fig. 4.7 and Fig. 4.8 is the outcome of the combined effect of all conditions addressed in this study. More precisely, these are the conditions under which it was feasible to apply the calculation methodology, since significant conditions such as vibrations and humidity were not considered. Humidity is included in the study only in the conditions of $S = 5$ and $S = 1$ when the test was conducted at 85°C with a RH of 90%. Thus, for Type IV tanks, humidity was indirectly considered in the worst-case scenario, whereas for Type III tanks, it was considered in the best-case scenario. The calculations performed are summarized in Tab. 4.10 and Tab. 4.11.

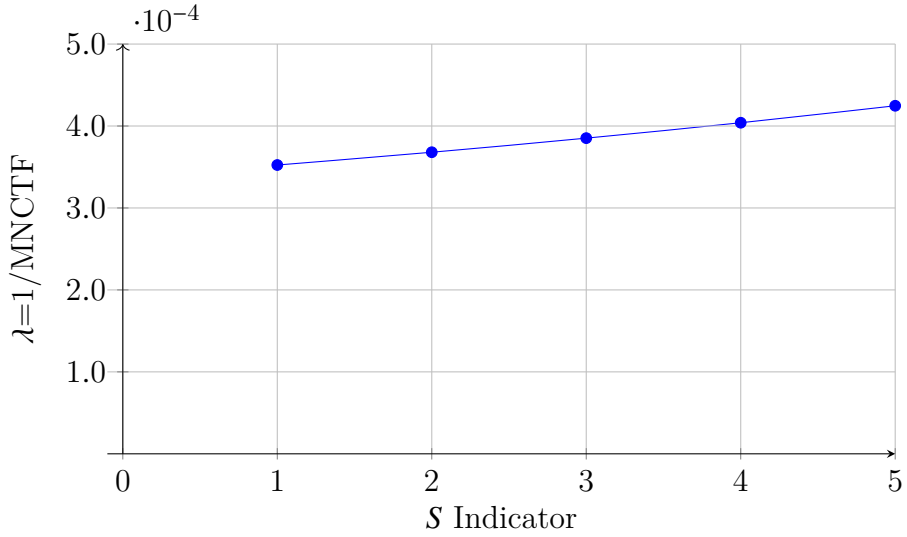

Figure 4.6 Impact of theoretical ambient temperature ranges on the failure rate λ for Type IV tanks

Table 4.10 Summation of operating and environmental conditions on the Type III failure rate.

Discriminator	$f(x)$	$\frac{\lambda_{\mathbf{old}}}{\sum_{i=1}^{n}(1\pm f(x_i))}$
Hydraulic Cycling test*	0	1.07×10^{-5}
FP 125%	0.755	$\lambda_{\text{new}}=\frac{\lambda_{\text{old}}}{(1-f(x))}=4.35\times10^{-5}$
Hydrogen Environment	0.945	$\lambda_{\text{new}}=\frac{\lambda_{\text{old}}}{(1-f(x))(1-f(x))}=7.90\times10^{-4}$
Temperature of the Surroundings (S=5)	0.360	$\lambda_{\text{new}}=\frac{\lambda_{\text{old}}}{(1-f(x))(1-f(x))(1-f(x))}=1.23\times10^{-3}$

* Conducted at room temperature

Table 4.11 Summation of operating and environmental conditions on the Type IV failure rate.

Discriminator	$f(x)$	$\frac{\lambda_{\mathbf{old}}}{\sum_{i=1}^{n}(1\pm f(x_i))}$
Hydraulic Cycling test*	0	1.06×10^{-5}
FP 125%	0.521	$\lambda_{\text{new}}=\frac{\lambda_{\text{old}}}{(1-f(x))}=2.22\times10^{-5}$
Hydrogen Environment	0.945	$\lambda_{\text{new}}=\frac{\lambda_{\text{old}}}{(1-f(x))(1-f(x))}=4.04\times10^{-4}$
Temperature of the Surroundings (S=5)	0.0488	$\lambda_{\text{new}}=\frac{\lambda_{\text{old}}}{(1-f(x))(1-f(x))(1-f(x))}=4.24\times10^{-4}$

* Conducted at room temperature

The respective trends, resulting from the sum of the operational and environmental conditions considered, are plotted in Fig. 4.7 and Fig. 4.8. Thus, the dramatic increase in failure rates correlated with the drastic reduction of MNCTF can be witnessed.

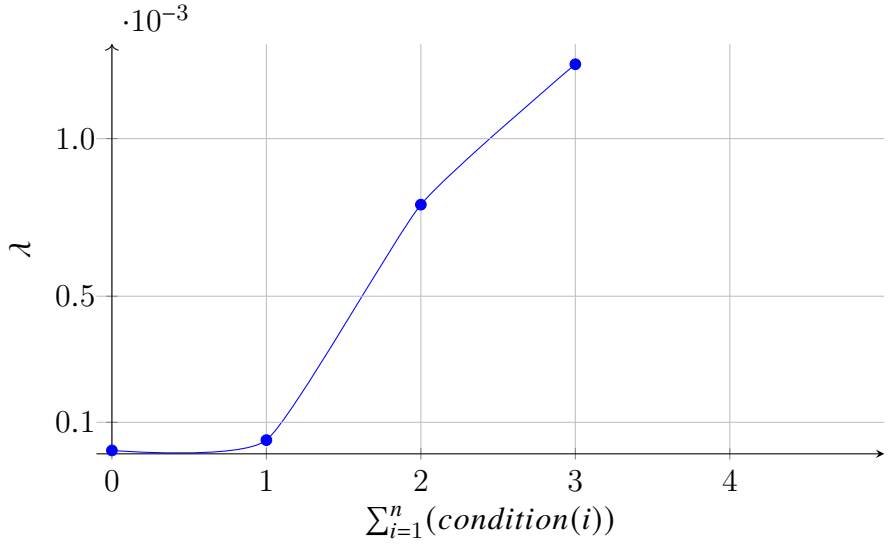

Figure 4.7 Failure rate trend of the Type III tank considering different operating and environmental conditions.

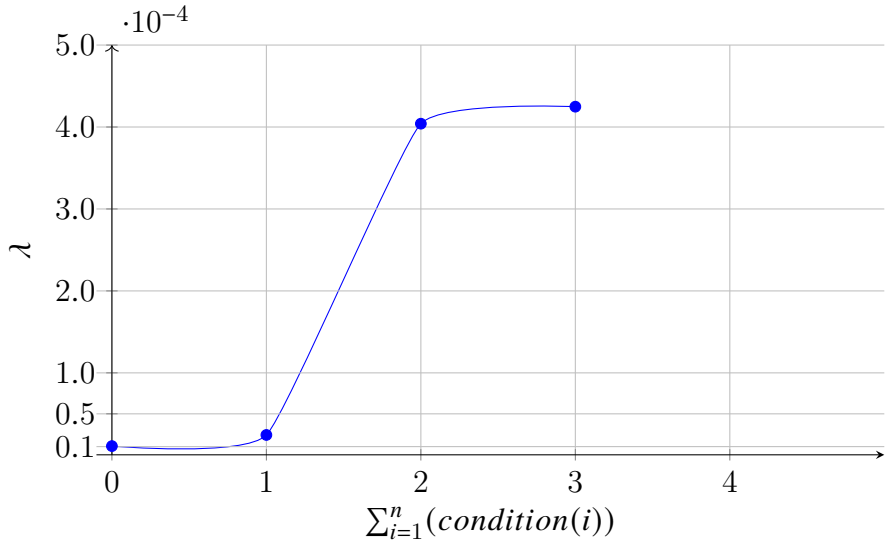

Figure 4.8 Failure rate trend of the Type IV tank considering different operating and environmental conditions.

As already discussed, various regulations [27, 51] mandate that tanks must withstand at least 12,000 cycles through hydraulic testing. However, Fig. 4.9 illustrates how different the results can be when considering realistic operational scenarios rather than scenarios with hydraulic testing. The standards state that through hydraulic tests, if a tank can complete 12,000 cycles without any leakage or breakage, it is expected to have an unlimited service life. Nevertheless, these types of tanks are predominantly used for applications involving gaseous hydrogen, which drastically reduces the lifespan of these components.

Through this analysis, it has been possible to highlight that various factors such as thermal stresses due to temperature cycles (caused by the increase in hydrogen temperature during the filling process), hydrogen corrosion, and extreme weather conditions (RH and room temperature) are factors that must not be absolutely overlooked.

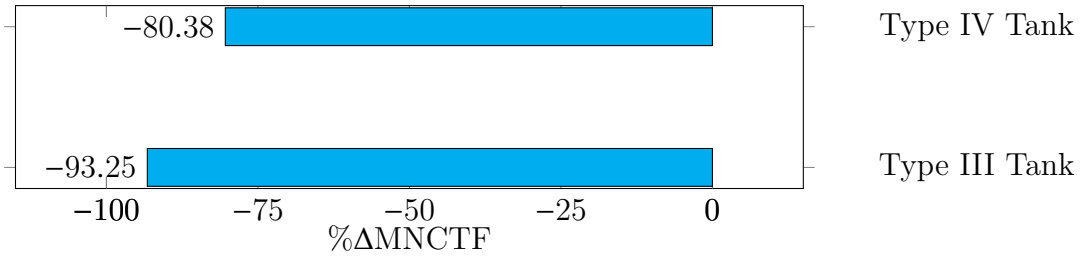

Figure 4.9 Percentage reduction of the calculated MNCTF compared to the MNCTF proposed by regulations for Type III and Type IV Tanks for hydrogen gas applications.

This significant discrepancy highlights a critical oversight in existing testing standards, which fail to adequately simulate the thermal cycling and material degradation effects associated with real-world hydrogen usage. The reliance solely on hydraulic testing, which overlooks the impacts of elevated temperatures and hydrogen embrittlement, could result in overly optimistic assessments of tank durability and safety. The findings of this analysis critically emphasize the limitations and gaps in the current testing standards for hydrogen storage tanks. They underscore the urgent need for revised testing protocols that include the effects of thermal cycling, hydrogen embrittlement, and gas permeation to provide a more accurate and comprehensive assessment of tank durability and safety throughout the component's entire lifespan. The call for enhanced testing standards is not just theoretical but is essential for ensuring the reliability and safety of hydrogen storage solutions in both vehicle and aircraft applications.

4.1.3 Liquid hydrogen tanks

Filling methods and rates

Just as with tanks used for gaseous hydrogen applications, liquid hydrogen tanks primarily focus on the thermal stress generated due to rapid temperature changes, local temperature variations, and effects induced by sloshing. These factors significantly influence the structural integrity and safety of the tanks.

The interaction between cryogenic liquid and tank walls results in notable temperature gradients, leading to heightened thermal stresses. This necessitates a meticulous approach that avoids sudden temperature shifts, thus reducing the likelihood of thermal stress concentrations. By controlling and improving the filling methods, it is possible to mitigate the stress states affecting the tank, thereby reducing the adverse effects of repeated pressure and temperature cycles on the tank's service life. Strategies for filling proposed to improve the stress state in the tank are shown in Tab. 4.12.

Table 4.12 Summary of improvement strategies for liquid hydrogen fueling process.

Strategy	Description
Controlled filling rate	Adopt a controlled, step-wise filling strategy to minimize thermal stress levels and prevent sudden temperature gradients within the tank; starting with an initial low feeding rate, then subsequently increasing the feeding rate in the main stage.
Filling technique	The top axial filling method is superior in reducing thermal stress compared to lateral or bottom filling methods. By promoting a more uniform temperature distribution, the top axial approach minimizes thermal stress levels, thus enhancing the tank's structural integrity during the filling process.
Temperature monitoring	Implement continuous temperature monitoring systems to detect and manage rapid temperature variations during the filling process.
Sloshing mitigation	Design filling protocols to minimize liquid sloshing, potentially incorporating anti-slosh baffles or adjusting filling angles to reduce the movement of liquid and associated thermal stress.
Tank material and design	Utilize materials with similar thermal expansion coefficients and optimize tank design to enhance thermal management during filling.

Low cycle fatigue analysis

While the structural design and testing standards for cryogenic composite tanks have advanced significantly, there remain critical gaps, particularly concerning the real-world effects of temperature cycles, hydrogen embrittlement, and the interaction between different materials used in the tank design. These gaps necessitate a reassessment of current standards and further research to ensure that the tanks can safely withstand the operational conditions they will face in practice.

In Subsection 2.3.4, two types of tanks from different studies are discussed, both embodying the characteristics of a Type III tank. However, for Type IV tanks used in cryogenic applications, with currently available technologies and materials, they appear to be unreliable, as discussed in Subsection 2.3.3. Regarding the study conducted by [4], the fact that the tank can reach 94.2 MPa implies that the tank structure is very heavy. Thus, this type of tank could be utilized in a system where the use of a gaseous hydrogen tank (illustrated in Fig. 2.12) is not included.

The layout studied by Meissner et al. [85] could be considered with a lightweight cryogenic tank, such as the one studied by [2]. However, in the study conducted by [4], the tank was cycled with liquid nitrogen 100 times, without leading to tank failure. Thus, unless the tank is maintained at a constant temperature and is not used in applications where it is emptied and refilled (thereby undergoing temperature cycles), the results are not promising and reliable enough to be considered for the deployment of the tank into an aeronautic system.

Returning to the study by [2], the aluminum liner of the tank after 600 cycles is damaged, and such damage to the aluminum liner results in leakage, rendering the tank inoperative. Consequently, the tank is considered unusable once the liner is compromised. The studied tank, although not mentioned, reflects the criteria and materials of a Type III tank (being the operating pressure of 0.2 MPa, the tank is much lighter compared to those used for gaseous hydrogen applications). Since the robustness of the aforementioned tank to pressure cycles alone is unknown, even though Type III tanks can withstand more than 90,000 cycles with purely hydraulic tests, a maximum value of 12,000 is assumed, referring to the standard [55].

$$m = \frac{12,000 - 600}{12,000} = 0.95$$

Assuming that the tank can withstand only 12,000 cycles with a hydraulic test, the impact of temperature cycles at the operating temperature of liquid hydrogen is enormous, similar to the impact of operational conditions of hydrogen in the applications of tanks for gaseous hydrogen.

Nevertheless, with the current data in literature and available sources, it appears even clearer that cryogenic tanks should be maintained at a constant temperature, avoiding emptying the tank except during scheduled maintenance intervals. In addition, as already discussed in Subsection 2.3.4, maintaining the tank at cryogenic temperatures can have positive effects on the properties of the tank. Thus, the operating temperature itself is

not a critical factor; it is the temperature cycles that, by changing the stress states within the tank, cause its useful life to decrease drastically.

Environmental factors

As discussed in Subsection 2.3.6, the lifetime of aluminum alloy in high humidity air is only 40% of that in dry air. Consequently, humidity could represent a significant factor when using a MLI as insulation and an aluminum alloy as the outer double wall. Qualitatively, a value of $m^* = 0.4$ is assigned to humidity for applications involving aluminum alloys. However, the focus should be on the liner in contact with hydrogen, as it has a much shorter service life compared to the unlikely rupture of the tank's outer wall (unless due to burst pressure). In addition, what really needs to be analyzed is the impact that humidity might have on the MLI, namely what risk the absorption of moisture by the tank's outer wall could pose to the vacuum state within the insulation. However, to avoid any negative effects that humidity could have, the same strategies outlined in Tab. 4.6 should be applied.

The same consideration applies to the external air temperature, given that there are no data in the literature, it would be necessary to evaluate whether the temperature cycles that the external wall of the tank undergoes could influence the vacuum state of the MLI. As for the impact on SOFI, in Subsection 2.3.5 it has already been discussed how humidity and temperature cycles can affect the insulatipn over time, the impact of which degradation will be discussed in the Subsection 4.2.4.

4.1.4 Fuel cell

Sub-freezing conditions

The studies addressed in Subsection 2.5.5 suggest that while fuel cells have potential for use in colder environments, significant hurdles remain, particularly concerning start-up procedures and sustained operations under subfreezing conditions.

Firstly, the degradation of the PEM and the MEA due to freezing water in the pores and the subsequent mechanical stress from ice formation is a crucial concern. The diversity of opinions on the temperature thresholds leading to significant degradation underscores the complexity of the issue and the necessity for more definitive thresholds tailored to specific operational contexts.

Secondly, the studies emphasize the importance of water management within the fuel cell, especially in freezing conditions. Achieving a balance between removing excess water to prevent ice-related damage and retaining enough water for proton conductivity and membrane hydration is delicate and critical for optimal performance. This balance becomes even more challenging in aviation environments where external conditions, such as air pressure and temperature, can vary significantly.

Additionally, the findings indicate that operational protocols, such as pre-purging and insulation, can substantially affect a fuel cell's ability to start and operate in cold conditions. These procedures, alongside controlled start-up sequences, are viable strategies to reduce the risks of cold-start failures and subsequent mechanical damage. Currently, there are no available data to apply the developed methodology (Subsection 3.1.1), but it is evident that the subfreezing temperatures with the currently available technologies could be fatal. Thus, a qualitative degradation index $I = 5$ ($m^* = 1$) is assigned.

From these findings, several strategies for improving fuel cell performance in subfreezing conditions can be drawn:

Table 4.13 Summary of improvement strategies for start-ups under subfreezing conditions.

Strategy	**Description**
Enhanced water management	Develop advanced water management systems that can adapt to changing conditions to minimize ice formation while maintaining membrane hydration. This may include innovative water removal systems that activate based on temperature thresholds or systems that redistribute water within the cell to prevent local freezing.
Optimized start-up procedures	Implement pre-start procedures, such as pre-purging and thermal management strategies, to condition the fuel cell for cold starts. Develop adaptive start-up sequences that can adjust based on the initial temperature and humidity conditions to reduce the risk of ice-related damage.
Operational parameter optimization	Determine the optimal operational parameters, such as air stoichiometry and feed gas temperature, for different external conditions. This optimization should balance the need for membrane hydration with the risks of ice formation and membrane drying.
Pressure and airflow management	Address the challenges posed by reduced external air pressure and varying temperature conditions typical of high-altitude flights. Develop systems that can adjust airflow and pressure dynamically to maintain optimal conditions within the fuel cell.

Vibrations

The findings provided in Subsection 2.5.6 emphasize the critical impact of mechanical vibrations on the integrity and performance of PEMFC, especially within automotive and

aerospace applications. These insights are crucial for guiding the design, installation, and operational strategies of fuel cells in environments where mechanical vibrations are common.

The reported studies exhibit a range of effects that vibrations can have on fuel cells, from negligible to significantly detrimental. It is evident that vibrations, particularly those at higher frequencies and amplitudes, can accelerate the degradation of PEM fuel cells, manifesting through reduced gas-tightness, power output, and the accelerated propagation of micro-scale defects such as delamination and crack formation. This degradation directly impacts the longevity and efficiency of fuel cells, underscoring the necessity for effective vibration mitigation strategies. Qualitatively, the higher the amplitudes, the higher the indicator S. From the limited data available, the worst-case scenario was identified with $A = 4g$ and w = 40 Hz. From these findings, starting from an amplitude of $A = 4g$, an indicator $S = 5$ could be assigned. Since there are no studies on the life span of the fuel cell to account for vibration-induced degradation, in this case, the delamination length reached is considered. With this vibration loads, a delamination length of 0.1 mm was reached after 2.94×10^4 hygrothermal cycles, while without vibrations after 3.27×10^4 cycles.

Thus, the qualitative value of m^* is calculated as follows:

$$m^* = \frac{3.27 - 2.94}{3.27} = 0.10$$

This means that with $S = 5$, the fuel cell degrades 10% faster ($I = 0.5$), reaching the delamination length threshold sooner. Obviously, the vibrations induced in an aircraft system due to the engine and other components are greater (as showed in Tab. 2.1), therefore new tests with greater amplitudes need to be set.

Regarding the effects of operational conditions such as temperature and humidity, these parameters are strongly linked to the performance of the fuel cell itself. It is evident that the lower the temperature and stress due to humidity cycles, the longer the lifespan of the fuel cells. However, to ensure the proper functioning of fuel cells and to make them comparable to conventional fuel-powered aircraft, the development of new materials capable of withstanding these operating conditions or new studies to improve the efficacy of these systems appears necessary.

4.2 Predicting relief valves service life through computational analysis

In this section, the significant results obtained through computational analysis will be discussed and introduced. Starting from subsection 4.2.1, the effects of low liquid hydrogen filling levels on the evaporation of liquid hydrogen and consequently on the activation of the relief valves will be investigated. Subsequently, in subsection 4.2.2, the effect of different venting pressures on the integrity of cryogenic tanks and, most importantly, on the lifespan of the relief valves will be discussed. Additionally, in subsection 4.2.3, the effects of various climatic conditions on the performance of different types of insulation and consequently on the activation of the relief valves will be analyzed. Furthermore, in subsection 4.2.4, the degradation of SOFI and MLI and their impact on relief valves in cryogenic applications will be examined.

4.2.1 Impact of filling levels on the activation of relief valves

As illustrated in Fig. 3.5 and discussed in Subsection 3.2.2, the coefficient ϕ is inversely proportional to the hydrogen liquid fill level of the tank; the higher β, the lower ϕ. Consequently, from Equation 3.27 it is already predictable that the pressure increase in the tank is lower with a higher fill level. To demonstrate the effect of the fill level on the increase in tank pressure and consequently on the activation of the relief valves, the tanks identified in Tab. 3.5 were taken as reference.

In the context of a SOFI characterized by a thermal conductivity of k = 0.0079 $\frac{W}{mK}$ [33], the aggregate thermal resistances, derived from Equation. 3.35, Equation. 3.36 and Equation. 3.38, are quantified R = 0.91 $\frac{W}{mK}$ for the spherical cylinder, R = 0.23 $\frac{W}{mK}$ and R = 0.45 $\frac{W}{mK}$ for the two cylindrical tanks. When addressing climatic variables, empirical temperature data from diverse global airport locations were incorporated, spanning from the most severe to normal environmental conditions. Pertaining to the aircraft's idle period at the airport, the analysis adopts the longest duration as it represents the most exigent scenario, a time during which the aircraft's relief valves are presumed to be in uninterrupted operation. Tab. 4.14 summarizes all the data taken into consideration. Additionally, in instances where the relief valves are activated during the aircraft's layover between successive flights, such occurrences should be integrated into Equation 3.29. This consideration is particularly crucial given that aircraft typically arrive at airports with diminished fuel levels, leading to an escalation in hydrogen evaporation rates.

Table 4.14 Summary of data for computational analysis concerning the influence of filling level on hydrogen evaporation.

Category	**Parameter**	**Value**	**Unit**	**Remark**
Insulation performance	Thermal conductivity	0.0079	$\frac{W}{mK}$	SOFI BX-265 [33]
	Total thermal resistance	0.91*	$\frac{W}{K}$	Eq. 3.38
		0.45**	$\frac{W}{K}$	Eq. 3.38
		0.23**	$\frac{W}{K}$	Eq. 3.38
Climatic Conditions	Temperatures from 9 p.m. to 10 a.m.	27 – 33	°C	21/07/2022 Napoli airport [56]
Operating Conditions	Average overnight stand time[1]	13	hours	[34]
	Operating pressure	2	bar	
	Venting pressure	2.2	bar	
	Filling level	10 – 92	%	
	Tank Volume	25.9**	m^3	Tab. 3.5
		34.5*	m^3	Tab. 3.5
		51.8**	m^3	Tab. 3.5

[1] Airbus A320-214, China Express Airlines
* Spherical tank
** Cylindrical tank

By applying Equation 3.29, through Matlab Fig. 4.10 is obtained. The core algorithm for this computational analysis is detailed in the appendix (function 1 and 3). From Fig. 4.10, two intriguing observations emerge: firstly, the failure rate increases as the tank's filling level decreases; secondly, for cylindrical tanks at equal filling levels, the failure rate escalates as the volume of the tank containing liquid hydrogen diminishes. These phenomena fundamentally occur because a smaller mass of liquid hydrogen leads to higher rates of hydrogen evaporation within the tank, thereby accelerating the increase in internal tank pressure. From a thermodynamic perspective, a reduced mass of liquid hydrogen entails a lower heat capacity, meaning less energy is stored by the hydrogen, making it more susceptible to temperature increases.

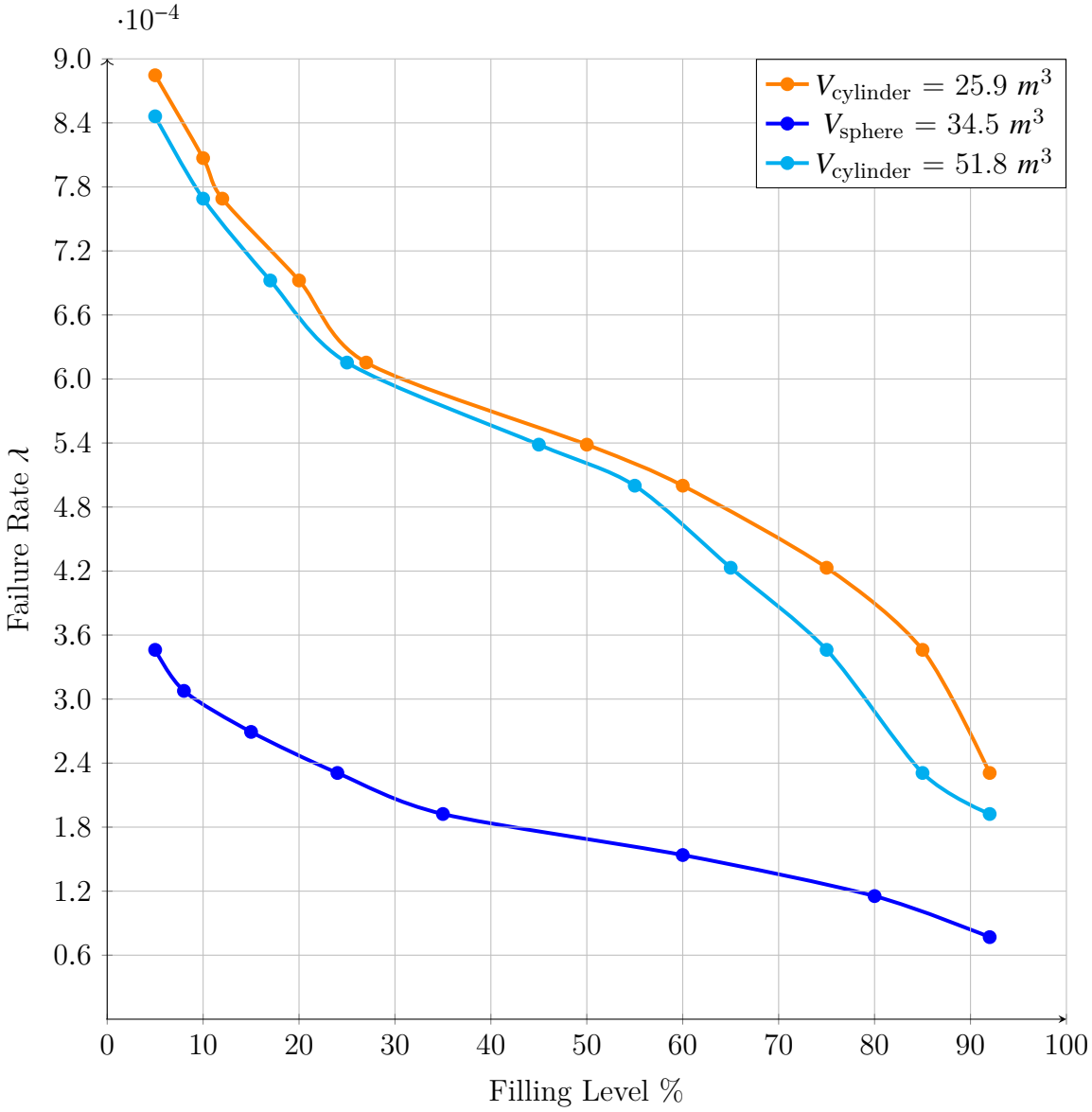

Figure 4.10 Influence of the filling level on the failure rate of relief valves.

The tank with the larger volume possesses a greater heat exchange surface, thereby allowing more heat to enter the tank. As inferred from Equation 3.27, the larger the volume of liquid hydrogen, the lower the pressure increase. From Fig. 4.10, this difference, between the two tanks, one having double volume of the other, is not significantly pronounced; at an equivalent failure rate, the filling level of the larger tank is slightly lower; thus, to maintain the same failure rate, lower percentages of hydrogen must be used. Despite the fact the tank with a volume of V = 51.8 m^3 has an extremely greater thermal capacity, this occurs fundamentally because it possesses a significantly larger heat exchange surface. Therefore, with the application of SOFI instead of MLI, the heat entering the tank is greatly sensitive to the thermal exchange surface. Concerning the tank with spherical geometry, despite having a larger volume than the cylinder with V = 25.9 m^3, it exhibits

a significantly lower failure rate compared to the two cylindrical tanks. Once again, this phenomenon is due to the fact that, for equal volumes, a sphere has a much smaller heat exchange surface compared to a cylinder. From this analysis, it is discernible that for the same volume, to achieve a comparable failure rate trend, cylindrical geometry tanks require more effective insulation than those of spherical geometry. This analysis distinctly indicates that liquid hydrogen tanks should ideally be refilled before being left idle at airports during downtime periods. Firstly, this strategy would allow the tank to maintain a stable temperature, thereby minimizing the thermal stress caused by temperature fluctuations and consequently enhancing its fatigue life. Secondly, it would reduce the number of activations of relief valves and all other components essential for the system's proper functioning, thus decreasing their failure rates.

4.2.2 Effect of the venting pressure on the relief valves performance

From the flowchart depicted in Fig. 3.6, it is evident that the higher the venting pressure, the fewer relief valve triggers occur. However, a higher venting pressure is correlated with a greater impact on the fatigue life of the tank. Additionally, increased venting pressure leads to more pronounced thermal stratification within the tank; hence, a lower venting pressure results in more stable liquid hydrogen temperatures. To assess the venting pressure's impact on relief valves performance, the trends of the failure rates for the cylindrical tank exhibiting a higher failure rate were extracted from Fig. 4.10. The parameters considered are summarized in Tab. 4.15, with the results illustrated in Fig. 4.11. The core algorithm for this computational analysis is detailed in the appendix (function 1 and 4).

In Fig. 4.11, five insulating materials were examined, considering a 30% filling level only for the MLI. From the figure, it is evident that, at equal thickness, the worse insulating material, the higher failure rate. Particularly, the worse insulation, the more λ curve shifts to the right.

The configuration illustrated in Fig. 2.12 lacks any device to improve thermal stratification inside the tank. In this context, it is deemed necessary for the configurations without an active or passive TVS to be equipped with a vacuum layer or MLI to mitigate the effects of thermal stratification On the other hand, the TVS could be used for cryogenic foam-insulated tanks (SOFI). However, all configurations with TVS are subject to venting pressure ranging from 7 kPa to 60 kPa [133, 134], which, as illustrated in Fig. 4.11, would lead to higher failure rates exceeding $\lambda = 10^{-3}\ \frac{1}{hour}$ when using SOFI (if the components of the TVS can perform the same number of cycles as the relief valves). With a vacuum layer, using these venting pressure ranges, it is possible to achieve a failure rate ranging from $8.84 \times 10^{-4}\ \frac{1}{hour}$ ($P_{\text{vent}} = 3.01$ bar) to $1.53 \times 10^{-4}\ \frac{1}{hour}$ ($P_{\text{vent}} = 3.23$ bar), while with MLI, the failure rate ranges from 7.69×10^{-5} ($P_{\text{vent}} = 3.01$ bar) to 3.84×10^{-5} ($P_{\text{vent}} = 3.02$ bar), resulting in a practically zero failure rate when the vent pressure exceeds the operating pressure of the tank by 30 kPa. Obviously, the use of vacuum layers and MLI

Table 4.15 Summary of data for computational analysis concerning the influence of venting pressures on the failure rate of relief valves.

Category	**Parameter**	**Value**	**Unit**	**Remark**
Insulation performance	Thermal conductivity	7.9×10^{-3}	$\frac{W}{mK}$	SOFI BX-265 I [33]
		13.9×10^{-3}	$\frac{W}{mK}$	(SOFI, BX-265 II) [33]
		18.6×10^{-3}	$\frac{W}{mK}$	(SOFI, BX-265 III) [33]
		8×10^{-4}	$\frac{W}{mK}$	(vacuum layer) [141]
		2.5×10^{-5}	$\frac{W}{mK}$	(MLI) [141]
	Total thermal resistance	0.45	$\frac{W}{K}$	Eq. 3.38
		0.23	$\frac{W}{K}$	Eq. 3.38
		0.19	$\frac{W}{K}$	Eq. 3.38
		4.37	$\frac{W}{K}$	Eq. 3.38
		79.6	$\frac{W}{K}$	Eq. 3.38
Climatic Conditions	Temperatures from 9 p.m. to 10 a.m.	27 – 33	°C	21/07/2022 Napoli airport [56]
Operating Conditions	Average overnight stand time[1]	13	hours	[34]
	Operating pressure	3	bar	
	Venting pressure	3.01 – 4.00	bar	
	Filling level	92	%	
	Tank Volume	25.8*	m^3	Tab. 3.5

[1] Airbus A320-214, China Express Airlines
* Cylindrical tank

would always be advantageous compared to SOFI, but due to weight and space constraints (MLI requires two walls to support the vacuum, resulting in heavy tanks [5]), currently this is not always feasible.

The use of SOFI with the configurations shown in Subfig. 2.13b, Subfig. 2.13c, and Subfig. 2.13d are potentially advantageous where system components (such as cryogenic centrifugal pump, heat exchangers, Joule-Thomson valves, cryogenic cut-off valves, temperature sensors, pressure sensors, flow rate meters, exhaust valves) demonstrate higher reliability and higher potential operating cycle numbers compared to relief valves. Otherwise, vacuum layers and MLI stand as the optimal solutions for the configuration without TVS (Subfig. 2.13a), albeit their drawbacks will be highlighted in subsection 4.2.4.

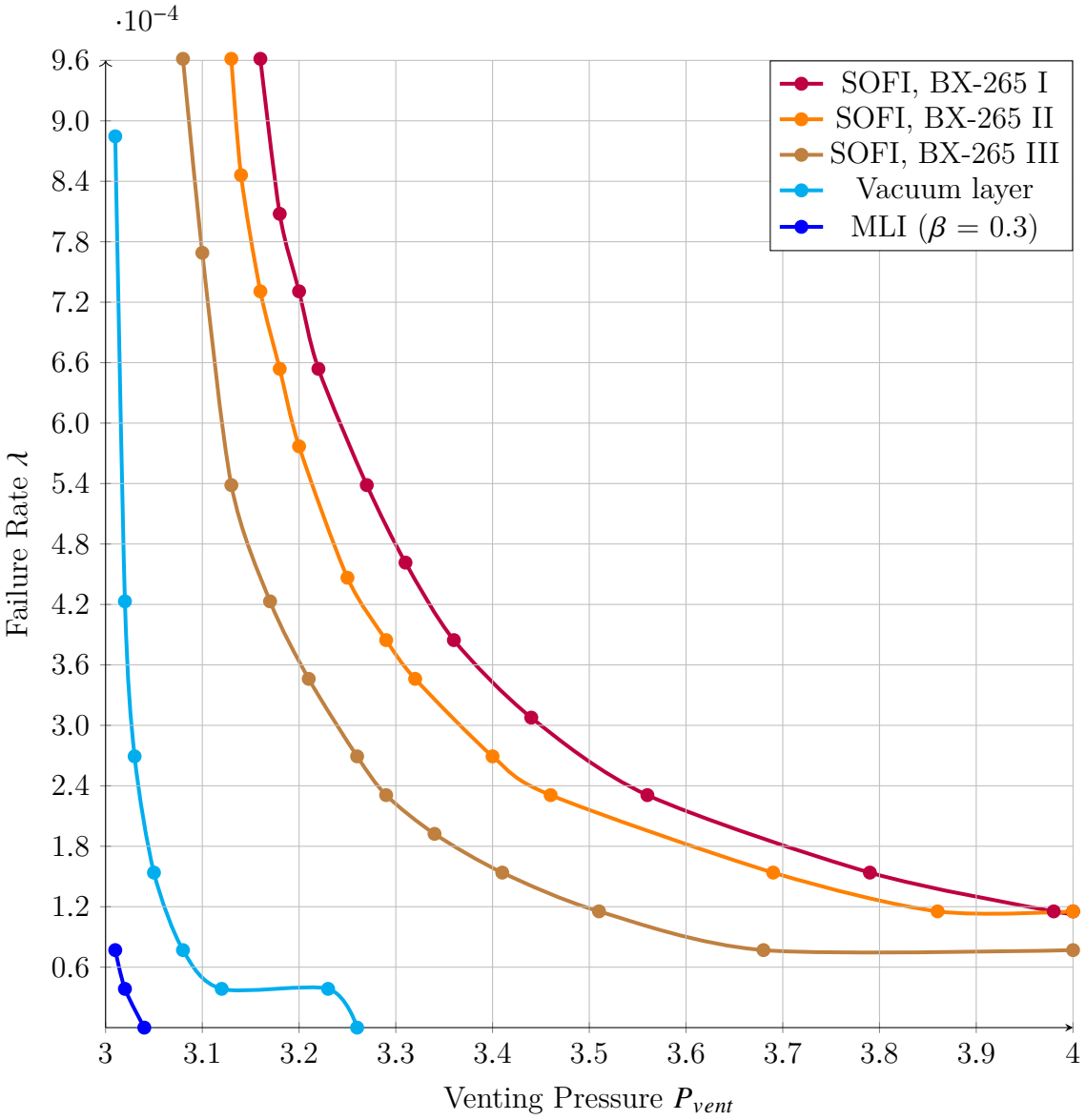

Figure 4.11 Influence of the venting pressure on the failure rate of relief valves.

4.2.3 Effect of environmental factors on the lifespan of relief valves

To evaluate the impact of external temperature on the evaporation of liquid hydrogen, various conditions were considered as references, from optimal to the most extreme. According to [5], the most demanding time for tank insulation is when the aircraft is parked with a full tank (but as demonstrated in this study, the lower filling level, the higher evaporation of liquid hydrogen) before takeoff in a hot desert, where ambient temperatures can reach 51°C. Tab. 4.16 summarizes all the data considered for the analysis. The core algorithm for this computational analysis is detailed in the appendix (function 1 and 4).

Table 4.16 Summary of data for computational analysis concerning the influence of environmental factors on the failure rate of relief valves.

Category	**Parameter**	**Value**	**Unit**	**Remark**
Insulation performance	Thermal conductivity	18.9×10^{-3}	$\frac{W}{mK}$	SOFI BX-265 [33]
	Total thermal resistance	0.19	$\frac{W}{K}$	Eq. 3.38
Climatic Conditions	Temperatures from 9 p.m. to 10 a.m.	27 – 33	°C	21/07/2022 Napoli Airport [56]
		6 – 8	°C	1/1/24 Hamburg Airport [56]
		−35 – −33	°C	2/1/24 Kuusano Airport [56]
		Fixed at 51	°C	[5]
Operating Conditions	Average overnight stand time[1]	13	hours	
	Operating pressure	3	bar	
	Venting pressure	3.20 – 3.40	bar	
	Filling level	92	%	
	Tank Volume	25.9*	m^3	Tab. 3.5

[1] Airbus A320-214, China Express Airlines; * Cylindrical tank

In Fig. 4.12, it can be asserted that at the same venting pressure, the activation of relief valves increases with rising external temperatures, thereby increasing the failure rate.

Furthermore, considering a humidity level of 80% (and thus accounting for a safety factor of 1.1), at the same venting pressure and external temperature, the failure rate curve is slightly shifted upwards: this implies that in the presence of extreme humidity, to maintain the same failure rate, it is necessary to reduce the venting pressure by a few kPa.

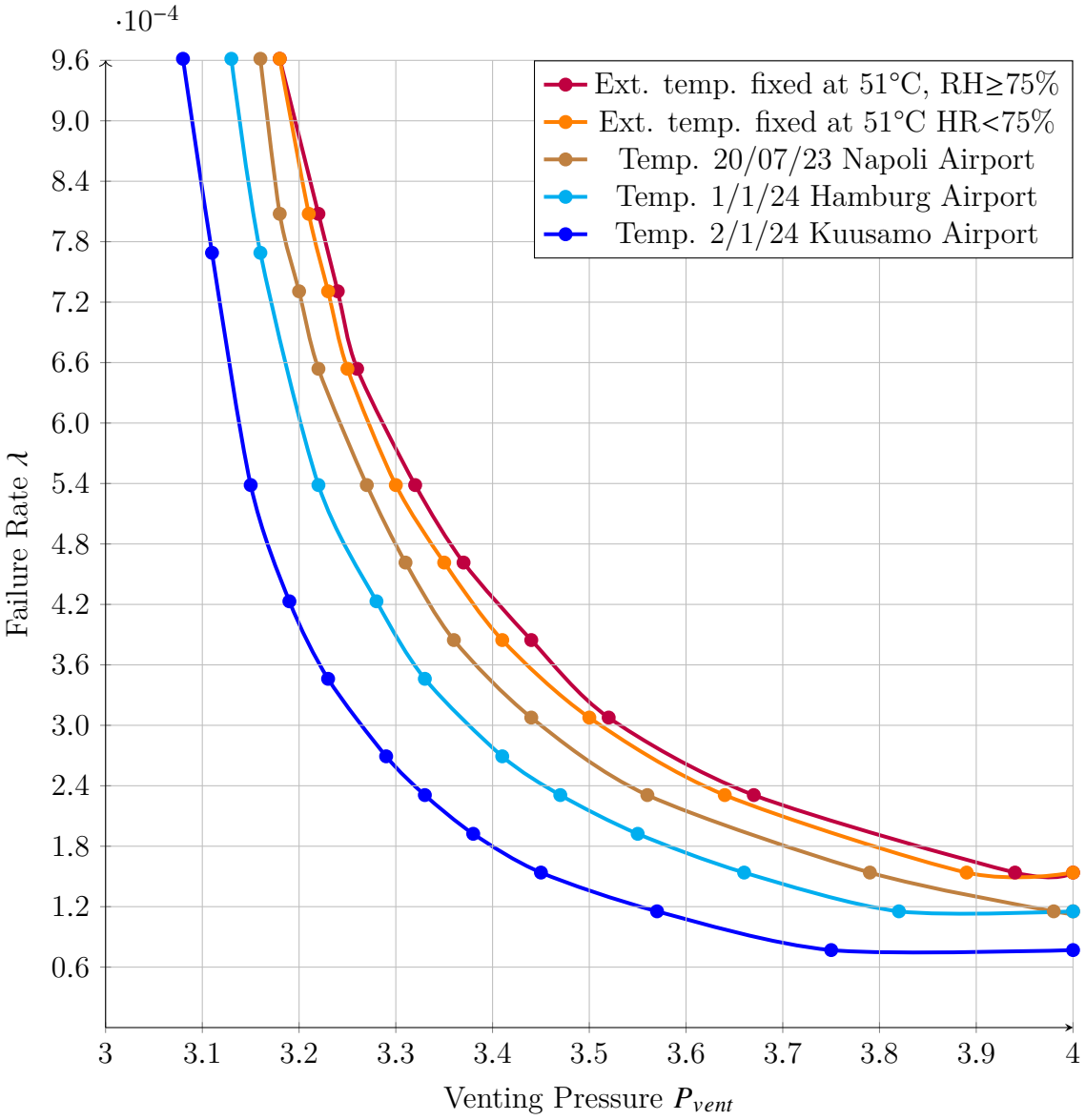

Figure 4.12 Influence of the environmental factors on the relief valves failure rates for a cryogenic tank with SOFI.

Through computational analysis, it has been possible to observe how cryogenic tanks insulated with SOFI are highly sensitive to variations in climatic conditions; indeed, for the same venting pressure of P = 3.3 bar, transitioning from the climatic conditions of Kuusamo airport to those of Naples airport, the failure rate doubles.

Considering the same conditions as described in Tab. 4.16, but with a vacuum layer having a thermal conductivity of k = 8 $\times 10^{-4}$ $\frac{W}{mK}$, the graph illustrated in Fig. 4.13 is obtained.

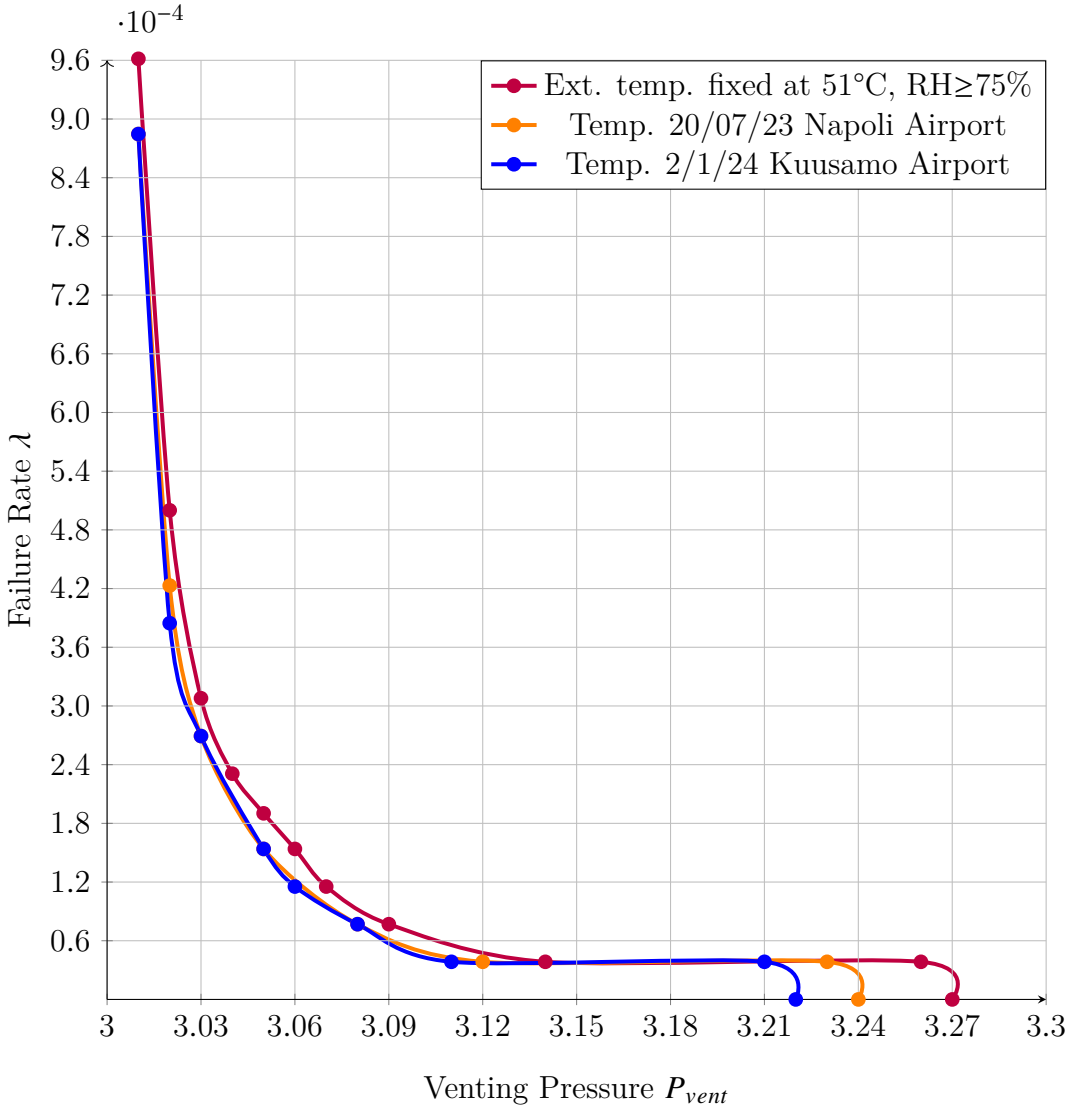

Figure 4.13 Influence of the environmental factors on the relief valves failure rates for a cryogenic tank with a vacuum layer insulation.

The figure demonstrates the effectiveness of the vacuum layer system insulation. In fact, transitioning from an average temperature of -35°C to a temperature of 51°C with 80% relative humidity, the trend of the failure rate remains nearly the same. If the valve were not subject to wear and aging, when transitioning from an external temperature of -35°C to 51°C (RH 80%), the venting pressures of 3.27 bar, 3.24 bar, and 3.22 bar would be sufficient to achieve an infinite service life.

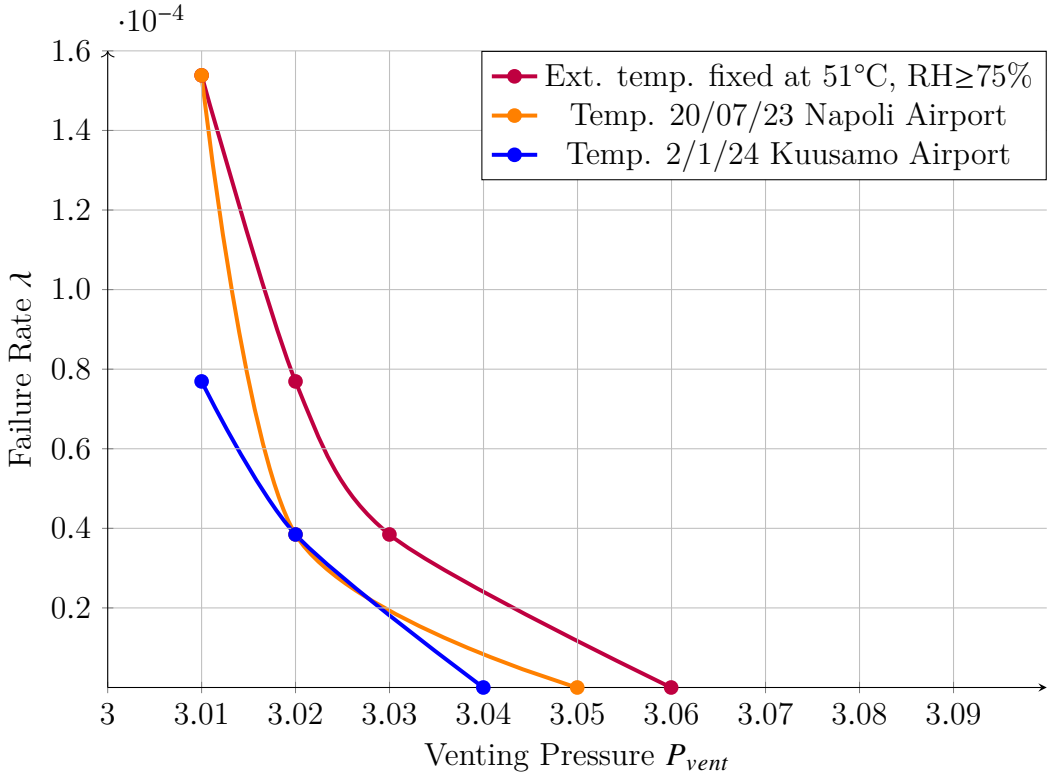

Figure 4.14 Influence of environmental factors on the failure fates of relief valves for a cryogenic tank equipped with MLI and a filling level of 50%.

Considering a MLI with a thermal conductivity k = 2.5×10^{-5} [141], it is possible to achieve an infinite service life (again disregarding aging and wear) with even lower venting pressures, demonstrating the superior effectiveness of these insulating materials. Thus, this results once again into reduced thermal stratification within the cryogenic tank and lower gas temperatures within the ullage.

Through Fig. 4.14, it has been found that the increase in external temperature does not have a significant effect on the functionality of relief valves and the other thermodynamic venting system components. Thus, environmental factors such as temperature and humidity become increasingly significant with the increase in thermal conductivity k of the insulation and the reduction in insulation thickness, thereby reducing the total thermal resistance.

From this analysis, it is clear that in a design where the cryogenic tank is insulated with SOFI, the operation of the relief valves depends heavily on atmospheric conditions. On the other hand, tanks insulated with MLI are not affected by changes in external temperature, thus enhancing the service life of the relief valves and the cryogenic tank itself. Having demonstrated that the failure rates for components of a cryogenic system depend strongly on various operating conditions, degradation indices could be assigned once it becomes possible to evaluate the impact of thermal stratification and thermal gradients in the tank. Therefore, once the optimal operating conditions for the tank have

been calculated, thanks to this study, it will be possible to calculate the failure rates of the components that are part of the TVS. However, assuming a venting pressure of 3.1 bar, when switching from a design with SOFI to one with MLI, the failure rate shifts from a λ proportional to 10^{-2} to a λ proportional to 10^{-5}. From these data, through the formula 3.6, a $f(x)= 0.9$ is obtained, thus a degradation index of $I = 4.5$. Therefore, switching from an MLI to a SOFI, the service life of the relief valves is reduced by 90%.

In addition, moving from an average external temperature of -35°C to an average external temperature of 51°C, the failure rate changes from a value of 2.69 10^{-4} to 5.76 10^{-4}. Through the formula 3.6, a $f(x) = 0.53$ is obtained, thus indicating a maximum degradation index of $I = 2.65$. On the other hand for MLI, the maximum degradation index is practically negligible.

4.2.4 Effect of degraded insulation on relief valves performance

To assess the impact of SOFI degradation on the performance of relief valves, reference was made to Fig. 2.9, in which the insulating material shows an increase in thermal conductivity k from 18.6 $\times 10^{-3} \frac{W}{mK}$ to 28.3 $\times 10^{-3} \frac{W}{mK}$ over two years. For this analysis, the conditions listed in Table4.17 were used. The core algorithm for this computational analysis is detailed in the appendix (function 5).

Table 4.17 Summary of data for the computational analysis to calculate the influence of insulation degradation on the failure rate of relief valves.

Category	Parameter	Value	Unit	Remark
Insulation performance	Thermal conductivity	18.6 – 28.3 $\times 10^{-3}$	$\frac{W}{mK}$	SOFI BX-265 Fig.2.9
		35 $\times 10^{-3}$	$\frac{W}{mK}$	MLI with degraded vacuum [30]
	Total thermal resistance	0.19 – 0.12	$\frac{W}{K}$	Eq. 3.38
		0.09	$\frac{W}{K}$	Eq. 3.38
Climatic Conditions	Temperatures from 9 p.m. to 10 a.m.	27 – 33	°C	21/07/2022 Napoli Airport [56]
	Temperatures	6 – 8	°C	1/1/24 Hamburg Airport [56]
	Temperatures	−35 – −33	°C	2/1/24 Kuusano Airport [56]
	Temperatures	Fixed at 51	°C	[5]
Operating Conditions	Average overnight stand time[1]	13	hours	
	Operating pressure	3.00	bar	
	Venting pressure	3.01 – 3.04	bar	
	Filling level	92	%	
	Tank Volume	25.90*	m^3	Tab. 3.5

[1] Airbus A320-214, China Express Airlines; ∗ Cylindrical tank

After two years of operation, from Fig. 4.15, it is observable that SOFI requires a higher venting pressure to maintain the same failure rate. From Fig. 4.16, after two years of

operation, the failure rate curve increases with a greater slope at higher temperatures, once again highlighting the greater susceptibility of SOFI to environmental factors. Considering an average external temperature of 30°C, after two years of operation with SOFI, the relief valves would move from about 13 activations per day to 16 activations per day, shifting from a lifespan of 2000 operating hours to 1625 hours, thus a reduction of 18.75%.

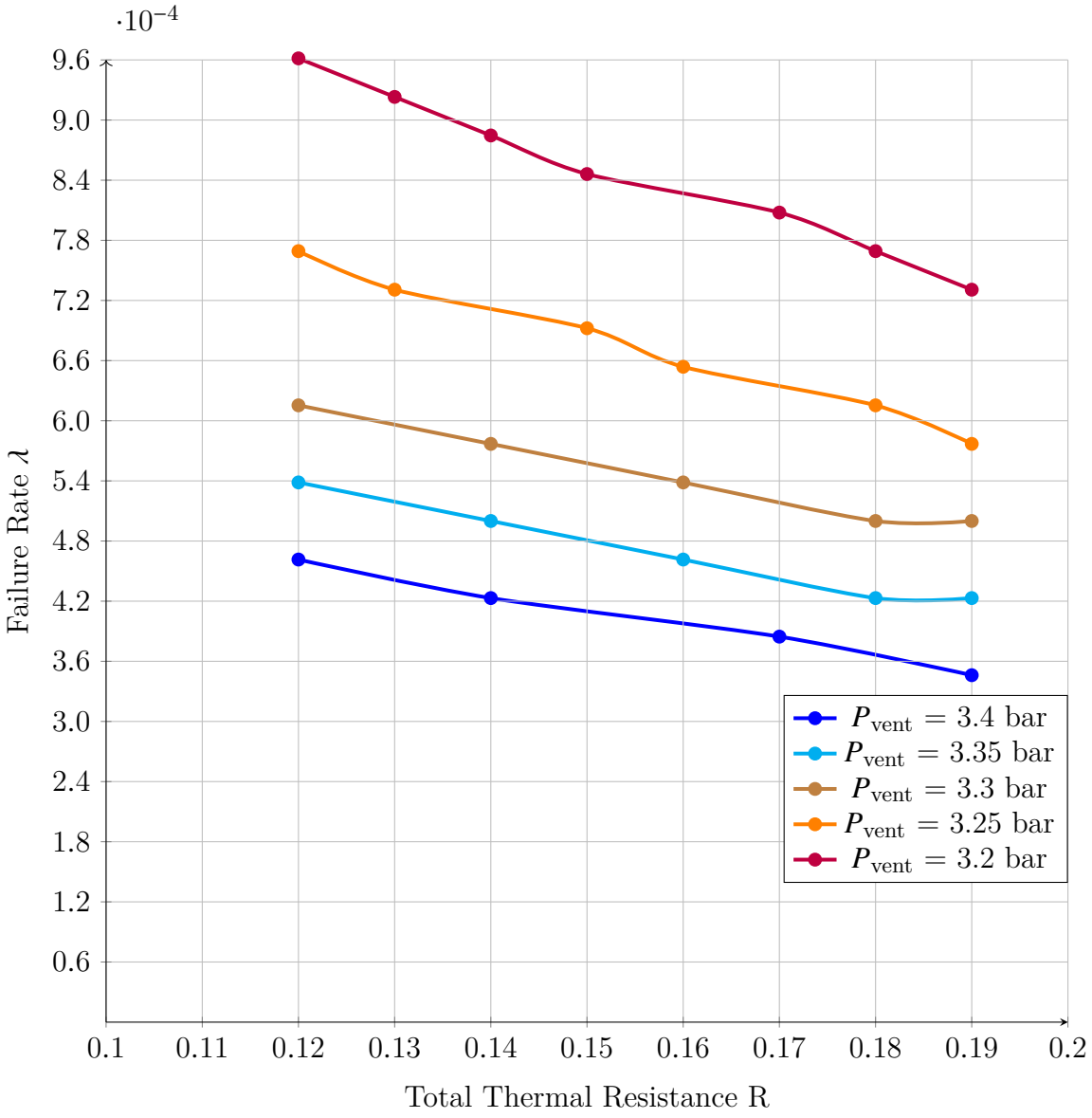

Figure 4.15 Impact of the SOFI degradation on the relief valves performance over time for various venting pressure and for climatic conditions at Napoli Airport.

Fig. 4.17 illustrates the effect of vacuum state degradation in MLI compared to the degradation of SOFI after two years of operation. From the figure, it is clear that the probable loss of vacuum has a greater impact compared to the degradation of SOFI after years of operation. However, this difference is not very marked. Nevertheless, a SOFI needs about

2 years to degrade if subjected to extreme climatic conditions, which may be avoided by following the strategies outlined in Table 4.6. On the other hand, the causes of vacuum state degradation are still unknown, necessitating the analysis of thermal cycles and vibrations on the vacuum state to understand how all system components and joints can cause vacuum loss. However, from this analysis, it is evident that although SOFIs are less performant, they are more reliable; thus, to avoid consequences due to the loss of vacuum state, a configuration with a vacuum layer and SOFI in series could be considered.

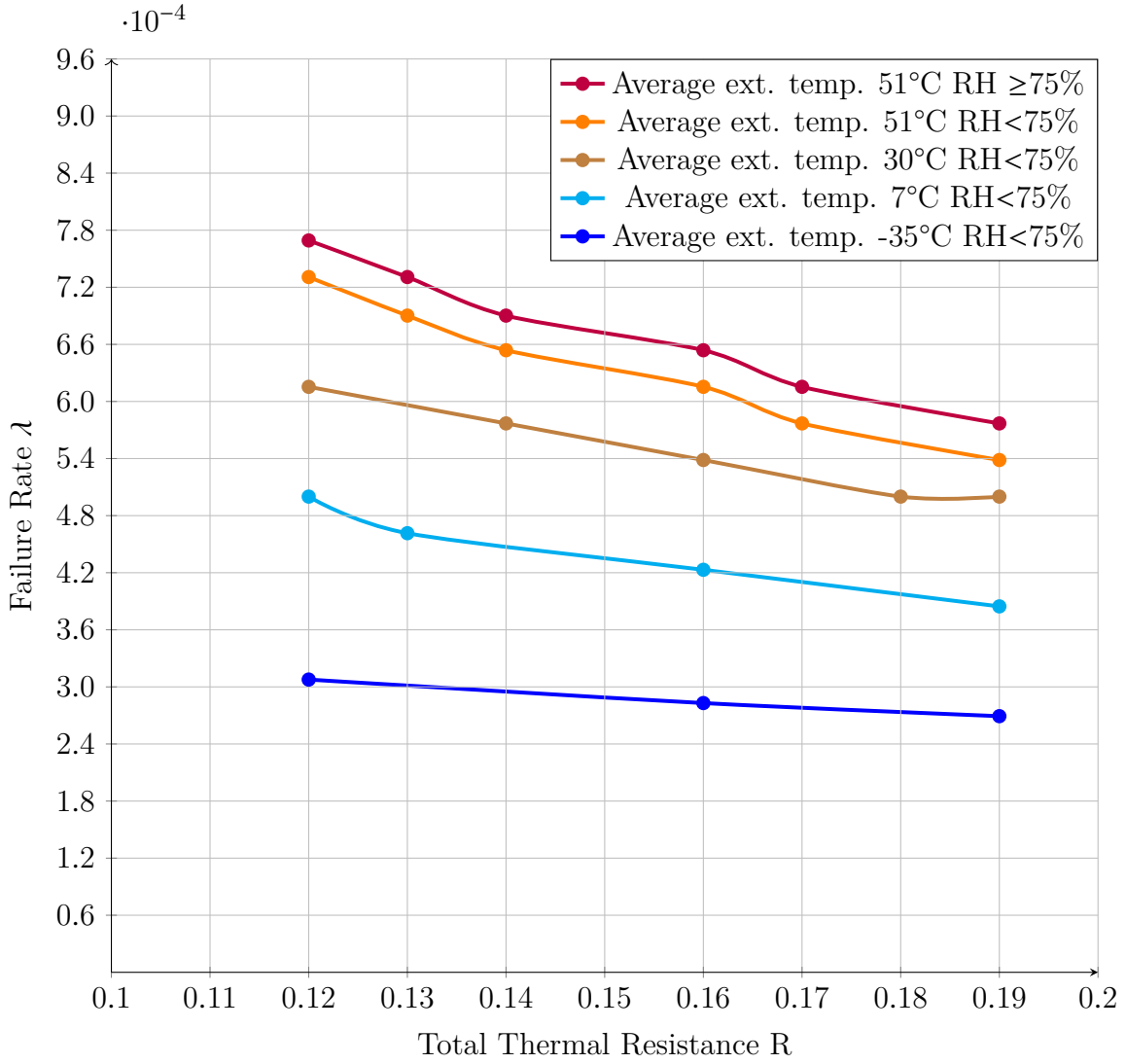

Figure 4.16 Impact of the SOFI degradation on the relief valves performance over time for various environmental factors with a venting pressure of 3.3 bar.

Furthermore, the code developed for this analysis has proven to be versatile and could be applied to all types of insulation and geometries. Therefore, once the degradation behaviors of an MLI and other insulations are analyzed in the laboratory, this study could be considered to evaluate the impact of such degradation on the relief valves and all components of the TVS.

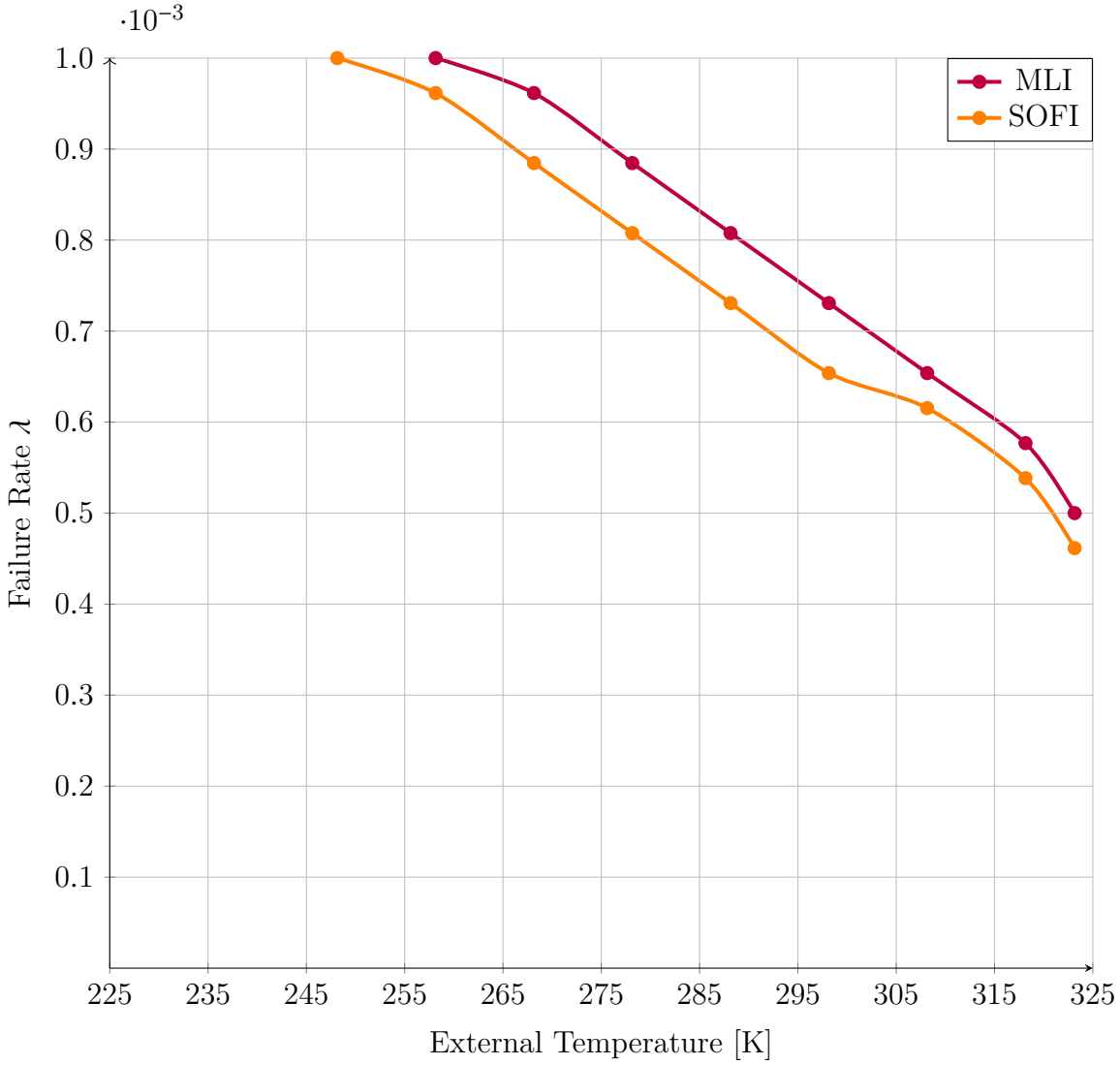

Figure 4.17 Impact of the loss of the vacuum state of an MLI on the performance of the relief valves with a venting pressure of 3.3 bar and an average external temperature of 30°C.

4.3 Architecture solutions: allocating components within aircraft

From the results illustrated in Section 4.1 and Section 4.2, it seems evident that the best possible configuration entails allocating all components within the fuselage, as they would be subjected to lower levels of vibration with the possibility of controlling temperature and humidity levels. However, for better distribution of the weight of the components and for balance reasons, it is not feasible to place all components within the fuselage of an aircraft used for long-haul flights [5]. For this reason, the probable allocation of components will be analyzed with the constraint of locating at least one component (between fuel cells and liquid hydrogen tanks) in underwing nacelles.

Regarding Type III and IV tanks, from the analyses conducted, Type IV tanks show a greater fatigue life in every scenario. However, given the unknown behavior regarding hydrogen permeation and the actual effect of hydrogen temperature on the polymeric liner, the choice of tank type was made with reference to the tank's intrinsic behavior under climatic conditions: thus, if at high temperatures the lifespan of Type IV tanks decreases but is still longer than that of Type III tanks, Type III tanks are preferred. Tab. 4.18 analyzes the probable allocation of components and the worst operational scenario. However, the table below only takes into account environmental factors, as operational conditions do not influence the allocation of components, except for the complexity of the resulting system. For example, placing fuel cells inside the fuselage would add complexity to the system, increasing the distances among powertrain components such as cooling systems and the electrical system [108].

Referring to the ATDI delineated in Equation 3.5, in all conceivable scenarios, the configuration that envisions allocating components within the nacelles attached to the aircraft's wings exhibits a higher ATDI. This is because, in this configuration, it is not possible to control the effects of ambient temperature on the components; for example, fuel cells exhibit a degradation index $I = 5$ when subjected to subzero temperatures. In light of this, Tab. 4.19 presents various configurations with the best possible configuration and the optimal choice of materials for Type III and IV tanks, and insulations for cryogenic tanks (MLI is always superior, but where temperatures are consistently subzero, the introduction of SOFI would ensure greater safety and weight savings). Among the suggested configurations, in the case of using SOFI, the use of spherical tanks is advisable (Subfig. 2.1b), due to their better performance in limiting the evaporation of liquid hydrogen.

The proposed configurations aim to enhance the average lifespan of the components. However, in each configuration, when fuel cells are required to operate in environments with subzero temperatures, air conditioning systems and the strategies outlined in Tab. 4.13 become mandatory, at least with respect to the current range of available data. In cases involving the use of tanks that store gaseous hydrogen, in operational scenarios that entail

Table 4.18 Allocation of the compontens within the aircraft analyzing the worst scenario in terms of temperature of the surroundings.

Component	**Location**	**Increase in the failure rate % λ in the worst scenario**	**Description**
Fuel cell	Fuselage	Asymptotic failure rate, imminent component failure	In case of sub-zero temperatures without an air-conditioning system
	Nacelles	Asymptotic failure rate, imminent component failure	In case of sub-zero temperatures
Type III tank	Fuselage	56 %	In case of sub-zero temperatures below -20°C
Type IV tank	Fuselage	5.1 %	In case of temperatures above 40°C
Cryogenic tank isolated with SOFI	Fuselage	Failure rate is expected to increase	In case of temperatures above 40°C the SOFI would not allow limiting thermal stratification in the tank
	Linked between wing and tail (TTB)	A greater increase in the failure rate is expected	The cryogenic tank would be subjected to worse weather conditions and worse vibration loads
Relief valves*	Fuselage	107 % **	SOFI is very susceptible to extreme temperatures and humidity
	Linked between wing and tail (TTB)	Failure rate is expected to increase	The cryogenic tank would be subjected to worse weather conditions and vibrations, increasing the work of the valves and the cooling system. In the case of insulation with MLI, the effect of vibrations on the vacuum state is still unknown

* Constrained to the allocation of cryogenic tanks; ** If the cryogenic tank is insulated with SOFI

Table 4.19 Configuration and choice of optimal design considering different average external temperatures over the year.

Temperature °C	**Configuration (Subfig.)**		**Allocation**	**Components**
≥ 40	2.1b[3] 2.1c[3,4]	2.1d[4]	Fuselage	Type III tank
				Cryogenic Tanks[2]
			Nacelles	Fuel Cells
40 < T < 0	2.1b[3] 2.1c[3,4]	2.1d[4]	Fuselage	Type IV tank
				Cryogenic Tanks[2]
			Nacelles	Fuel Cells
≤0	2.1e[4]		Fuselage[5]	Type IV tank
				Fuel Cells
			Linked between wing and tail (TTB configuration)	Cryogenic Tanks[1]

[1] Possibility of considering a SOFI for the cryogenic tank
[2] Cryogenic Tank with MLI
[3] Configuration for spherical tank
[4] Configuration for cylindrical tank
[5] Temperature control required to avoid sub-zero temperatures

extreme temperatures, the introduction of Type IV tanks (which are lighter) through the use of air conditioning systems could be considered.

5 Conclusion and Outlook

Contrary to conventional aircraft, with the deployment of hydrogen-powered aircraft, failure rates have a significant dependency on thermodynamic parameters, operating conditions, environmental factors, tank design and type of insulation used. Thus, thanks to the results presented, within hydrogen aviation, it is possible to assert that failure rates are highly versatile. Consequently, the failure rates presented in Subsection 2.6.4 (extrapolated from the available literature) related to tanks and valves used in cryogenic applications should be reconsidered and, most importantly, further investigated.

Within this study, the first research question presented in Subsection 1.3 has been extensively investigated. This study has thoroughly examined the impact of operating conditions and environmental factors on the degradation of critical components in hydrogen-powered aircraft.

The deterioration of hydrogen storage systems, encompassing both gaseous and liquid states, is profoundly influenced by a multitude of operational and environmental parameters. These include fluctuations in temperature and humidity, alterations in pressure, changes in the operating temperature of hydrogen, the phenomenon of hydrogen embrittlement, hydrogen permeation, as well as exposure to vibrations. Such factors play a crucial role in determining the longevity and reliability of hydrogen tanks.

Thanks to the methodology developed in this study, it was possible to address the second and third research questions outlined in Subsection 1.3. Specifically, in Chapter 3, a calculation procedure was established to assess the effects of various operating conditions and environmental factors on component degradation and, consequently, their failure rates. The methodology devised can be applied not only to all components of a hydrogen-powered aircraft but also, due to its versatility, to any system or component (such us the batteries of electrically powered aircraft, gas turbines, etc). Moreover, the additional maintenance efforts required in terms of failure rates were calculated, addressing the fourth research question. The results have been thoroughly discussed in Chapter 4. Thanks to the developed methodology, it was possible to calculate how variations in the intrinsic state of the considered operating condition or environmental factor can increase or decrease the failure rate, thereby influencing maintenance efforts.

This study has demonstrated that the hydraulic tests suggested by Standards are insufficient to demonstrate the efficacy and ensure the safety of hydrogen storage tanks. The establishment of new standards that consider the impact of the hydrogen environment is unequivocally mandatory. Moreover, having demonstrated that the temperature

cycles, thermal gradients, thermal stratifications, and pressure cycles that occur in the tank strongly depend on operational conditions, the failure rates present in the literature concerning liquid hydrogen tanks cannot be taken as a reference, except for approximate suppositions. Particularly for liquid hydrogen tanks subjected to continuous cycles of filling, emptying, and heating, failure rates need reevaluation. However, this study highlighted that maintaining a constant level of liquid hydrogen may improve the lifespan of both the tank itself and the components that are part of the ventilation system (TVS).

The performance of cryogenic valves is essential for the safety of hydrogen supply and storage system, requiring careful maintenance and frequent monitoring of degradation conditions. In addressing to the fourth research question, it has been determined that the performance of relief valves is significantly impacted by the rate of hydrogen evaporation, as well as by various operational conditions of the tank and system design. These conditions include the filling level, operating pressure, venting pressure, type of insulation, geometry of the tank and other parameters. This insight is crucial for optimizing the design and operation of hydrogen storage facilities, thereby enhancing their safety and efficiency. This study has shown that, switching from an MLI to a SOFI, the maintenance efforts related to the components of the thermodynamic ventilation system would increase, as SOFIs are super sensitive to climatic and operational conditions. The study shows that when transitioning from an MLI to a SOFI design, the lifespan of relief valves is reduced by 90%. Nevertheless, SOFIs would guarantee greater safety due to the system's lesser complexity and predictable, non-catastrophic degradation.

Despite significant advancements, some critical challenges remain that require further investigation. Firstly, developing more sophisticated models that can accurately predict the degradation of components under diversified operational scenarios is essential for optimizing maintenance and enhancing operational safety. In the delicate case of liquid hydrogen tanks, the research world must answer many questions, for example: given the operation of the tank at a working pressure, how far can we go with the venting pressure so that the tank is not affected by thermal gradients and stratification and by the cycles of pressure itself? What are the effects of the hydrogen environment on the liner of the tanks over a prolonged period? To answer these questions, laboratory tests and FEM analysis are necessary.

Furthermore, concerning liquid hydrogen tanks, the engine-induced vibrations and the effect of the hydrogen environment need to be studied thoroughly. In addition, the effects of vibrations, thermal cycles, and humidity on the outer wall of the tank must be investigated to assess the probable impact on MLIs, to avoid losing the vacuum state.

Regarding fuel cells, the study identified literature gaps needing further investigation; notably, natural failure rates do not align with those from laboratory test results discussed here. Concerning vibrations, laboratory tests with higher GRMS are mandatory. In addition, subzero temperatures have a destructive impact on fuel cell degradation. Since these systems are must operate in harsh conditions, this topic requires thorough investigation and research effort to improve the behavior of fuel cells at subzero temperatures and settle the differing opinions on the subject.

Research on new materials offering greater resistance to degradation under extreme environmental conditions could lead to significant improvements in the durability of components for hydrogen aircraft. In conclusion, addressing the final research question underscores that the transition towards sustainable aviation unequivocally requires a robust commitment to research and development. Future efforts should focus on addressing the remaining challenges and investigating the effects of long-term operational conditions. Finally, exploring new architectures combining batteries, fuel cells, and gas turbines could be a turning point.

Appendix

Algorithm 1 Calculation of tank outer wall temperature, incoming heat flow and mass of liquid hydrogen evaporated

function THERMODYNAMICVALUES($T_{s,new}(t), M(t), Q_{out}(t), h(t)$)
  Initialization $T_s(i)$, mi, c, Kg, R, T_{LH2}, e, σ, g, D, A,
m_{H2}, max_iter, tolerance, $t[0:1:46800]$ ▷ *Set initial values discussed in Section 3.2 and Section 3.3*
  $T_{oo}(t)$ ▷ *Incorporation of external temperature by calling the function 2*
  for each $i \in t[0:1:46800]$ **do**
    while iter < max_iter **do** ▷ *Set an iteration process with a maximum number of iterations*
      Calculate $\alpha, \nu, Pr, R_{AD}, N_{UD}, h$ ▷ *By using Equations 3.12 (or 3.13), 3.14, 3.15, 3.16, 3.17 and 3.11*
      return $T_{s,new}(t), h(t)$ ▷ *Return tank outer wall temperature and thermal convection coefficient in their respective arrays by using Equations 3.18 and 3.11*
      if $T_{s,new}$ does not converge **then**
        Update $T_s(i)$ and continue iteration.
      end if
      if error < tolerance **then** ▷ *Check if the relative error is less than the tolerance*
        Save $T_{s,new}(t)$ **break**
      else
        Update $T_s(i)$ for the next iteration.
      end if
    end while
    return $M(t), Q_{out}(t)$ ▷ *Return incoming heat flow and mass of liquid hydrogen evaporated any second in their respective arrays by using Equations 3.19 and 3.20*
  end for each
end function

Algorithm 2 External Temperature Function

function EXTERNALTEMPERATURE($T_{oo}(t)$)
  Initialization $t[0:1:46800]$, T_{oo} ▷ *Time interval and external temperature*
  return $T_{oo}(t)$ ▷ *Return external temperature as a function of time*
end function

Algorithm 3 Calculation of failure rates for different filling levels

function FAILURERATES($\lambda(\beta)$, $\frac{dP}{dt}(\beta, t)$)
  Initialization M(t), Q_{out}(t), $\beta(\phi_i)$, P_i, V, $t[0:1:46800]$, $P_{venting}$
  for each $j \in \phi(\beta, \rho, P_i)$ **do** ▷ *Calculates the opening and closing cycles of the relief valves for each different value of ϕ, using Fig. 3.5 and the Equations 3.25 and 3.26*
    for each $i \in t[0:1:46800]$ **do**
      if i == 1 **then**
        $P2(i) = P_i$
      else
        Calculate $\frac{dP}{dt}$ over time ▷ *By using Equation 3.27*
        if $P2(i) \geq P_{venting}$ **then**
          $P2(i) = P_i$ ▷ *Reset pressure; increment relief valve opening counter*
        end if
      end if
    end for each
    return N_{CD} ▷ *Number of opening-closing cycles of relief valves in the time interval considered*
  end for each
  return ENY, MTBF, λ ▷ *By using Equations 3.28, 3.29 and 2.6*
end function

Algorithm 4 Calculation of failure rates for different venting pressures

function FAILURERATES($\lambda(P_{venting})$, $\frac{dP}{dt}(P_{venting}, t)$)
  Initialization M(t), Q_{out}(t), $\beta(\phi_i)$, P_i, V, $t[0:1:46800]$, $P_{venting}$
  for each $j \in P_{venting}$ **do** ▷ *Calculates the opening and closing cycles of the relief valves for each different value of $P_{venting}$*
    for each $i \in t[0:1:46800]$ **do**
      if i == 1 **then**
        $P2(i) = P_i$
      else
        Calculate $\frac{dP}{dt}$ over time ▷ *By using Equation 3.27*
        if $P2(i) \geq P_{venting}$ **then**
          $P2(i) = P_i$ ▷ *Reset pressure; increment relief valve opening counter*
        end if
      end if
    end for each
    return N_{CD} ▷ *Number of opening-closing cycles of relief valves in the time interval considered*
  end for each
  return ENY, MTBF, λ ▷ *By using Equations 3.28, 3.29 and 2.6*
end function

Algorithm 5 Calculation of the effect of insulation degradation on the failure rate of relief valves and TVS components

function FAILURERATES($\lambda(R)$, $\frac{dP}{dt}(R, t)$)
  Initialization $T_s(i), mi, c, Kg, R, T_{LH2}, e, \sigma, g, D, A,$
$m_{H2}, max\_iter, tolerance, t[0:1:46800]$ ▷ *Set initial values discussed in Section 3.2 and Section 3.3*
  $T_{oo}(t)$ ▷ *Incorporation of external temperature by calling the function 2*
  for each $j \in R$ **do** ▷ *The range of R is contingent upon the specific case under analysis. The code provided can be utilized to simulate the degradation of the insulation over time, by adjusting R from its optimal value to a scenario representing the absence of insulation.*
    for each $i \in t[0:1:46800]$ **do**
      while iter < max_iter **do** ▷ *Set an iteration process with a maximum number of iterations*
        Calculate $\alpha, v, Pr, R_{AD}, N_{UD}, h$ ▷ *By using Equations 3.12 (or 3.13), 3.14, 3.15, 3.16, 3.17 and 3.11*
        return $T_{s,new}(t), h(t)$ ▷ *Return tank outer wall temperature and thermal convection coefficient in their respective arrays by using Equations 3.18 and 3.11*
        if $T_{s,new}$ does not converge **then**
          Update $T_s(i)$ and continue iteration.
        end if
        if error < tolerance **then** ▷ *Check if the relative error is less than the tolerance*
          Save $T_{s,new}(t)$ **break**
        else
          Update $T_s(i)$ for the next iteration.
        end if
      end while
      return $Q_{out}(R)$ ▷ *Return incoming heat flow for any value of R by using Equation 3.19*
    end for each
  end for each
  Initialization $M(t), Q_{out}(R), \beta(\phi_i), P_i, V, t[0:1:46800], P_{venting}$
  for each $i \in t[0:1:46800]$ **do**
    if $i == 1$ **then**
      $P2(i) = P_i$
    else
      Calculate $\frac{dP}{dt}$ over time ▷ *By using Equation 3.27*
      if $P2(i) \geq P_{venting}$ **then**
        $P2(i) = P_i$ ▷ *Reset pressure; increment relief valve opening counter*
      end if
    end if
    return N_{CD} ▷ *Number of opening-closing cycles of relief valves in the time interval considered*
  end for each
  return ENY, MTBF, λ ▷ *By using Equations 3.28, 3.29 and 2.6*
end function

Bibliography

[1] A. Abu Kasim, M. Chan, and E. J. Marek. "Performance and failure analysis of a retrofitted Cessna aircraft with a Fuel Cell Power System fuelled with liquid hydrogen." In: *Journal of Power Sources* 521 (2022), p. 230987. ISSN: 03787753. DOI: 10.1016/j.jpowsour.2022.230987.

[2] G. Abumeri, D. Kosareo, and J. Roche. "Cryogenic Composite Tank Design for Next Generation Launch Technology." In: *40th AIAA/ASME/SAE/ASEE Joint Propulsion Conference and Exhibit*. Reston, Virigina: American Institute of Aeronautics and Astronautics, 2004. ISBN: 978-1-62410-037-6. DOI: 10.2514/6.2004-3390.

[3] S. M. Aceves, J. Martinez-Frias, and F. Espinosa-Loza. "Performance Evaluation tests of insulated pressure vessels for vehicular hydrogen storage." In: *U.S. Department of Energy* 14th World Hydrogen Energy Conference (2002).

[4] S. Acevesa, J. Martinez Friasb, and O. Garcia Villazana. "Analytical and experimental evaluation of insulated pressure vessels for cryogenic hydrogen storage." In: *International Journal of Hydrogen Energy 25* (2000), pp. 1075–1085.

[5] E. J. Adler and Martins, Joaquim R. R. A. "Hydrogen-Powered Aircraft: Fundamental Concepts, Key Technologies, and Environmental Impacts." In: *Progress in Aerospace Sciences (2023)* (2023).

[6] T. T. Aindow and J. O'Neill. "Use of mechanical tests to predict durability of polymer fuel cell membranes under humidity cycling." In: *Journal of Power Sources* 196.8 (2011), pp. 3851–3854. ISSN: 03787753. DOI: 10.1016/j.jpowsour.2010.12.031.

[7] AIRBUS. *A320ceo: Setting single-aisle standards*. URL: https://aircraft.airbus.com/en/aircraft/a320-the-most-successful-aircraft-family-ever/a320ceo (visited on 03/14/2024).

[8] R. Alink, D. Gerteisen, and M. Oszcipok. "Degradation effects in polymer electrolyte membrane fuel cell stacks by sub-zero operation—An in situ and ex situ analysis." In: *Journal of Power Sources* 182.1 (2008), pp. 175–187. ISSN: 03787753. DOI: 10.1016/j.jpowsour.2008.03.074.

[9] R. Banan, A. Bazylak, and J. Zu. "Combined effects of environmental vibrations and hygrothermal fatigue on mechanical damage in PEM fuel cells." In: *International Journal of Hydrogen Energy* 40.4 (2015), pp. 1911–1922. ISSN: 03603199. DOI: 10.1016/j.ijhydene.2014.11.125.

[10] R. Banan, A. Bazylak, and J. Zu. "Effect of mechanical vibrations on damage propagation in polymer electrolyte membrane fuel cells." In: *International Journal of Hydrogen Energy* 38.34 (2013), pp. 14764–14772. ISSN: 03603199. DOI: 10.1016/j.ijhydene.2013.08.136.

[11] A. Baroutaji et al. "Comprehensive investigation on hydrogen and fuel cell technology in the aviation and aerospace sectors." In: *Renewable and Sustainable Energy Reviews* 106 (2019), pp. 31–40. ISSN: 13640321. DOI: 10.1016/j.rser.2019.02.022.

[12] A. Baroutaji et al. "Comprehensive investigation on hydrogen and fuel cell technology in the aviation and aerospace sectors." In: *Renewable and Sustainable Energy Reviews* 106 (2019), pp. 31–40. ISSN: 13640321. DOI: 10.1016/j.rser.2019.02.022.

[13] H. Barthelemy, M. Weber, and F. Barbier. "Hydrogen Storage: Recent Improvements and Industrial Perspectives." In: *International Journal of Hydrogen Energy* 42.11 (2017), pp. 7254–7262. ISSN: 03603199. DOI: 10.1016/j.ijhydene.2016.03.178.

[14] H. Barthélémy. "Hydrogen storage – Industrial prospectives." In: *International Journal of Hydrogen Energy* 37.22 (2012), pp. 17364–17372. ISSN: 03603199. DOI: 10.1016/j.ijhydene.2012.04.121.

[15] *Basic Requirements for Fully Wrapped Fiber Reinforced Aluminum Lined Cylinders*.

[16] U. Berardi. "The impact of aging and environmental conditions on the effective thermal conductivity of several foam materials." In: *Energy* 182 (2019), pp. 777–794. ISSN: 03605442. DOI: 10.1016/j.energy.2019.06.022.

[17] G. H. Bray, R. J. Bucci, and R. L. Brazill. "Lessons Neglected: Effects of Moist Air on Fatigue and Fatigue Crack Growth in Aluminum Alloys." In: *Materials Science Forum* 331-337 (2000), pp. 1413–1426. DOI: 10.4028/www.scientific.net/MSF.331-337.1413.

[18] G. D. Brewer. "Study of fuel systems for LH2-fueled subsonic transport aircraft." In: *Langley Research Center, National Aeronautics and Space Administration* I (1978).

[19] U. Cabulis et al. "Rigid Polyurethane Foams as External Tank Cryogenic Insulation for Space Launchers." In: *IOP Conference Series: Materials Science and Engineering* 500 (2019), p. 012009. ISSN: 1757-8981. DOI: 10.1088/1757-899X/500/1/012009.

[20] J. Chen, H. He, and H. Yue. "A review of plateau environmental adaptation for proton exchange membrane fuel cells." In: *International Journal of Hydrogen Energy* 50 (2024), pp. 744–764. ISSN: 03603199.

[21] Z. Chen, K. Tokaji, and A. Minagi. "Particle size dependence of fatigue crack propagation in SiC particulate-reinforced aluminium alloy composites." In: *JOURNAL OF MATERIALS SCIENCE* 36 (2001), pp. 4893–4902.

[22] E. Cho et al. "Characteristics of the PEMFC repetitively brought to temperatures below 0°C." In: *Journal of The Electrochemical* (2003). DOI: 10.1149/1.1621877.

[23] S. Collong and R. Kouta. "Fault tree analysis of proton exchange membrane fuel cell system safety." In: *International Journal of Hydrogen Energy* 40.25 (2015), pp. 8248–8260. ISSN: 03603199. DOI: 10.1016/j.ijhydene.2015.04.101.

[24] A. J. Colozza and L. Kohout. *Hydrogen Storage for Aircraft Applications Overview*. 2002.

[25] G. Cuccurullo and P. G. Berardi. *Elementi di Termodinamica e Trasmissione del Calore*. 1st ed. Salerno: cues, 2011. ISBN: 9788895028781.

[26] D. Di Maio, F. Magi, and I. A. Sever. "Damage Monitoring of Composite Components under Vibration Fatigue using Scanning Laser Doppler Vibrometer." In: *Experimental Mechanics* 58.3 (2018), pp. 499–514. ISSN: 0014-4851. DOI: 10.1007/s11340-017-0367-y.

[27] DIN Deutsches Institut für Normung e.V. *DIN EN 12245: Transportable Gas Cylinders - Fully Wrapped Composite Cylinders*. Berlin, 2002-02.

[28] DIN Deutsches Institut für Normung e.V. *DIN EN 13306: Instandhaltung – Begriffe der Instandhaltung; Dreisprachige Fassung EN 13306:2010*. Berlin, 2010.

[29] U. S. DOE. "Fuel Cell Technologies Program: Multi-Year Research, Development, and Demonstration Plan-Planned Program Activities for 2011-2020." In: *US Department of Energy* (2017).

[30] L. Edward and L. Filip. "Influence of vacuum level on insulation thermal performance for LNG cryogenic road tankers." In: *MATEC Web of Conferences* 240 (2018), p. 01019. DOI: 10.1051/matecconf/201824001019.

[31] Z. Fan et al. "Experimental Research on Vibration Fatigue of CFRP and Its Influence Factors Based on Vibration Testing." In: *Shock and Vibration* 2017 (2017), pp. 1–18. ISSN: 1070-9622. DOI: 10.1155/2017/1241623.

[32] J. E. Fesmire. "Vibration and Thermal Cycling Effects on Bulk-fill Insulation Materials for Cryogenic Tanks." In: *AIP Conference Proceedings*. AIP, 2006, pp. 1359–1366. DOI: 10.1063/1.2202556.

[33] J. E. Fesmire et al. "Spray-on foam insulations for launch vehicle cryogenic tanks." In: *Cryogenics* 52.4-6 (2012), pp. 251–261. ISSN: 00112275. DOI: 10.1016/j.cryogenics.2012.01.018.

[34] Flightradar24. *Production lists - Airbus A320 family*. URL: https://www.flightradar24.com/data/aircraft/a32s.

[35] J. Fydrych and G. Consogno. "A maintenance strategy for a multi-valve cryogenic distribution system." In: *IOP Conference Series: Materials Science and Engineering* 278 (2017), p. 012014. ISSN: 1757-8981. DOI: 10.1088/1757-899X/278/1/012014.

[36] B. Gentilleau, F. Touchard, and J. C. Grandidier. "Numerical study of influence of temperature and matrix cracking on type IV hydrogen high pressure storage vessel behavior." In: *Composite Structures* 111 (2014), pp. 98–110. ISSN: 02638223. DOI: 10.1016/j.compstruct.2013.12.034.

[37] Global Technical Regulation. *Proposal for a global technical regulation on hydrogen and fuel cell vehicles*. 2013.

[38] S. A. Grammatikos et al. "Thermal cycling effects on the durability of a pultruded GFRP material for off-shore civil engineering structures." In: *Composite Structures* 153 (2016), pp. 297–310. ISSN: 02638223. DOI: 10.1016/j.compstruct.2016.05.085.

[39] A. Haji Hosseinloo and M. M. Ehteshami. "Shock and vibration effects on performance reliability and mechanical integrity of proton exchange membrane fuel cells: A critical review and discussion." In: *Journal of Power Sources* 364 (2017), pp. 367–373. ISSN: 03787753. DOI: 10.1016/j.jpowsour.2017.08.037.

[40] M. O. Hales et al. "H2GEAR Hydrogen Electric Powertrain – System Architecture." In: *AIAA AVIATION 2023 Forum*. Reston, Virginia: American Institute of Aeronautics and Astronautics, 2023. ISBN: 978-1-62410-704-7. DOI: 10.2514/6.2023-3874.

[41] M. M. Hasan, C. S. Lin, and N. T. van Dresar. "Self-Pressurization of a Flightweight Liquid Hydrogen Storage Tank Subjected to Low Heat Flux." In: *ASME/AIChE National Heat Transfer Conference* (1991).

[42] S. Hasunuma and T. Hayase. "Effect of hydrogen on the dislocation evolution in an aluminum alloy under cyclic loading by two-dimensional discrete dislocation dynamics." In: *International Journal of Fatigue* 176 (2023). ISSN: 01421123. DOI: 10.1016/j.ijfatigue.2023.107856.

[43] Y. He, D. Qiu, and Z. Yu. "Study of failure behaviors of rigid polyurethane foam treated under thermal and vibration conditions by experiment and numerical simulation." In: *Journal of Applied Polymer Science* 140.4 (2023). ISSN: 0021-8995. DOI: 10.1002/app.53364.

[44] M. Heitsch, D. Baraldi, and P. Moretto. "Numerical investigations on the fast filling of hydrogen tanks." In: *International Journal of Hydrogen Energy* 36.3 (2011), pp. 2606–2612. ISSN: 03603199. DOI: 10.1016/j.ijhydene.2010.04.134.

[45] M. Hinsch. *Industrial Aviation Management: A Primer in European Design, Production and Maintenance Organisations*. Berlin, Heidelberg: Springer Berlin Heidelberg, 2019. ISBN: 978-3-662-54739-7. DOI: 10.1007/978-3-662-54740-3.

[46] T. Hoff et al. "Implementation of Fuel Cells in Aviation from a Maintenance, Repair and Overhaul Perspective." In: *Aerospace* 10.1 (2023), p. 23. DOI: 10.3390/aerospace10010023.

[47] N. Hölzel. "Ein Bewertungsansatz zur Analyse von Zustandsmanagementsystemen in Verkehrsflugzeugen unter Berücksichtigung neuer Instandhaltungskonzepte." PhD Thesis. DLR, 2019. DOI: 10.15480/882.2543.

[48] Y. Hou et al. "Effect of strengthened road vibration on performance degradation of PEM fuel cell stack." In: *International Journal of Hydrogen Energy* 41.9 (2016), pp. 5123–5134. ISSN: 03603199. DOI: 10.1016/j.ijhydene.2016.01.072.

[49] S. J. Imen and M. Shakeri. "Reliability Evaluation of an Open–Cathode PEMFC at Operating State and Longtime Vibration by Mechanical Loads." In: *Fuel Cells* 16.1 (2016), pp. 126–134. ISSN: 1615-6846. DOI: 10.1002/fuce.201500144.

[50] International Maintenance Review Board Policy Board. *Issue Paper 185: Handling of Pressure Cylinders within MSG-3*. Apr. 27, 2018. URL: https://www.easa.europa.eu/download/imrbpb/IP%20185%20-%20Hydrostatic%20Test.pdf (visited on 04/23/2022).

[51] International Organization for Standardization. *ISO 11119-3: Gas Cylinders of Composite Construction - Specification and Test Methods: Part 3: Fully Wrapped Fibre Reinforced Composite Gas Cylinders with Non-Load-Sharing Metallic or Non-Metallic Liners*. 2002.

[52] International Organization for Standardization. *ISO 13985: Liquid Hydrogen - Land Vehicle Fuel Tanks*. 2006.

[53] International Organization for Standardization. *ISO 21011: Cryogenic Vessels - Valves for Cryogenic Service*. Berlin, 2008.

[54] International Organization for Standardization. *ISO 21013-1: Cryogenic Vessels - Pressure Relief Accessories for Cryogenic Service: Part 1: Reclosable Pressure-Relief Valves*. 2021.

[55] International Organization for Standardization. *ISO 21029-1: Cryogenic Vessels - Transportable Vacuum Insulated Vessels of not more than 1000 l Volume: Part 1: Design, Fabrication, Inspection and Tests*. 2004.

[56] Iowa State University. *Iowa Environmental Mesonet*. URL: https://mesonet.agron.iastate.edu/request/download.phtml.

[57] P. Irving and C. Soutis, eds. *Polymer Composites in the Aerospace Industry*. Elsevier, 2015. ISBN: 9780857095237. URL: https://books.google.de/books?hl=it&lr=&id=tHHADwAAQBAJ&oi=fnd&pg=PP1&dq=Polymer+Composites+in+the+Aerospace+Industry&ots=SQfSZLnFK4&sig=2gEv5ct1YINqmSCp96g4daXTvuE&redir_esc=y#v=onepage&q&f=false.

[58] S. Jari. "Technical standards for containers for compressed-hydrogen vehicle fuel device." In: *Japan Automobile Research Institute: Tsukuba, Japan* (2004).

[59] S. G. Kandlikar and Z. Lu. "Thermal management issues in a PEMFC stack – A brief review of current status." In: *Applied Thermal Engineering* 29.7 (2009), pp. 1276–1280. ISSN: 13594311. DOI: 10.1016/j.applthermaleng.2008.05.009.

[60] S.-G. Kang et al. "Thermo Elastic Analysis of a Type 3 Cryogenic Tank Considering Curing Temperature and Autofrettage Pressure." In: *Journal of Reinforced Plastics and Composites* 27.5 (2008), pp. 459–472. ISSN: 0731-6844. DOI: 10.1177/0731684407081371.

[61] Z. Kang et al. "Experimental study on cool down characteristics and thermal stress of cryogenic tank during LN2 filling process." In: *Applied Thermal Engineering* 130 (2018), pp. 951–961. ISSN: 13594311. DOI: 10.1016/j.applthermaleng.2017.11.079.

[62] B. Khandelwal et al. "Hydrogen powered aircraft : The future of air transport." In: *Progress in Aerospace Sciences* 60 (2013), pp. 45–59. ISSN: 03760421. DOI: 10.1016/j.paerosci.2012.12.002.

[63] R. M. Khorasany et al. "Simulation of ionomer membrane fatigue under mechanical and hygrothermal loading conditions." In: *Journal of Power Sources* 279 (2015), pp. 55–63. ISSN: 03787753. DOI: 10.1016/j.jpowsour.2014.12.133.

[64] K.-H. Kim et al. "Analysis of heat transfer and frost layer formation on a cryogenic tank wall exposed to the humid atmospheric air." In: *Applied Thermal Engineering* 29.10 (2009), pp. 2072–2079. ISSN: 13594311. DOI: 10.1016/j.applthermaleng.2008.10.015.

[65] M.-G. Kim et al. "Thermally induced stress analysis of composite/aluminum ring specimens at cryogenic temperature." In: *Composites Science and Technology* 68.3-4 (2008), pp. 1080–1087. ISSN: 02663538. DOI: 10.1016/j.compscitech.2007.03.015.

[66] S. Kim and M. M. Mench. "Physical degradation of membrane electrode assemblies undergoing freeze/thaw cycling: Micro-structure effects." In: *Journal of Power Sources* 174.1 (2007), pp. 206–220. ISSN: 03787753. DOI: 10.1016/j.jpowsour.2007.08.111.

[67] S. C. Kim, S. H. Lee, and K. B. Yoon. "Thermal characteristics during hydrogen fueling process of type IV cylinder." In: *International Journal of Hydrogen Energy* 35.13 (2010), pp. 6830–6835. ISSN: 03603199. DOI: 10.1016/j.ijhydene.2010.03.130.

[68] S. D. Knights et al. "Aging mechanisms and lifetime of PEFC and DMFC." In: *Journal of Power Sources* 127.1-2 (2004), pp. 127–134. ISSN: 03787753. DOI: 10.1016/j.jpowsour.2003.09.033.

[69] A. Kusoglu et al. "Mechanical behavior of fuel cell membranes under humidity cycles and effect of swelling anisotropy on the fatigue stresses." In: *Journal of Power Sources* 170.2 (2007), pp. 345–358. ISSN: 03787753. DOI: 10.1016/j.jpowsour.2007.03.063.

[70] J. A. Lee. *Hydrogen Embrittlement*. Huntsville, Alabama, 2016.

[71] Y. Lei et al. "Internal polymeric coating materials for preventing pipeline hydrogen embrittlement and a theoretical model of hydrogen diffusion through coated steel." In: *International Journal of Hydrogen Energy* 47.73 (2022), pp. 31409–31419. ISSN: 03603199. DOI: 10.1016/j.ijhydene.2022.07.034.

[72] Q. Li et al. "Effects of geometry and inconstant mass flow rate on temperatures within a pressurized hydrogen cylinder during refueling." In: *International Journal of Hydrogen Energy* 37.7 (2012), pp. 6043–6052. ISSN: 03603199. DOI: 10.1016/j.ijhydene.2011.12.020.

[73] R. Li et al. "Research on hydrogen environment fatigue test system and correlative fatigue test of hydrogen storage vessel." In: *Journal of Shanghai Jiaotong University (Science)* 19.1 (2014), pp. 88–94. ISSN: 1007-1172. DOI: 10.1007/s12204-013-1463-5.

[74] W. Li et al. "Experiment, simulation, optimization design, and damage detection of composite shell of hydrogen storage vessel-A review." In: *Journal of Reinforced Plastics and Composites* 42.11-12 (2023), pp. 507–536. ISSN: 0731-6844. DOI: 10.1177/07316844221132744.

[75] C. S. Lin, N. T. van Dresar, and M. M. Hasan. "Pressure Control Analysis of Cryogenic Storage Systems." In: *Journal of Propulsion and Power* 20.3 (2004), pp. 480–485. ISSN: 0748-4658. DOI: 10.2514/1.10387.

[76] S. Lin et al. "Thermo-mechanical properties of filament wound CFRP vessel under hydraulic and atmospheric fatigue cycling." In: *Composites Part B: Engineering* 46 (2013), pp. 227–233. ISSN: 13598368. DOI: 10.1016/j.compositesb.2012.09.067.

[77] Y.-L. Liu et al. "Experimental studies on temperature rise within a hydrogen cylinder during refueling." In: *International Journal of Hydrogen Energy* 35.7 (2010), pp. 2627–2632. ISSN: 03603199. DOI: 10.1016/j.ijhydene.2009.04.042.

[78] T. Lochner et al. "Temperature Effects in Polymer Electrolyte Membrane Fuel Cells." In: *ChemElectroChem* 7.17 (2020), pp. 3545–3568. ISSN: 2196-0216. DOI: 10.1002/celc.202000588.

[79] R. M.H. Khorasany et al. "Mechanical degradation of fuel cell membranes under fatigue fracture tests." In: *Journal of Power Sources* 274 (2015), pp. 1208–1216. ISSN: 03787753. DOI: 10.1016/j.jpowsour.2014.10.135.

[80] K. Majewska et al. "Coexisting sub-zero temperature and relative humidity influences on sensors and composite material." In: *Composite Structures* 260 (2021), p. 113263. ISSN: 02638223. DOI: 10.1016/j.compstruct.2020.113263.

[81] A. Manimaran, S. S. Hiremath, and K. P. Shekhar. "Dynamic Simulation and Validation of a Vent and Safety Valve for Cryogenic Flight Tanks." In: *Procedia Technology* 25 (2016), pp. 1320–1334. ISSN: 22120173. DOI: 10.1016/j.protcy.2016.08.232.

[82] R. Manzini and A. Regattieri, eds. *Manutenzione dei sistemi produttivi: Modelli e metodi per la gestione della produttivitá. della qualitá e della sicurezza.* Bologna: Progetto Leonardo Esculapio, 2007. ISBN: 9788874882298. DOI: 61027.

[83] B.-Z. Maytal. "3He Joule-Thomson inversion curve." In: *Cryogenics* 36.4 (1996), pp. 271–274. ISSN: 00112275. DOI: 10.1016/0011-2275(96)88786-8.

[84] R. C. McDonald, C. K. Mittelsteadt, and E. L. Thompson. "Effects of Deep Temperature Cycling on Nafion® 112 Membranes and Membrane Electrode Assemblies." In: *Fuel Cells* 4.3 (2004), pp. 208–213. ISSN: 1615-6846. DOI: 10.1002/fuce.200400015.

[85] R. Meissner et al. "Towards climate-neutral aviation: Assessment of maintenance requirements for airborne hydrogen storage and distribution systems." In: *International Journal of Hydrogen Energy* 48.75 (2023), pp. 29367–29390. ISSN: 03603199. DOI: 10.1016/j.ijhydene.2023.04.058.

[86] D. Melideo et al. "CFD model performance benchmark of fast filling simulations of hydrogen tanks with pre-cooling." In: *International Journal of Hydrogen Energy* 39.9 (2014), pp. 4389–4395. ISSN: 03603199. DOI: 10.1016/j.ijhydene.2013.12.196.

[87] N. de Miguel et al. "Compressed hydrogen tanks for on-board application: Thermal behaviour during cycling." In: *International Journal of Hydrogen Energy* 40.19 (2015), pp. 6449–6458. ISSN: 03603199. DOI: 10.1016/j.ijhydene.2015.03.035.

[88] S. K. Mital et al. *Review of Current State of the Art and Key Design Issues With Potential Solutions for Liquid Hydrogen Cryogenic Storage Tank Structures for Aircraft Applications*. Oct. 1, 2006. URL: https://ntrs.nasa.gov/api/citations/20060056194/downloads/20060056194.pdf (visited on 08/19/2022).

[89] D. Mori and K. Hirose. "Recent challenges of hydrogen storage technologies for fuel cell vehicles." In: *International Journal of Hydrogen Energy* 34.10 (2009), pp. 4569–4574. ISSN: 03603199. DOI: 10.1016/j.ijhydene.2008.07.115.

[90] S. Mouvand and Q. Noharet. "Preliminary design and simulation of a hydrogen-powered regional aircraft." In: *AIAA AVIATION 2023 Forum*. Reston, Virginia: American Institute of Aeronautics and Astronautics, 2023. ISBN: 978-1-62410-704-7. DOI: 10.2514/6.2023-4546.

[91] R. Mukundan et al. "Freeze/Thaw Effects in PEM Fuel Cells." In: *ECS Transactions* 1.8 (2006), pp. 403–413. ISSN: 1938-5862. DOI: 10.1149/1.2214572.

[92] H. NOJOUMI, I. DINCER, and G. NATERER. "Greenhouse gas emissions assessment of hydrogen and kerosene-fueled aircraft propulsion." In: *International Journal of Hydrogen Energy* 34.3 (2009), pp. 1363–1369. ISSN: 03603199. DOI: 10.1016/j.ijhydene.2008.11.017.

[93] R. Ortiz Cebolla et al. "Hydrogen tank first filling experiments at the JRC-IET GasTeF facility." In: *International Journal of Hydrogen Energy* 39.11 (2014), pp. 6261–6267. ISSN: 03603199. DOI: 10.1016/j.ijhydene.2013.10.038.

[94] D. N. Ozen, B. Timurkutluk, and K. Altinisik. "Effects of operation temperature and reactant gas humidity levels on performance of PEM fuel cells." In: *Renewable and Sustainable Energy Reviews* 59 (2016), pp. 1298–1306. ISSN: 13640321. DOI: 10.1016/j.rser.2016.01.040.

[95] P. J. Pelto et al. *Analysis of LNG Peakshaving Facility Release Prevention Systems*. United States, 1982. DOI: 10.2172/6747398.

[96] K. O. Pomeroy et al. "Cryostorage tank failures: temperature and volume loss over time after induced failure by removal of insulative vacuum." In: *Journal of assisted reproduction and genetics* 36.11 (2019), pp. 2271–2278. DOI: 10.1007/s10815-019-01597-5.

[97] R. F. Ponden. "Reliability of a Cryogenic Liquid Storage Vessel." Master Thesis. Bethlehem, PA, USA: Lehigh University, 1982. URL: https://asa.lib.lehigh.edu/Record/10633714 (visited on 08/10/2022).

[98] D. Qiu et al. "Mechanical degradation of proton exchange membrane along the MEA frame in proton exchange membrane fuel cells." In: *Energy* 165 (2018), pp. 210–222. ISSN: 03605442. DOI: 10.1016/j.energy.2018.09.136.

[99] D. Qiu et al. "Mechanical failure and mitigation strategies for the membrane in a proton exchange membrane fuel cell." In: *Renewable and Sustainable Energy Reviews* 113 (2019), p. 109289. ISSN: 13640321. DOI: 10.1016/j.rser.2019.109289.

[100] Y. Qiu et al. "Research Progress of Cryogenic Materials for Storage and Transportation of Liquid Hydrogen." In: *Metals* 11.7 (2021), p. 1101. DOI: 10.3390/met11071101.

[101] Radio Technical Commission for Aeronautics. *Environmental Conditions and Test Procedures for Airborne Equipment: (DO-160G)*. 2010. URL: https://do160.org/rtca-do-160g/.

[102] B. C. Ray. "Temperature effect during humid ageing on interfaces of glass and carbon fibers reinforced epoxy composites." In: *Journal of Colloid and Interface Science* 298.1 (2006), pp. 111–117. ISSN: 00219797. DOI: 10.1016/j.jcis.2005.12.023.

[103] Reinhard Faaß. *Cryoplane - final technical report*. 2001.

[104] O. A. Rosyid, D. Jablonski, and U. Hauptmanns. "Risk analysis for the infrastructure of a hydrogen economy." In: *International Journal of Hydrogen Energy* 32.15 (2007), pp. 3194–3200. ISSN: 03603199. DOI: 10.1016/j.ijhydene.2007.02.012.

[105] Y. Rotenberg, M. Burrows, and R. McNeil. "VIBRATION EFFECTS ON BOIL-OFF RATE FROM A SMALL LIQUID HYDROGEN TANK." In: *International Association for Hydrogen Energy*. Vol. 11, No. 11 (1986), pp. 729–735.

[106] C. K. Sain, J. Hänsel, and S. Kazula. "Conceptual Design of Air and Thermal Management in a Nacelle-Integrated Fuel Cell System for an Electric Regional Aircraft." In: *AIAA AVIATION 2023 Forum*. Reston, Virginia: American Institute of Aeronautics and Astronautics, 2023. ISBN: 978-1-62410-704-7. DOI: 10.2514/6.2023-3875.

[107] S. Satyapal et al. "The U.S. Department of Energy's National Hydrogen Storage Project: Progress towards meeting hydrogen-powered vehicle requirements." In: *Catalysis Today* 120.3-4 (2007), pp. 246–256. ISSN: 09205861. DOI: 10.1016/j.cattod.2006.09.022.

[108] M. Schmelcher and J. HäSSy. *Hydrogen fuel cells for aviation*.

[109] M. Schmidt. "A review of aircraft turnaround operations and simulations." In: *Progress in Aerospace Sciences* 92 (2017), pp. 25–38. ISSN: 03760421. DOI: 10.1016/j.paerosci.2017.05.002.

[110] D. Schultheiß. "Permeation Barrier for lightweight Liquid Hydrogen Tanks." Ph.D. Thesis. Augsburg: Mathematisch-Naturwissenschaftlichen Fakultät, 2007.

[111] M. J. Sefain. *Hydrogen aircraft concepts & ground support.* 2000.

[112] K. Song et al. "Assembly techniques for proton exchange membrane fuel cell stack: A literature review." In: *Renewable and Sustainable Energy Reviews* 153 (2022), p. 111777. ISSN: 13640321. DOI: 10.1016/j.rser.2021.111777.

[113] K. Sotoodeh. "The Design of Pressure Safety and Relief Valves for Overpressure Protection: Essential considerations." In: *Transactions of the Indian National Academy of Engineering* 8.2 (2023), pp. 273–287. ISSN: 2662-5415. DOI: 10.1007/s41403-023-00396-w.

[114] K. Sotoodeh and O. T. Gudmestad. "Valve design considerations in liquid hydrogen systems to prevent failure." In: *International Journal on Interactive Design and Manufacturing (IJIDeM)* 17.3 (2023), pp. 1429–1441. ISSN: 1955-2513. DOI: 10.1007/s12008-022-01158-8.

[115] S. Speaks. *Reliability and MTBF Overview.* 2010.

[116] M. Still, H. Venzke, and A. Melling. "Influence of humidity on the convective heat transfer from small cylinders." In: *Experiments in Fluids* 24 (1998), pp. 141–150.

[117] Y. Su et al. "Review of the Hydrogen Permeability of the Liner Material of Type IV On-Board Hydrogen Storage Tank." In: *World Electric Vehicle Journal* 12.3 (2021), p. 130. DOI: 10.3390/wevj12030130.

[118] I. G. Tapeinos et al. "Evaluation of the mechanical performance of a composite multi-cell tank for cryogenic storage: Part I - Tank pressure window based on progressive failure analysis." In: *International Journal of Hydrogen Energy* 44.7 (2019), pp. 3917–3930. ISSN: 03603199. DOI: 10.1016/j.ijhydene.2018.12.118.

[119] I. G. Tapeinos et al. "Evaluation of the mechanical performance of a composite multi-cell tank for cryogenic storage: Part II – Experimental assessment." In: *International Journal of Hydrogen Energy* 44.7 (2019), pp. 3931–3943. ISSN: 03603199. DOI: 10.1016/j.ijhydene.2018.12.063.

[120] Y. Teng, L. Xie, and H. Zhang. "Experimental Study on Vibration Fatigue Behavior of Aircraft Aluminum Alloy 7050." In: *Materials (Basel, Switzerland)* 15.21 (2022). ISSN: 1996-1944. DOI: 10.3390/ma15217555.

[121] T. Terada et al. "Thermal behaviour in hydrogen storage tanks for FCV on Fast Filling." In: *SAE Technical Paper 2008-01-0463* (2007). DOI: 10.4271/2008-01-0463.

[122] R. L. Tobler and R. P. Reed. "Fracture Mechanics Parameters for a 5083-0 Aluminum Alloy at Low Temperatures." In: *Institute for Basic Standards, Cryogenics Division,* (1977). DOI: 10.1115/1.3443545.

[123] J.-i. Tomioka et al. "Ambient temperature pressure cycle test of compressed hydrogen tanks for vehicles e influence of maximum pressure on tank fatigue." In: *SAE 2007 World Congress* (2007). DOI: 10.4271/2007-01-0691.

[124] J.-i. Tomioka et al. "Influence of temperature on the fatigue strength of compressed-hydrogen tanks for vehicles." In: *International Journal of Hydrogen Energy* 36.3 (2011), pp. 2513–2519. ISSN: 03603199. DOI: 10.1016/j.ijhydene.2010.04.120.

[125] U.S. Department of Energy. *Targets for Onboard Hydrogen Storage Systems for Light-Duty Vehicles*. 2009.

[126] T. T. Veenstra et al. "Development of a stainless steel check valve for cryogenic applications." In: *Cryogenics* 47.2 (2007), pp. 121–126. ISSN: 00112275. DOI: 10.1016/j.cryogenics.2006.10.004.

[127] A. Velicki and Da Hansen. *Hydrogen fueled blended wing body ring tank*. 2006.

[128] D. Verstraete. "Long Range Transport Aircraft Using Hydrogen Fuel." In: *International Journal of Hydrogen Energy* 38.34 (2013), pp. 14824–14831. ISSN: 03603199. DOI: 10.1016/j.ijhydene.2013.09.021.

[129] D. Verstraete. "Long range transport aircraft using hydrogen fuel." In: *International Journal of Hydrogen Energy* 38.34 (2013), pp. 14824–14831. ISSN: 03603199. DOI: 10.1016/j.ijhydene.2013.09.021.

[130] D. Verstraete. "The Potential ofLiquid Hydrogen for long range aircraft propulsion." Ph. D. Thesis. Cranfield University, 2009.

[131] G. Voudouris, D. Di Maio, and I. A. Sever. "Experimental fatigue behaviour of CFRP composites under vibration and thermal loading." In: *International Journal of Fatigue* 140 (2020), p. 105791. ISSN: 01421123. DOI: 10.1016/j.ijfatigue.2020.105791.

[132] Z. Wan et al. "A Review on Cold Start of Proton Exchange Membrane Fuel Cells." In: *Energies* 7.5 (2014), pp. 3179–3203. DOI: 10.3390/en7053179.

[133] B. Wang et al. "LH 2 tank pressure control by thermodynamic vent system (TVS) at zero gravity." In: *IOP Conference Series: Materials Science and Engineering)* 171 (2017). DOI: 10.1088/1757-899X/171/1/012046.

[134] B. Wang et al. "Experimental study on pressure control of liquid nitrogen tank by thermodynamic vent system." In: *Applied Thermal Engineering* 125 (2017), pp. 1037–1046. ISSN: 13594311. DOI: 10.1016/j.applthermaleng.2017.07.067.

[135] D. Wang et al. "Experimental Analysis on Residual Performance of Used 70 MPa Type IV Composite Pressure Vessels." In: *Journal of Failure Analysis and Prevention* 19.1 (2019), pp. 204–211. ISSN: 1547-7029. DOI: 10.1007/s11668-019-00581-6.

[136] G. Wei and J. Zhang. "Numerical Study of the Filling Process of a Liquid Hydrogen Storage Tank under Different Sloshing Conditions." In: *Processes* 8.9 (2020), p. 1020. DOI: 10.3390/pr8091020.

[137] R. J. Werlink, J. Fesmire, and J. P. Sass. "Vibration considerations for cryogenic tanks using glass bubbles insulation." In: *AIP Conference Proceedings*. AIP Conference Proceedings. AIP, 2012, pp. 55–65. DOI: 10.1063/1.4706905.

[138] C. Winnefeld et al. "Modelling and Designing Cryogenic Hydrogen Tanks for Future Aircraft Applications." In: *Energies* 11.1 (2018), p. 105. DOI: 10.3390/en11010105.

[139] N. J. Wood, M. O. Hales, and S. Taylor. *AIAA AVIATION 2023 Forum*. Reston, Virginia, 2023. DOI: 10.2514/MAVIAT23.

[140] E. Wu et al. "Fatigue life prediction and verification of high-pressure hydrogen storage vessel." In: *International Journal of Hydrogen Energy* 46.59 (2021), pp. 30412–30422. ISSN: 03603199. DOI: 10.1016/j.ijhydene.2021.06.177.

[141] W. Xu, Q. Li, and M. Huang. "Design and Analysis of Liquid Hydrogen Storage Tank for High-Altitude Long-Endurance Remotely-Operated Aircraft." In: *International Journal of Hydrogen Energy* 40.46 (2015), pp. 16578–16586. ISSN: 03603199. DOI: 10.1016/j.ijhydene.2015.09.028.

[142] Q. Xujin, M. Chuiju, and H. Yonghua. "Modeling of pressure control in a cryogenic tank by a thermodynamic vent system considering flash evaporation." In: *International Journal of Heat and Mass Transfer* 204.123857 (2023). ISSN: 00179310. DOI: 10.1016/j.ijheatmasstransfer.2023.123857.

[143] Q. Yan, H. Toghiani, and J. Wu. "Investigation of water transport through membrane in a PEM fuel cell by water balance experiments." In: *Journal of Power Sources* 158.1 (2006), pp. 316–325. ISSN: 03787753. DOI: 10.1016/j.jpowsour.2005.09.013.

[144] Q. Yan et al. "Effect of sub-freezing temperatures on a PEM fuel cell performance, startup and fuel cell components." In: *Journal of Power Sources* 160.2 (2006), pp. 1242–1250. ISSN: 03787753. DOI: 10.1016/j.jpowsour.2006.02.075.

[145] J. YANG and M. HUBER. "Analysis of thermodynamic processes involving hydrogen." In: *International Journal of Hydrogen Energy* 33.16 (2008), pp. 4413–4418. ISSN: 03603199. DOI: 10.1016/j.ijhydene.2008.05.085.

[146] T. Yoshi, K. Okubo, and T. Fujii. "Stiffness Reduction of Woven CFRP and CFRTP Spring under Ultra High Cyclic Fatigue for Vibration Conveyor." In: *Advanced Materials Research* 123-125 (2010), pp. 217–220. DOI: 10.4028/www.scientific.net/AMR.123-125.217.

[147] M. Zhang et al. "A literature review of failure prediction and analysis methods for composite high-pressure hydrogen storage tanks." In: *International Journal of Hydrogen Energy* 44.47 (2019), pp. 25777–25799. ISSN: 03603199. DOI: 10.1016/j.ijhydene.2019.08.001.

[148] X. B. Zhang et al. "Experimental study on cryogenic moisture uptake in polyurethane foam insulation material." In: *Cryogenics* 52.12 (2012), pp. 810–815. ISSN: 00112275. DOI: 10.1016/j.cryogenics.2012.10.001.

[149] J. Zhao and X. Li. "A review of polymer electrolyte membrane fuel cell durability for vehicular applications: Degradation modes and experimental techniques." In: *Energy Conversion and Management* 199 (2019), p. 112022. ISSN: 01968904. DOI: 10.1016/j.enconman.2019.112022.

[150] L. Zhao et al. "Numerical simulation of temperature rise within hydrogen vehicle cylinder during refueling." In: *International Journal of Hydrogen Energy* 35.15 (2010), pp. 8092–8100. ISSN: 03603199. DOI: 10.1016/j.ijhydene.2010.01.027.

[151] C.-x. Zheng et al. "Fatigue test of carbon epoxy composite high pressure hydrogen storage vessel under hydrogen environment." In: *Journal of Zhejiang University SCIENCE A* 14.6 (2013), pp. 393–400. ISSN: 1673-565X. DOI: 10.1631/jzus.A1200297.

[152] J. Zheng et al. "Experimental and numerical study on temperature rise within a 70 MPa type III cylinder during fast refueling." In: *International Journal of Hydrogen Energy* 38.25 (2013), pp. 10956–10962. ISSN: 03603199. DOI: 10.1016/j.ijhydene.2013.02.053.

[153] W. Zhou et al. "Review on optimization design, failure analysis and non-destructive testing of composite hydrogen storage vessel." In: *International Journal of Hydrogen Energy* 47.91 (2022), pp. 38862–38883. ISSN: 03603199. DOI: 10.1016/j.ijhydene.2022.09.028.

[154] K. Zhu et al. "Influence of filling methods on the cool down performance and induced thermal stress distribution in cryogenic tank." In: *Applied Thermal Engineering* 141 (2018), pp. 1009–1019. ISSN: 13594311. DOI: 10.1016/j.applthermaleng.2018.06.030.